STUDIA UNIVERSITATIS
BABEŞ-BOLYAI

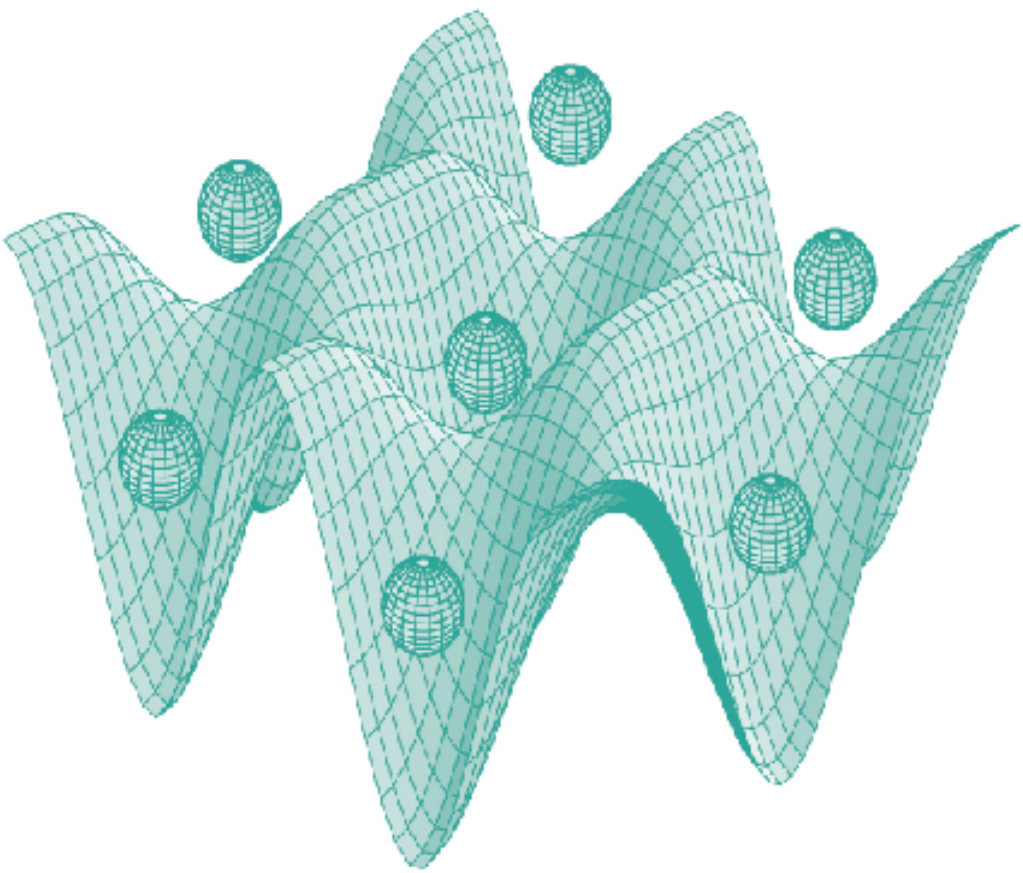

PHYSICA

1-2/2018

STUDIA
UNIVERSITATIS BABEŞ-BOLYAI
PHYSICA

Dedicated to Professor Dr. Aurel Pop
on his 65th Anniversary

1-2/2018
January-December

EDITORIAL OFFICE OF STUDIA UBB PYSICA:
1, M. Kogălniceanu St., Cluj-Napoca, ROMANIA, Phone: +40 264 405300
http://www.studia.ubbcluj.ro/serii/physica/index_en.html

YEAR **Volume 63 (LXIII) 2018**
MONTH **DECEMBER**
ISSUE **1-2**

PUBLISHED ONLINE: 2018-12-30
PUBLISHED PRINT: 2018-12-30
ISSUE DOI:10.24193/subbphys.2018

S T U D I A
UNIVERSITATIS BABEŞ–BOLYAI

PHYSICA

1-2

Dedicated to Professor Dr. Aurel Pop on his 65th anniversary

STUDIA UBB EDITORIAL OFFICE: B.P. Hasdeu no. 51, 400371 Cluj-Napoca, Romania,
Phone + 40 264 405352

CUPRINS – CONTENT – SOMMAIRE – INHALT

STUDIA UBB PHYSICA, Vol. 63 (LXIII), 1-2, 2018, pp. 5-7
(RECOMMENDED CITATION)

FOREWORD

ANNIVERSARY OF PROFESSOR AUREL POP

It is a great pleasure to honor Aurel Pop with this dedicated issue on "Studia Universitatis Babes-Bolyai – seria Physica". Aurel Pop has contributed to the synthesis and characterization of various materials, like polycrystals, thin films, interfaces, and nanostructures covering a broad range of materials and methods and is well recognized in the worldwide scientific community.

Aurel Pop was born in Feleacu, Cluj county, Romania, on July 8, 1953 and graduated Faculty of Physics at the Babes-Bolyai University in 1976. In the period 1976-1977 he has followed Master studies in Solid State Physics at the same University. He performed his PhD studies between 1989 and 1993 at Babes-Bolyai University under the supervision of prof. dr. Alexandru Nicula and prof. dr. Ioan Cosma. In this time his studies became more comprehensive, and they covered a broader research field. His Ph.D. thesis was entitled "*Electric and Magnetic Properties Studies on High T_C superconductor oxidic compounds*". The effect of the Gd substitution on Y site on structural, magnetic and electric properties in YBCO compounds were reported. He has shown the presence of thermal fluctuations below 170 K, confirmed by a metallic behavior at low temperatures and by Hall effect measurements. Several methods were used as static and dynamic susceptibility, transport and EPR measurements.

He starts to work in 1977 as a teacher of physics at the Chemistry Industrial High School Craiova till 1987. During this period, he acts also as vice-director at the same institution. From 1987 till 2018 he has occupied several positions at Babes-Bolyai University, Faculty of Physics. He was assistant professor (1988-1993), lecturer (1994-1996), associate professor (1997-2000) and full professor starting with 2001. In this period he was

teaching different courses, seminars and laboratory classes, at bachelor level, like: “Mechanics and Acoustic”, “Molecular Physics and Thermodynamic”, master level courses for master degree as follows: “Thin films physics”, “Transport phenomena”, “Physics of vortex systems”, ”Magnetic and superconducting materials” and PhD level: “Experimental methods in solid state physics”. He was focused on understanding the modern directions in science and technologies, and to introduce these new information, at high scientific level, from the field of solid state and applied physics, in him courses. The teaching activities performed by during this years were very appreciated by him students. He was awarded by the University with “The Diploma of Merit” in 2005, Diploma Comenius in 2010, and Diploma Teacher of the Year in 2011.

Aurel Pop research interest was focused in the field of high temperature superconductivity: synthesis, structural, electric and magnetic characterization of different classes of superconducting materials with high transition temperatures, both bulk and thin films. In the last years, another field of interest was the study of electrodeposited nanocomposite coating and their anticorrosive behaviour and ZnO doped thin films, respectively. In his research activities Aurel has installed and used different techniques for thin films preparation and characterization as follows: installation the equipment for thin film synthesis by magnetron sputtering, a.c. magnetic susceptibility devices, magnetization devices, and transport properties measurements. In the last years he was involved in numerous studies related to the understanding of the morphological and structural particularities of a large variety of nanostructures with potential applications, as well as of the processes in which such systems are involved. He was involved in the field of magnetism and superconductivity during 1 year and 3 month (1999-2000) at Universite Libre de Bruxelles, Department “Physiques des Solides et Cryophysique” (Director prof. R. Deltour). He has published 97 papers in prestigious ISI journals like Thin Solid Films, J. Alloys and Compounds, Superconductor Science and Technology, J. of Applied Electrochemistry and others. In the same time, he has contributed with 8 papers in journals of the Romanian Academy, 38 papers in University journals, 20 papers in International non-ISI journals and 8 in Proceedings of International

Conferences, 63 abstracts in international conferences volumes and 7 books. He was awarded in 2005 with the Romanian Academy "Stefan Procopiu" prize for his researches on *Oxidic superconducting materials with high transition temperature* and with Babes-Bolyai University prize for the book "*Introduction on the Physics of Vortex Systems*" in 2004. He was director of many research grants. His result has attracted many appreciations in scientific literature, confirmed by the high number of citations in ISI journals.

Besides his scientific activity, Aurel Pop was permanently involved in the academic development at local and national levels. In this respect, he served as Head of Mechanics and Solid State Physics Department of the Faculty of Physics (1996–1998), as Head of the Department of Condensed Matter Physics and Advanced Technologies (1998–2012), as Dean of the Faculty of Physics (2012–2018), as President of the Cluj Branch of the Romanian Physics Society (2013–2017), as member of the National Council for Research in Romanian University (2000–2008), and ARACIS member staring with 2011, member of the Senate and member of the Faculty Council.

He is also a member of the following international scientific societies: European Physical Society, Romanian Physical Society, Balkan Physical Society and IEEE Magnetic Society. He serve as Editor in Chief of *Studia Universitatis Babes-Bolyai, seria PHYSICA* (2012-2018) and member in the editorial office of the journal *Coroziune si protectie anticoroziva* from Technical University of Cluj-Napoca.

Under his supervision, many students obtained their license Diploma degree, Diploma at the Master or PhD in Physics. In the name of all his students and his colleagues I would like to express the deepest appreciation and best wishes for the future.

Dr. Romulus Tetean
Professor at Babes-Bolyai University

STUDIA UBB PHYSICA, Vol. 63 (LXIII), 1-2, 2018, pp. 9-18
(RECOMMENDED CITATION)
doi:10.24193/subbphys.2018.01

MAGNETOCALORIC EFFECT AND MAGNETIC PROPERTIES OF $Pr_{1-x}Ce_xCo_3$ COMPOUNDS

G. SOUCA[1,*], S. IAMANDI[1], C. MAZILU[1], R. DUDRIC[1], R. TETEAN[1]

ABSTRACT. Magnetic properties and magnetocaloric effect under moderate magnetic field in polycrystalline $Pr_{1-x}Ce_xCo_3$ compounds with x = 0, 0.1, 0.2, 0.3, and 0.4 are reported. The powder X-ray diffraction measurements show that all samples crystallize in the rhombohedral $PuNi_3$-type structure (space group: R-*3m*), specific for $PrCo_3$, with the lattice parameters decreasing with the cerium content. The magnetic measurements indicate a transition from a magnetic order state to a paramagnetic one below room temperature. The Curie temperature decreases roughly linear with the Ce concentration from 270 K for x = 0.1 to 146 K for x = 0.4. A moderate magnetocaloric effect was found for all samples, with the maximum entropy change located at temperatures near the magnetic transition ones.

Keywords: *rare earth based intermetallic compounds, Curie temperature, magnetocaloric effect.*

1. INTRODUCTION

The magnetic properties and magnetocaloric effect investigations of *R* -*T* (*R* = rare earth, *T* = transition metal) intermetallic compounds has been the subject of many theoretical and experimental studies, due to their potential technological applications as magnetic refrigerating materials around room temperature.

[1] *Babes-Bolyai University, Faculty of Physics, 1 Kogalniceanu street,400084 Cluj-Napoca, Romania*
[*] *Corresponding author: gabrielasouca@gmail.com*

Magnetocaloric effect is an intrinsic phenomenon for magnetic materials and can be defined as the absorption or emission of heat when a magnetic material is subjected to a change of a magnetic field [1-2]. Closely related to the MCE value and to magnetic contribution to the heat capacity is magnetic entropy and its change. The magnetic entropy change (ΔS_m) is also a tool used to determine the capacity of the magnetic refrigerators. *R-T* based intermetallic systems have been intensively investigated and reported to have large MCE in a wide temperature range, depending on the constituent elements and composition [3-5].

Among these series of compounds, *R*-Co_3 intermetallic compounds have attracted a lot of scientific interest due to their wide applications as permanent magnets and due to their excellent magnetic properties, such as large magnetocrystalline anisotropy and important saturation magnetization at room temperature [6].

R-Co_3 compounds crystalize in the rhombohedral $PuNi_3$-type structure (space group: R-*3m*). The unit cell contains two crystallographic sites for R atoms (3a and 6c) and three crystallographic sites for Co atoms (3b, 6c and 18h) [7] The important magnetic properties of RCo_3 are the result of the combination of *4f* - localized and *3d* - itinerant magnetism [8] Usually, the transition metal, Co is the one which provides high transition temperature and saturation magnetization, while rare earth element, *R* provides high magnetocrystalline anisotropy.

Previously, $PrCo_3$ was reported to be highly anisotropic uniaxial ferromagnet [9-11] with the easy magnetization direction parallel to the c-axis and the Curie temperature of 349 K [6]. Unlike other RCo_3 compounds, $CeCo_3$ shows different magnetic behavior like very low transition temperature (~50 K) and a low value of magnetic susceptibility. The *3d* weak magnetism in $CeCo_3$ compared with other members of RCo_3 compounds indicate that Ce is probably in an intermediate valence state [12-14]. Previous studies of magnetocaloric effect on *R*-Co_3 compounds with Al substitution on Co site [15] show that hybridization effects cause the adjustment of the transition temperature through the room temperature. Depending on the dopant concentration, a significant value of the magnetic entropy changes around transition temperature can be

obtain. The experimental reports suggest that these types of compounds can be used for magnetic refrigeration.

This paper reports on the elaboration of polycrystalline samples of $Pr_{1-x}Ce_xCo_3$, the structural, magnetic and magnetocaloric properties, not investigated so far, to our best knowledge.

2. EXPERIMENTAL DETAILS

The samples of $Pr_{1-x}Ce_xCo_3$ (x = 0, 0.1, 0.2, 0.3, 0.4) were prepared by arc-melting technique, under highly purified Ar atmosphere from high purity of Pr, Ce and Co (>99.9%) acquired from Alfa Aesar. Several consecutive meltings were performed to ensure homogeneity and a small excess of rare earth element (3% Ce and 1% Pr) was used in order to compensate for losses during melting. The samples were heat treated at 850 ºC in vacuum for 7 days and slowly cooled to room temperature. The crystallographic structure of the samples was checked by X-ray powder diffraction technique, at room temperature using a Bruker D8 Advance AXS diffractometer with Cu Kα radiation. All the magnetic investigations were performed in the temperature range 4 - 300 K and external magnetic field up to 12 T, using a 12 T Vibrating Sample Magnetometer (VSM) from Cryogenics. The magnetic entropy changes were calculated from magnetization isotherms, between zero field and a maximum field (H_0) using the thermodynamic relation:

$$\Delta S_m(T,H_0) = S_m(T,H_0) - S_m(T,0) = \frac{1}{\Delta T}\int_0^{H_0}\left[M(T+\Delta T,H) - M(T,H)\right]dH \qquad (1)$$

with an increment in temperature between measured magnetization isotherms of ΔT = 5K. The refrigerant capacity or the relative cooling power (RCP) was used to evaluate the magnetic refrigeration of materials:

$$RCP(S) = -\Delta S_m(T,H) \times \delta T_{FWHM} \qquad (2)$$

where ΔS_m is the maximum value of the magnetic entropy change and δT_{FWHM} its full-width at half-maximum.

3. RESULTS AND DISCUSSION

The crystal structure of $Pr_{1-x}Ce_xCo_3$ was investigated by powder X-ray diffraction. As shown in **Figure 1**, these compounds crystallize in the rhombohedral $PuNi_3$-type structure (space group: R-*3m*), specific for $PrCo_3$.

The lattice parameters listed in **Table 1** were obtained by Rietveld refinement using Fullprof software [16] on the measured patterns; a representative result is shown in **Figure 2**. The obtained values for lattice parameters are in good agreement with those reported previously for $PrCo_3$ [17]. The Ce doped samples show slightly smaller values for both lattice parameters than those for $PrCo_3$, as expected considering the smaller ionic radius of the cerium compared to the praseodymium ionic radius. **Figure 3** shows the decrease of the lattice parameters on the *a*- axis, almost linearly, as the cerium concentration is increasing. The c lattice parameters remain almost constant.

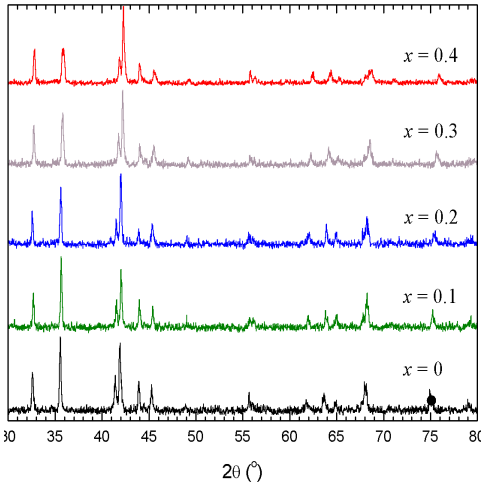

Figure 1. X-ray diffraction patterns for the $Pr_{1-x}Ce_xCo_3$ samples

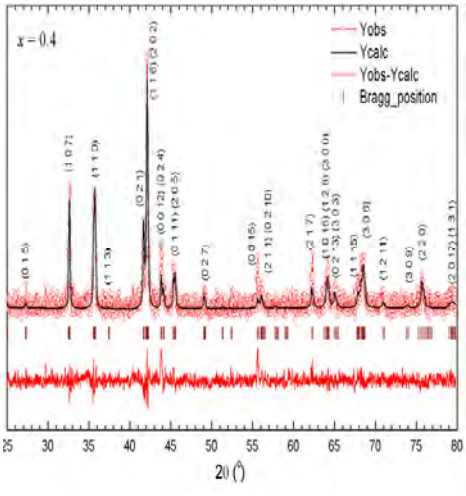

Figure 2. X-ray diffraction pattern together with the calculated profile using Rietveld method and difference curve of the $Pr_{0.6}Ce_{0.4}Co_3$ sample

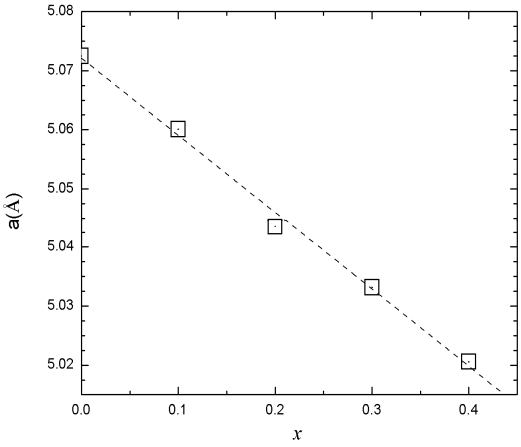

Figure 3. The concentration dependence of *a* lattice parameter for $Pr_{1-x}Ce_xCo_3$ samples

Table 1. Refined lattice parameters of$Pr_{1-x}Ce_xCo_3$ investigated samples

x	a(Å)	c(Å)
0	5.07(2)	24.81(1)
0.1	5.06(1)	24.79(7)
0.2	5.04(4)	24.77(4)
0.3	5.03(3)	24.78(1)
0.4	5.02(1)	24.77(7)

Zero Field Cooled (ZFC) – Field Cooled (FC) magnetization measurements were performed under a moderate applied magnetic field of 0.05T, in the temperature range of 4 – 300 K as plotted in **Figure 4,** for the samples with *x* = 0.1 and *x* =0.2. Both ZFC and FC curves show a typical paramagnetic to ferromagnetic transition. The difference between the ZFC and FC curves below the ordering temperature increases with Ce content. The spin-glass like features [18-19], may be due to the presence of a possible magnetic disorder and the magnetocrystalline anisotropies [20].

The transition temperatures from the paramagnetic state to the magnetic order one defined as the temperature corresponding to the minimum of $\delta M/\delta T$ were calculated and plotted for all samples, as shown

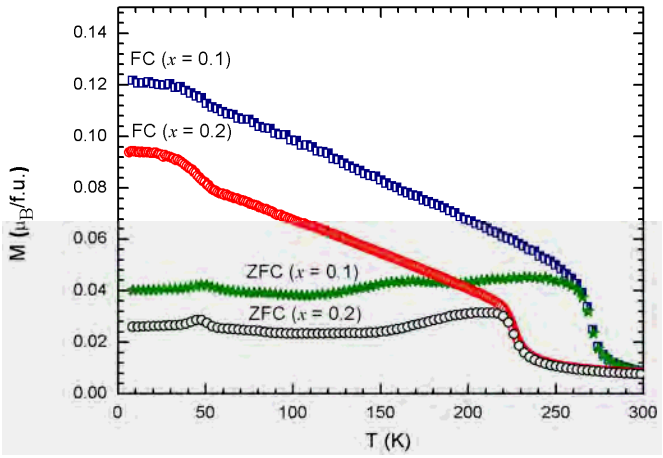

Figure 4. Temperature dependences of magnetization measured in zero field-cooling (ZFC) and field-cooling (FC) modes for all samples

in **Figure 5.** A decrease, almost linearly, of the transition temperature is observed with the increase of the Ce concentration, from 270 K for x = 0.1 to 146 K for x = 0.4. The reduction of the magnetic ordering temperature is caused by the changes associated with hybridization of 5*d* orbitals of Ce and 3*d* orbitals of Co and the intersublattice 3*d*-4*f* exchange interaction (J_{PrCo}) which decreases with the substitution of Pr for Ce [21].

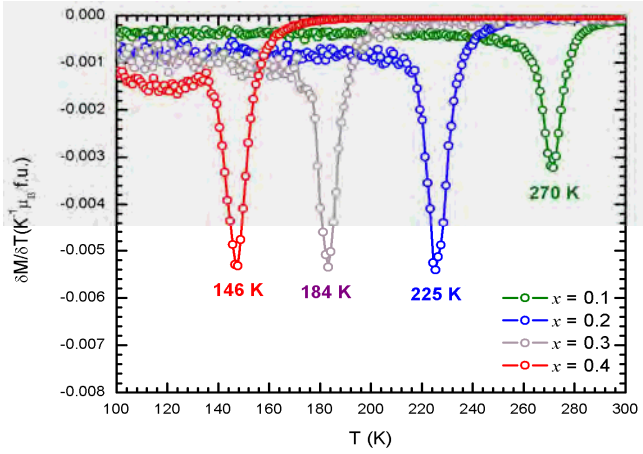

Figure 5. The first derivative of the magnetization versus temperature and the transition temperature for all samples

The magnetization isotherms measured between T = 100 K and T = 300 K are shown in **Figure 6**, for the sample with x = 0.2. The measurements indicate the same trend for all samples, the saturation being not reached until the 12 T value of the applied magnetic field. The difficulty of approaching a magnetic saturation state can be explained by the spin glass like behavior also highlighted by ZFC-FC measurements.

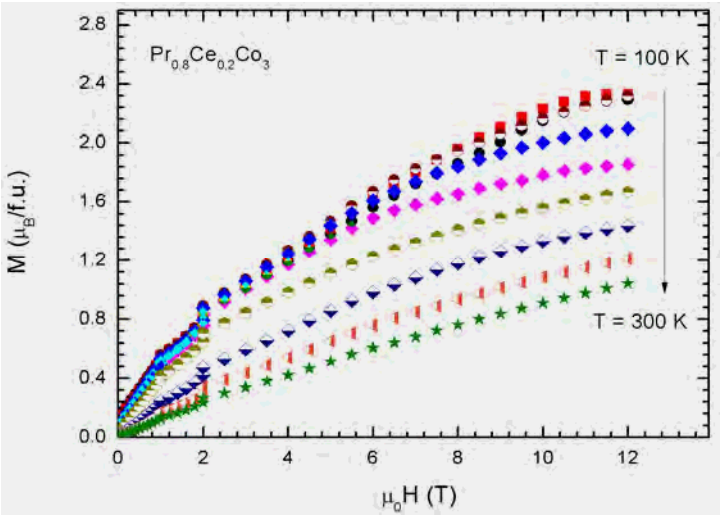

Figure 6. Magnetization isotherms for $Pr_{0.8}Ce_{0.2}Co_3$ in the temperature range 100 K and 300 K

The Arrot plots for $Pr_{0.8}Ce_{0.2}Co_3$, calculated from the magnetization isotherms around the transition temperature are represented in **Figure 7**. The Arrot curves for all samples display a second order magnetic phase transition from a ferromagnetic to a paramagnetic state at T_c, a specific feature for magnetic refrigerants.

The magnetic entropy changes were calculated based on the magnetization isotherms measured between 200 K and 300 K, with a step of 5 K, in the external magnetic field of 2 T and 4 T and plotted as a function of temperature in **Figure 8.** The maximum value of the magnetic entropy change is reached at temperatures close to the magnetic transition ones, for all the investigated samples. The substitution of Ce for Pr causes a decrease in maximum entropy change values, as listed in **Table 2**. This decrease in maximum

values of magnetic entropy change may be caused by the decrease in the concentration of the Pr ions and by the disorder. Nevertheless, the $|\Delta S_m|$ peaks are broader, which is mandatory for a good refrigerant material. Moreover, it can be observed that the curves are nearly symmetric distributed around the transition temperature, a behavior generally characteristic for materials exhibiting a second order magnetic phase transition [22].

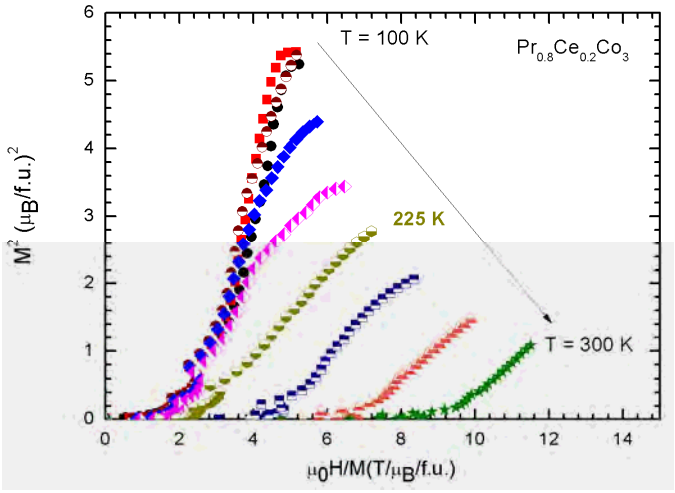

Figure 7. Arrot plots for $Pr_{0.8}Ce_{0.2}Co_3$ sample.

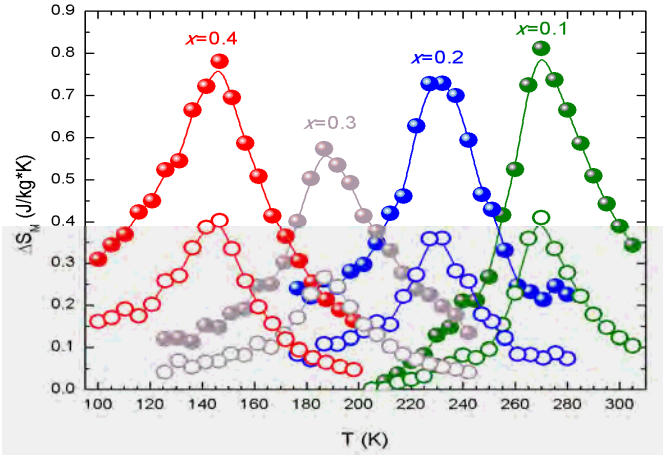

Figure 8. The temperature dependences of the magnetic entropy change for $Pr_{1-x}Ce_xCo_3$ compounds in ΔH=4T and ΔH=2T

The magnetic refrigeration efficiency was evaluated by calculating the relative cooling power (*RCP*) for all the investigated samples. The RCP*(S)* values, presented in **Table 2**, indicate that the materials could be used for the magnetic refrigeration applications.

Table 2. Magnetocaloric properties of $Pr_{1-x}Ce_xCo_3$ compounds

x	T_{max} (K)	$\|\Delta S_M\|$ (J/KgK)		δT_{FWHM} (K)		RCP(*S*) (J/kg)	
		ΔH=4T	ΔH=2T	ΔH=4T	ΔH=2T	ΔH=4T	ΔH=2T
0.1	270	0.81	0.41	44	30	35.6	12.3
0.2	230	0.72	0.36	46	34	33.1	12.2
0.3	188	0.55	0.27	48	35	26.4	9.45
0.4	146	0.78	0.40	60	41	46.8	16.4

CONCLUSIONS

The structural, magnetic and magnetocaloric properties of $Pr_{1-x}Ce_xCo_3$ have been studied. All samples crystallize in the rhombohedral $PuNi_3$-type structure, with the lattice parameters slightly smaller than those for $PrCo_3$. The magnetic measurements indicate a roughly linear decrease of the transition temperature with Ce concentration, from 270 K for x = 0.1 to 146 K for x = 0.4. The decrease in Curie temperature could be attributed to the changes associated with hybridization of 5*d* orbitals of Ce and 3*d* orbitals of Co and the intersublattice 3*d*-4*f* exchange interaction (*J*PrCo) which is weaker by substitution of Pr for Ce.

A moderate magnetocaloric effect was found for all samples, with the maximum entropy change located at temperatures near the magnetic transition ones. Allthough the maximum value of the magnetic entropy changes decreases with increasing cerium content, moderate RCP(*S*) values were obtained for all samples due to the large δT_{FWHM} values.

Considering the possibility of choosing the appropriate concentration for constituents, to tune the transition temperature and the magnetocaloric effect, together with the high RCP(*S*) values and the broadened magnetic entropy curves, these materials are promising candidates for magnetic refrigeration devices.

REFERENCES

1. A.M. Tishin and Y.I. Spichkin, *The Magnetocaloric effect and its Applications, 1st ed., Institute of Physics* New York (2003).
2. V. K. Pecharsky, K. A. Gschneidner Jr., *International Journal of Refrigeration 29* (2006) 1239.
3. V.K. Pecharsky and K.A. Gschneider Jr., *J. Appl.Phys.* 85 (1999) 5365.
4. V.K. Pecharscky, K.A. Gschneider Jr., A.O. Pecharscky and A.M. Tishin, *Phys. Rev. B 64* (2001) 144406.
5. Ling-Wei Li, *Chin. Phys. B 25* (2016) 037502.
6. K.H.J. Buschow, *Reports on Progress in Physics* 40 (1977) 1179.
7. J.J.M. Franse, R.J. Radwanski, in*: K.H.J. Buschow (Ed.), Handbook of Magnetic Materials vol. 7 North-Holland Amsterdam* (1993) 307–501.
8. Guo Y, Li W and Feng W *Appl. Phys. Lett.* (2002) 86192513.
9. J.M.D. Coey, H. Sun, *Journal of Magnetism and Magnetic Materials* 87 (1990) L251.
10. G.C. Hadjipanayis, *Journal of Magnetism and Magnetic Materials* 200 (1999) 373.
11. L. Bessais, C. Djéga-Mariadassou, *Physical Review B 63* (2001) 054412.
12. J.W. Ross, J. Crangle, *Phys. Rev.* 133A (1964) 509.
13. T.F. Smith, H.L. Luo, M.B. Maple, I.R. Harris, *J. Phys*. F 1 (1971) 896.
14. R. Dudric, G. Souca, K. Kuepper, R. Tetean, *Physica Solidi Status B* (2018).
15. R. Tetean, E. Burzo, I.G. Deac, *JOAM* vol.8 (2006) 501-503.
16. H.M. Rietveld, *Journal of Applied Crystallography 2* (1969).
17. V. V. Burnasheva, V. V. Klimeshin, V. A. Yartys', and K. N. Semenenko, *Inorganic Materials, Neorganicheskie Materialy 15* (1979) 627.
18. K. Binder and A. P. Young, *Rev. Mod. Phys 58* (1986) 801.
19. J.A. Mydosh, *Spin Glasses: An Experimental Introduction (London: Taylor and Francis)* (1993).
20. P.A. Joy, P.S. Anil Kumar and S.K. Date, *J. Phys.: Condens. Matter 10* (1998) 11049-11054.
21. Nguyen Huu Duc *Handbook of Physics and Chemistry of Rare Earth 24* (1997).
22. J. Lyubina, O. Gutfleisch, M.D. Kuz'min, M. Richter, *J. Magn. Magn. Mater*. 320 (2008) 2252-2258.

STUDIA UBB PHYSICA, Vol. 63 (LXIII), 1-2, 2018, pp. 19-26
(RECOMMENDED CITATION)
doi:10.24193/subbphys.2018.02

FLUORESCENCE INVESTIGATION OF SOME POLYSTYRENE SAMPLES THERMALLY DEGRADED

CARMEN NICULAESCU[1], IOANA BREZESTEAN[1], CLAUDIU LUNG[1] AND MIHAI TODICA[1,*]

ABSTRACT. The behavior of some samples of commercial polystyrene, thermally degraded, was investigated by UV-VIS and fluorescence methods. Excited with different wavelengths in the domain 315-365 nm, the spectra show a peak located at 409 nm. The amplitude and the shape of this peak change after thermal degradation. Minor changes appear at 200ºC, indicating relatively stability of the samples, but the modifications are more important at 350ºC. At that temperature the samples are affected by oxidation.

Keywords: *polystyrene, thermal degradation, UV-VIS, fluorescence.*

INTRODUCTION

The destruction and the recycling of polymeric materials, without pollutant effects, is one of the important challenges concerning the efforts to preserve the natural environment. One of the simplest methods is the thermal degradation, but often this procedure is followed by the production of secondarily products with pollutant effects, and by dramatically modifications of the physical properties of the initial materials, [1 - 4]. One of the most popular polymers used for the fabrication of a large category of products,

[1] *"Babes-Bolyai" University, Faculty of Physics, M. Kogalniceanu No 1, 400084 Cluj-Napoca, Romania*
** Corresponding author: mihai.todica@phys.ubbcluj.ro*

packaging, and most recently for the thermal insulation of the buildings, is the polystyrene. It is known by very high chemical stability, resistance against a large category of solvent, good mechanical and thermal properties and low price of productions. However its large usage is accompanied by the production of huge amount of wastes which must be destroyed or recycling. Burning seems to be the simplest and cheap method of destruction, but this process can be accompanied by great modifications of the physical properties of the initial material. The aim of our study was the investigation by UV-VIS and fluorescence methods of the effects induced by this procedure.

EXPERIMENTAL

For this study we used samples of commercial polystyrene, with the same weight 10g, used as thermal insulation for building. A series of sample was heated 30 minutes at 200ºC, and another one at 350ºC. The samples were investigated by fluorescence methods with FP 8200 JASCO equipment, at different excitation wavelength, 315, 340 and 365nm. The UV-VIS investigation was done with Jasco V-670 system with scan speed 200 nm/min, UV VIS bandwidth 2 nm, and NIR bandwidth 8 nm.

RESULTS AND DISCUSSION

In order to establish the wavelength of the excitation radiation used for the fluorescence investigation we preceded to the UV-VIS analyzes.

Generally, the UV radiation causes the excitation of the electrons from a fully occupied orbital σ and π, or an unrelated orbital in connection with an unoccupied orbital orbital *n*, to an unoccupied antiorbital σ^* and π^*. In organic compounds, the most frequent transitions are $n \rightarrow \pi^*$ and $\pi \rightarrow \pi^*$, because these compounds contain frequently unsaturated groups with orbital π. [5 - 7]. For a large category of polymers the most important absorption is observed in the domain 200-300 nm, determined mainly by the $\pi \rightarrow \pi^*$ transition of the carbonyl groups, [7, 11]. In our case, at room

temperature, the UV-VIS spectrum of polystyrene shows a broad absorption peak centered at 263 nm, with a shoulder at 313 nm. Another peak, with smaller amplitude, is observed at 571 nm, (Fig. 1). The strong absorption in the domain 300nm nm suggests that the most suitable excitation for fluorescence emission should be located in this domain of wavelengths.

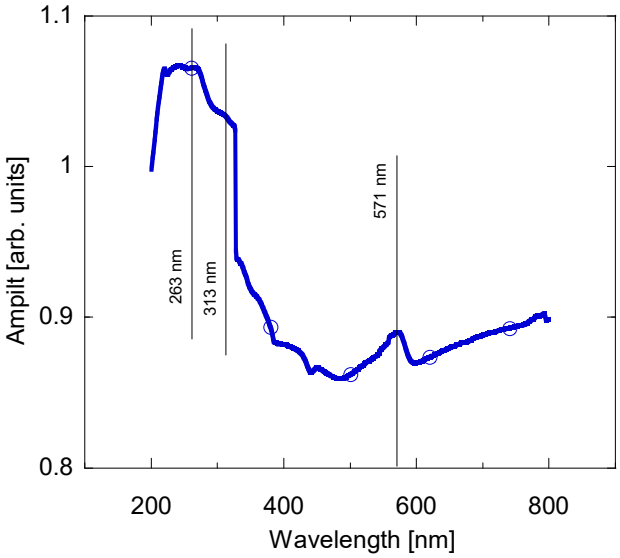

Fig. 1. The UV-VIS absorption of polystyrene at room temperature.

The fluorescence experiments involve the excitation of the electrons from theirs initial state to a high energy level by irradiation with a source of light with well defined wavelength. The return to the initial state can be realized directly by emission of a photon with the same energy as those of the exciting radiation, the resonant fluorescence, or by intermediate states, [7]. In this last case the transitions are accompanied by the emission of photons with energy smaller than those of the excitation. The excitation induces transitions between the lovest vibration level V_{00} of the fundamental state S_0 and one of the vibration level of the upper state V_1, in function of the energy of the incident photon $h\nu_0=\Delta W$. The non-radioactive return to the fundamental state involves transitions between the excited state V_{1*} of the state S_1 and the lowest vibration state V_{10} of the state S_1 through dissipative energy. The

energy is used for the excitation of othe vibration modes of the molecule, or by inner molecular friction. Further, the molecule come back to its fundamental state by transitions between the lovest level V_{10} of state S_1 and one of the levels V_{oi} of S_0 state with the emission of a fluorescence photon. Although the excitation is made all the time at the same wavelength, the position of the intermediate state V_{oi} is not all the time the same, that results in the broadening of the spectrum, [8, 9].

We analyzed first the samples in the initial state, using for excitation radiations with 315 nm, 340nm and 365nm wavelength. At 315nm excitation we can observe a broad fluorescence peak located in the domain 350 - 490nm, with a maximum at 409nm. We can observe also a shoulder at 390nm and another one at 470nm, (Fig. 2). The broadening of the spectrum in this domain suggests a large dispersion of the probabilities of transitions between the levels V_{10} of state S_1 and the levels V_{oi} of state S_0.

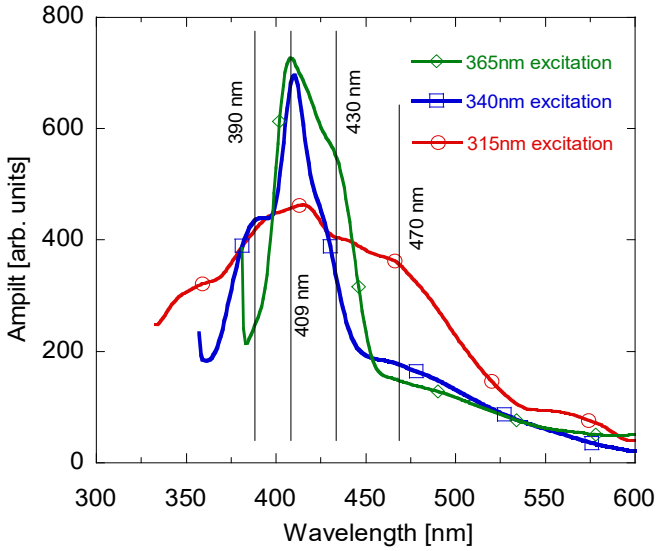

Fig. 2. The fluorescence spectra of polystyrene, at room temperature, excited at 315, 340 and 365m.

At 340nm excitation we can observe a fluorescence peak much narrow but higher, than those observed at 315nm excitation, with a maximum

at 409nm. A weak shoulder is observed at 470nm. The narrowing of the spectrum suggests a reduction of the dispersion of the probabilities of transitions between the levels of states S_1 and S_0. At 365nm excitation we observed a fluorescence peak with a maximum at 409nm and a shoulder at 430nm. This peak has almost the same amplitude as the peak observed at 340nm excitation, (Fig. 2). The high amplitude and the narrowing of the fluorescence peak suggest that the most efficient excitation corresponds to 340-365nm wavelength. On the same time we can observe that the position of the maximum of the fluorescence peaks remains unshifted even the excitation changes, in agreement with the theory, [7, 10].

After heating at 200ºC, some changes appear. At 315nm excitation we can observe a weak narrowing and a modification of the shape of spectrum compared with the spectrum obtained at room temperature. The maximum of the peak is observed at 385-390nm, close to the peak 390nm observed at room temperature. The relative amplitude of this peak, compared with the peaks observed at 340nm and 365nm excitation, increases. The shoulder at 470nm remains unshifted. At 340nm excitation we can observe a narrow peak at 409nm and a weak shoulder at 470nm. Except a small modification of the shape and amplitude of the peak, the spectrum is similar with those obtained at room temperature. At 365nm excitation we can observe a large peak centered at 424nm, which is the superposition of the peaks 409nm and 430nm observed at room temperature. Increase of the temperature has as effect the modification of the probabilities of transitions between the levels S_1 and S_0 associated to these peaks, followed by a modification of the intensities of these peaks. The apparent shift of the maximum of the resulting peak from 409nm to 424nm is due to the different contribution of the initial peaks 409nm and 430nm in the superposition. The amplitude of this peak is comparable with the amplitude of the peak 409nm obtained at 340nm excitation. A shoulder at 470nm is observed at the same position like in the case of the excitations at 315 and 340nm, (Fig. 3).

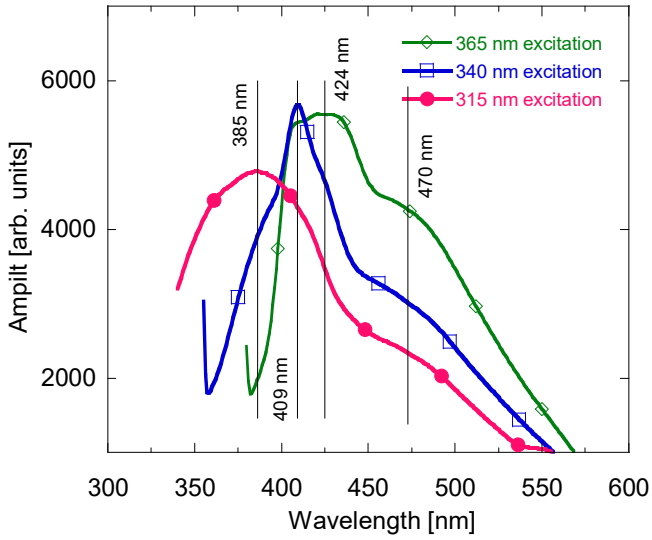

Fig. 3. The fluorescence spectra of polystyrene at 200ºC, excited at 315, 340 and 365m.

The amplitude of all the peaks increases compared with the amplitude at room temperature. However the position of the peaks, considering the effect of the superposition, remains unchanged after heating. We suppose that the electronic levels involved in these transitions are not affected by the heating process.

At 350ºC the general aspect of the spectra is similar to those obtained at room and 200ºC temperatures, except the amplitude of the peaks which is dramatically reduced. All the peaks appear unshifted in this spectrum, with weak modification of theirs shapes, (Fig. 4). All the excitations are followed by a fluorescence emission centered at 409nm. The shape of the peak is determined by the different contribution of the transitions between the states S_1 and S_0 to the fluorescence effect when the frequency of excitation changes. The superposition of the elementary peaks associated to these transitions give rise to the resulting fluorescence spectrum. Increase of the temperature induces modification of the probabilities of these transitions which is reflected by the modification of the general shape of the fluorescence spectrum.

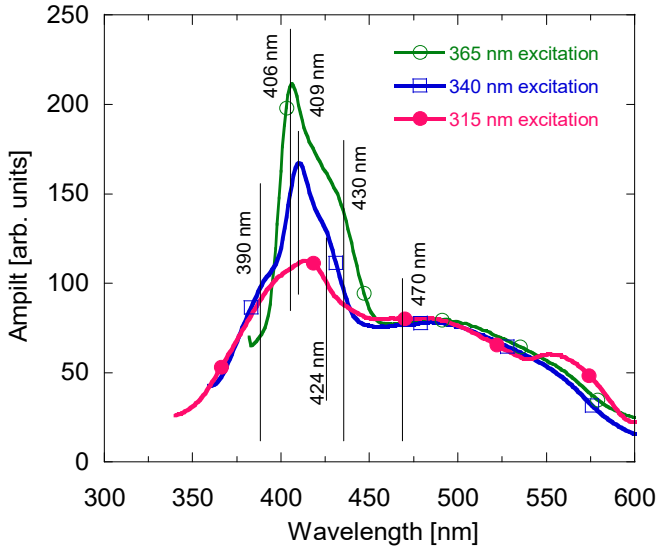

Fig. 4. The fluorescence spectra of polystyrene at 350ºC, excited at 315, 340 and 365m.

However the position of the fluorescence peak remains at 409nm, indicating the fact that the thermal treatment doesn't induced major changes on the electronic energy levels. Only the amplitude decreases with the temperature, fact associated with the irreversible degradation of part of the sample by oxidation. Observing the evolution of the fluorescence peaks in function of excitation we consider that the most stable and efficient fluorescence effect is obtained at 340nm excitation.

CONCLUSION

The behavior of some polystyrene samples thermally degraded was achieved by fluorescence investigation. The excitation was done at 315, 340 and 365nm, in accord with the UV-VIS absorption of these samples.

The fluorescence spectra of the polystyrene excited at different wavelengths contain peaks with widths and amplitudes depending on the frequency of excitation. This behavior is correlated with the probabilities of

transitions between the electronic levels involved in the fluorescence emission. The most important peak appears at 409 nm, whatever the frequency of the excitation, but its amplitude depends on the excitation. Taking into account the amplitude and the width of this fluorescence peak, we assume that the 340 nm is the most efficient excitation. Modifications of the fluorescence spectra appear after thermal treatment. The position of the peaks remains unchanged, but the amplitude and the width depend on the temperature. At 200ºC the general aspect of the spectra is similar to those obtained at room temperature, but at 350ºC the amplitude decreases dramatically. We correlate this behavior with the oxidation process of part of the sample. However the stable position of the fluorescence peaks suggests a great stability of the polystyrene even at high temperatures. This property can be taken into account for the recycling of these materials by thermal treatment.

REFERENCES

1. A. Martínez-Romo, R. González-Mota, J.J. Soto-Bernal, I. Rosales-Candel, Hindawi Publishing Corporation. Journal of Spectroscopy, 2015. Article ID: 586514.
2. M. Pop, S. Traian, L. Daraban, R. Fechete, Studia UBB Chemia, 56, 129, 2011.
3. X.F. Lu, J.N. Hay, Polymer, 42, 9423, 2001.
4. B. Demirel, A.H. Yaras, B.F. Elcicek, Bil Enst Dergisi Cilt, 13, 26, 2011.
5. Barbara Stuart, Polymer Analysis. Chichester (UK): John Wiley and Sons; 2002.
6. M. Rubinstein and R. Colby. Polymer Physics. Oxford (UK): Oxford University Press; 2002.
7. Joseph R. Lakowicz, Principles of Fluorescence Spectroscopy. Springer; 2006.
8. S. Garabagiu, C. Pestean, R. Stefan, Journal of Luminescence, 143, 271, 2013.
9. T. Iliescu, S. Pînzaru. Spectroscopia Raman şi SERS cu aplicaţii în biologie şi medicină. Cluj-Napoca: Casa Cărţii de Ştiinţa; 2011; ISBN: 978-973-133-887-3.
10. S. Aștilean, Metode și tehnici moderne de spectroscopie optică. Cluj-Napoca: Casa Cărţii de Ştiinţa; 2002
11. M. Todica, L. Udrescu, Cent. Eur. J. Phys., 9, 6, 2011.

STUDIA UBB PHYSICA, Vol. 63 (LXIII), 1-2, 2018, pp. 27-35
(RECOMMENDED CITATION)
doi:10.24193/subbphys.2018.03

READING X, Y COORDINATES WITH OPTICAL MOUSE AND SENDING DATA VIA INTERNET WITH NODEMCU-ESP8266

M. TODICA[1,*]

ABSTRACT. The work demonstrates the possibility to read the x, y coordinates of a moving object using an optical PC mouse and send the data to Android devices (smartphone or tablet) using the NodeMcu-ESP 8266 board. The system was used to control a small robot car with a smartphone via internet. The method can be usefully for didactic and scientific experiments.

Keywords: optical mouse, x, y coordinates, NodeMcu-ESP8266.

INTRODUCTION

Reading the x, y coordinates of a moving object is not a new idea, but achieving this task with simple, cheap and reliable materials represents an interesting challenge. Such kind of task is required for the control of the displacement of different mobile parts of complex mechanisms like industrial machines or robots, 3d printers, etc. Usually this operation is performed with different sensors like rotary encoders, ultrasound radars, optical switches, and so on, attached to the moving parts of the mechanical system [1-3]. The distance is measured by counting the number of passes

[1] *"Babes-Bolyai" University, Faculty of Physics, M. Kogalniceanu No 1, 400084 Cluj-Napoca, Romania*
** Corresponding author: mihai.todica@phys.ubbcluj.ro*

of the sensor in front of particularly points of a given stationary reference frame. Specific system of sensors for each application is requested. The accuracy is determined by the precision of the mechanical system of the sensors. For ordinary equipment this accuracy lies in the domain 0.1-1 mm. Better accuracy request very sophisticated and expansive mechanical devices, those used is justified only for complex machinery. However some times we need to obtain good accuracy with cheap equipment. A simple and reliable solution is the use of an ordinary PC mouse. The idea starts from the observation that every small displacement of the mouse on a smooth surface is followed by fine displacement of the cursor on the screen of the PC. The accuracy is of the order of hundreds or thousands dpi, depending on the quality of the mouse. This accuracy is enough to measure small displacements of different mechanisms or simple robots. The mouse is attached to the moving object without special adapters. The only requirement is to ensure continuous displacement of the mouse in front of a smooth fixed surface. It is possible to use for this job a mechanical or optical mousse, but the last one is less influenced by the errors determined by the motion or by the change of direction of the motion. It is the option chosen for his work.

Another feature required to the intelligent devices is the possibility to send and receive the data trough the internet. There are a lot of specific devices and protocols performing this task, but a simple solution is the use of the module ModeMcu ESP 8226 and Blynk application. We used this module and an optical mouse to read the x, y coordinates of a small robot car, controlled by smartphone via the internet. The work can be regarded as the starting point for the development of more complex equipments.

EXPERIMENTAL

The optical mouse used for this work contain the chip ADNS 2610, but other chips like ADNS 3610 or equivalent can be used. No special modifications of the mouse are requested. The useful information are collected directly from the pins SDIO (pin 3) and SCLK (pin4) of the chip

ADNS 2601, [4]. Because the mouse is +5V operating and the board NodeMcu supports only +3.3V signals, a logic level converter is intercalated between the chip and the NodeMcu board. The mouse is connected to high voltage pins and the NodeMcu to low voltage of the converter. The SDIO of the mouse is connected to the pin D1 and SCLK to pin D2 of NodeMcu. The +5V are available on the pin VU of NodeMcu. It is necessarily to connect the low pin LV of the logic converter to +3.3V and the HV pin to +5V,

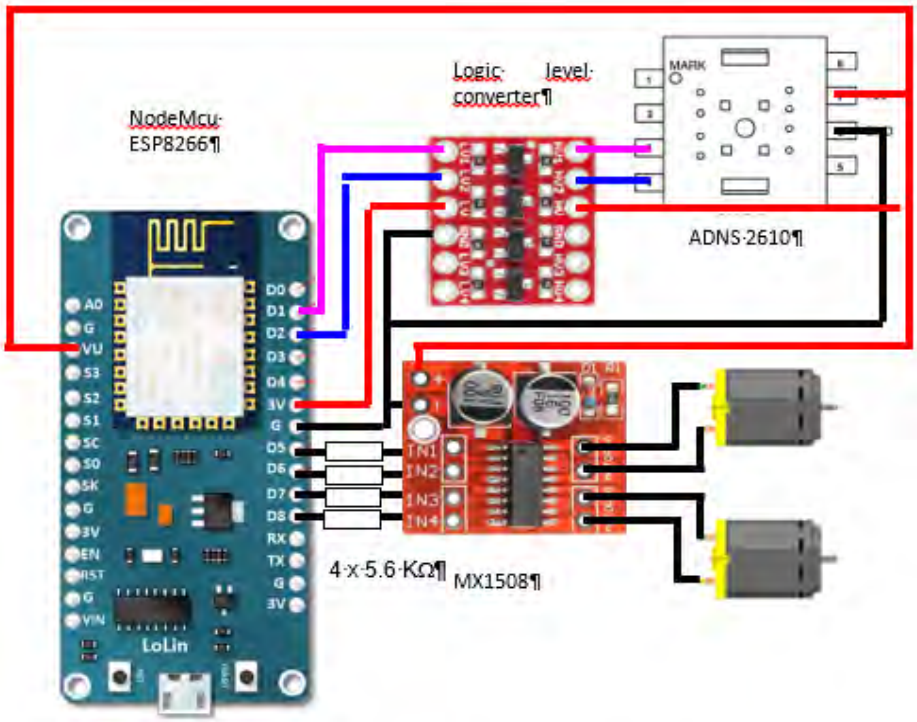

Fig. 1. Electrical diagram of the circuit

otherwise the converter is not working. The mouse was attached to a small car robot, driven by two DC motors. The motors are connected to the NodeMcu board trough a H bridge, (MX1508). The entries IN1, IN2, IN3 and IN4 of the bridge are connected to pins D5, D6, D7 and D8 of NodeMcu and the DC motors to the corresponding outputs of the bridge. The bridge and

the motors can be powered by the same source as the NodeMcu board, but for powerful motors we need separately source. In this case the pins + and - of the H bridge and the motors must be connected to this external source, but ensuring common ground with the NodeMcu board. The whole system is powered with +5V via USB port, or by external 5 - 9V connected to pins VIN and G of NodeMcu. The electric connections are shown in figure 1.

RESULTS AND DISCUSSION

The project is based on the properties of the optical mouse to identify every motion by comparing two successive images of the surface traveling in front of its camera. The difference between the images is transformed in x, y coordinates. The principle of work is well known and described in literature, [5]. For some mousse, especially the ancient ones, the rough x, y data are available before being processed by its own microcontroller, and before being sent to the PC. It is the situation of the chips ADNS 2610, 3610, etc. [4]. These data are sent to the NodeMcu board and processed by its microcontroller, CH 340, CP 2102, or equivalent. This microcontroller is compatible with Arduino platform and can be programmed using C+ language, [6, 7]. Programming the NodeMcu board request the installation of the Arduino IDE on the computer and the setting of the application to recognize and communicate with the NodeMcu board, [8, 9].

Brief description of the procedure is presented below:

- Download and install the version Arduino 1.6.8 or latter, [6].

- Add the information of the board ESP8266 to the Arduino. Open the Arduino IDE, go to the menu File/ Preference, and introduce into the box **Additional Boards Manager URLs,** the address of the board of JSON file ESP8266, http://arduino.esp8266.com/package_esp8266com_index.json.

- Manage the ESP library. In the Arduino IDE go to the menu Sketch/ Include Library/ Manage Libraries/ and add the Library of ESP8266.

- Select the NodeMcuESP8266 board. Go to menu Tools/ Board/ Boards Manager/. Select NodeMCU 1.0 (ESP-12E Module)

- Downoload and install **Blynk library** 0.4.0 from the official site, [10].

At this stage the Arduino is able to recognize and communicate with the board. To ensure the control of the robot car and the transmission of data trough the internet we must install the Blynk application on the smartphone, available on Google Magazin Play, and set the credentials of the internet router. The procedure is the follows:

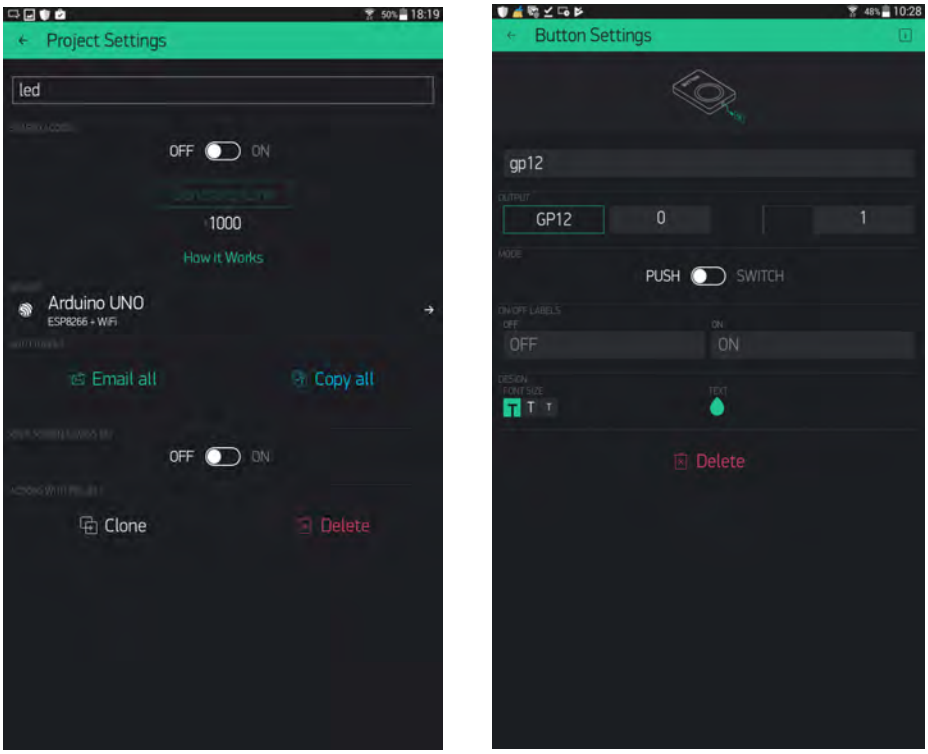

Fig. 2. Setting the Blynk workspace

- Open the app, create an account, enter a valid email address and the password, register, and **Sign Up**.

- Open new project, give it a name, creates the **auth. char** and send it to the above e-mail address. Select the **ESP8266 WiFi** board, (Fig. 2).

- Add the desired widgets to the workspace of the Blynk. For our project we used only four widgets buttons attached to digital pins GP 12,

13, 14 and 15, for the control of the two motors of the robot car, and one widget terminal on V12 displays the x, y coordinated of the mouse. The HIGH state is applied to the entries IN1 – IN4 of the H bridge when the buttons are pushed. So the two motors can be controlled separately or together, forward or backward, in any order. A supplementary widget button was added to virtual pin V1 for resetting the data sent by the mouse. Now the Blynk application is ready to control the NodeMcu board via internet.

In the next stage the board NodeMcu must be programmed. First we need to download the library **OptiMouse-master** from GitHub site and install it on the Arduino IDE, [11, 12].

Then we upload the below code:

The code.

```
//////////////////////
#include <ESP8266WiFi.h>
#include <BlynkSimpleEsp8266.h>
#include <SimpleTimer.h>
SimpleTimer timer;
char auth[] = "put there the auth. char of Blynk";
char ssid[] = "put there the SSID of the router";
char pass[] = "put there the password of the router";
#include "PAN3101.h"
#define SDIO D2
//attach SDIO pin of the mouse to D2 pin of NodeMcu
#define SCLK D1
//attach SCLK pin of the mouse to D1 pin of NodeMcu
PAN3101 Optical1 = PAN3101(SCLK, SDIO);
signed long x = 0;
signed long y = 0;

void setup()
{
Serial.begin(115200);
```

```
Optical1.begin();
Blynk.begin(auth, ssid, pass);
timer.setInterval(1000L, sendUptime);
delay(100);
}

BLYNK_WRITE(V1)
{
int Value = param.asInt();
//reset the data sent by the mouse when V1 widget is pressed
if (Value=1)
{
Serial.print("Reset prin V1 ");
x=0;
y=0;
Blynk.virtualWrite(12, " RESET ");
}
}

void sendUptime()
{
x += Optical1.dx();
y += Optical1.dy();
//optional, displays the data on the PC monitor
Serial.print("x=");
Serial.print(x, DEC);
Serial.print(" y=");
Serial.print(y, DEC);
Serial.println();
//displays the data on the smartphone
Blynk.virtualWrite(12, " X= ");
Blynk.virtualWrite(12, x);
```

```
Blynk.virtualWrite(12, " Y= ");
Blynk.virtualWrite(12, y);
}

void loop()
{
Blynk.run(); // Initiates Blynk
timer.run();
}
//////////////////////
End of the code.
```

It is necessarily to introduce in this code the **auth. char** of the Blynk project, the **SSID** and the **password** of the local internet router. Once the code was uploaded, the NodeMcu board can be disconnected from the computer and powered by external source. Open the project on the Blynk application on the smartphone and send commands to the motors by pushing the buttons GP12-15. When the robot car is moving, the mouse coordinates will be displayed on the widget terminal. By pushing the widget button V1 the data are resets.

CONCLUSION

The work demonstrates the possibility to read and send the x, y coordinates of the moving object trough the internet with very simple equipment. The displacement sensor is an PC optical mouse, which offer a resolution of the order of hundred dpi, and the connection to the internet is realized with the NodeMcu-ESP8266 board. With the application Blynk, a bilateral communication between the Android device, smartphone or tablet, and this board is established. This facility was used to control a small robot car with the Android device.

REFERENCES

1. I. Burda, Microprocesoare si microcontrolere, Presa Universitară Clujeană, Cluj-Napoca, **2002**, ISBN 973-610-046-4.
2. S. D. Anghel, Bazele Electronicii analogice si digitale, Presa Universitară Clujeană, Cluj-Napoca, **2007**, ISBN: 978-973-610-554-8
3. A Tunyagi, K Kandrai, Z Fülöp, Z Kapusi and A Simon, Phys. Educ. 53 (2018) 035028 (9pp)
4. www.efo.ru/components/avago/catalog/5988-9774EN.pdf
5. Richard F. Lyon, The Optical Mouse, and an Architectural Methodology for Smart Digital Sensors, Xerox Corporation, Palo Alto Research Center,
6. www.dicklyon.com/tech/OMouse/OpticalMouse-Lyon.pdf.
7. Arduino Website (www.arduino.cc/en/Guide/ Introduction)
8. T. A. Antal, Acta Technica Napocensis, Series: Applied Mathematics, Mechanics, and Engineering, Vol. 60, Issue I, March, (2017).
9. http://www.instructables.com/id/Programming-ESP8266-ESP-12E-NodeMCU-Using-Arduino-/
10. M. Todica, Controlling by smartphone via internet two relays with Blynk and ESP 8266-01, DOI: 10.13140/RG.2.2.31986.91847
11. Blynk Website: http://www.blynk.cc/getting-started/
12. https://github.com/zapmaker/OptiMouse,
13. Martijn The. http://www.martijnthe.nl/

STUDIA UBB PHYSICA, Vol. 63 (LXIII), 1-2, 2018, pp. 37-48
(RECOMMENDED CITATION)
doi:10.24193/subbphys.2018.04

DIGITAL DATA RECORDING OF TRANSIENT PHENOMENA IN RC CIRCUITS WITH ARDUINO

M. TODICA[1,*]

ABSTRACT. The work demonstrates the possibility to acquire data from any physics experiment using very simple equipment, Arduino Uno and Processing software. The algorithm was tested to record data of transient phenomena in RC circuits. Despite its simplicity the method provides accurate and reliable data, being usefully for didactic and scientific experiments.

Keywords: *digital data recording, RC transient phenomena, Arduino Uno.*

INTRODUCTION

Recording digital data from scientific experiment, simple or complex, is today a common stage performed with dedicated equipment. Generally the strategy of data recording is implemented into the recording equipment following specific protocols, which cannot be modified by the user. In these cases the experimental data can be collected quickly without special skills requested to the user, [1-4]. The simplicity of the use can lead to incomplete understanding of the procedure, and to the impossibility to adjust or to improve the parameters of the acquisition. Understanding the protocol of digital data acquisition, and implement this procedure for some physics

[1] "Babes-Bolyai" University, Faculty of Physics, M. Kogalniceanu No 1, 400084 Cluj-Napoca, Romania
**Corresponding author: mihai.todica@phys.ubbcluj.ro*

experiments, using simple equipments, represents the aim of this work. We propose a simple method for digital data recording using a common computer, the software Processing, available free on the internet, and the very popular programmable board, Arduino Uno. The method has been tested to record data of the transient phenomena in RC circuits. The main advantage of the method is its simplicity, economy of resources, and the availability for a large category of users. The method provides accurate and reliable data, being useful for didactic and scientific experiments.

EXPERIMENTAL

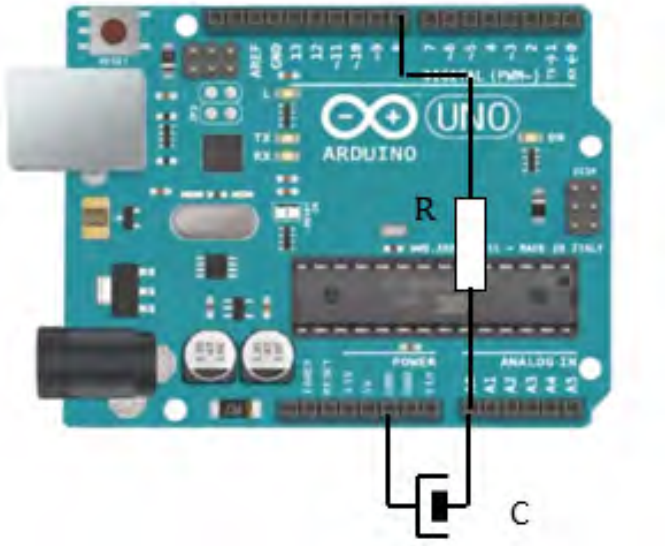

Fig. 1. RC circuit connected to the Arduino board

We used for this work the Arduino Uno board, which is a powerful programmable controller, easy to code with Arduino IDE, (C++ language). The board has many digital pins, which can be set as entries or outputs, and many analog pins which can be set as entries. The digital IN/OUT pins accepts and provides TTL signals, at low impedance. The analog pins are high impedance and accept signals up to +5V. The analog signals are converted to

digital on the range 0-1023 points, so that the data must be mapped from 1024 points to 5V if we want to have decimal output of the entry signal. For this project we used only one analog entry, A_0, which is connected to one end of the capacitor in order to measure the voltage at its ends. Due to the high impedance, we can neglect the influence of this entry on the measuring process. The RC circuit consists of a 24 μF capacitor connected between the ground and digital pin D_8 trough a resistor R=470 KΩ. The circuit is presented in figure 1. The recorded data are displayed using an ordinary computer and Processing software, available free on the internet, [5]. The data are displayed on the processing windows and then can be copied and processed with Origin, Kaleidagraph or other software for mathematically analyze.

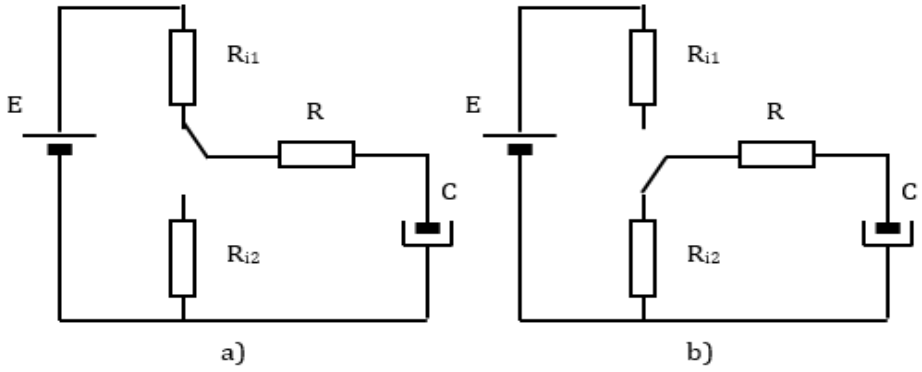

Fig. 2. RC charging-discharging equivalent circuits.
a) charging circuit; b) discharging circuit

RESULTS AND DISCUSSION

In the high state the pin D_8 is connected to +5V trough a low inner resistance R_{i1} of the Arduino board, and the capacitor C is charged via the resistors R and R_{i1}. The schema of the equivalent charging circuit is presented in figure 2a. The voltage on the capacitor is described by the equation, [6, 7]:

$$U_C(t) = E\left[1 - exp\left(\frac{-t}{R_{ch}C}\right)\right] \quad (1)$$

where *E* is the maximum voltage of the charging source, (in our case E=5V), *C* is the capacitance of the capacitor and R_{ch} the total charging resistance, (in our case $R_{ch} = R_{i1} + R$). In the low state the pin D_8 is connected to the ground trough the low inner resistor R_{i2}, (Fig. 2.b). The voltage of the capacitor is described by the equation:

$$U_C(t) = U_1\, exp\left(\frac{-t}{R_{dch}C}\right) \quad (2)$$

where U_1 is the voltage of the capacitor at the start moment of the discharging process, and R_{dch} the total discharging resistance, (in our case $R_{dch} = R_{i2} + R$). The inner resistances R_{i1}, R_{i2}, of the Arduino board are small compared with the charging-discharging resistance *R* and can be neglected. Then we can rewrite the equations 1 and 2 as follows:

$$U_C(t) = E\left[1 - exp\left(\frac{-t}{RC}\right)\right] \text{ and } U_C(t) = U_1\, exp\left(\frac{-t}{RC}\right) \quad (3)$$

When the code is running the pin D_8 is set up and down repeatedly ensuring the charging and discharging of the capacitor. The charging and discharging times, expressed in milliseconds, are described in IDE code by the variable *interval A*. These times are set equals, otherwise one of the processes, charging or discharging should be dominant and the system should reach a limit state, saturation charging, or completely discharging. The sampling time is defined by the variable *interval B*. We can change these parameters in order to obtain the best charging-discharging curves. To start the experiment we connect the Arduino board to the PC via USB port, we open the Arduino IDE, select the right Port, (to which the Arduino board is connected), and upload the following code.

```
//Arduino code

int AnalogPin0 = A0;
int ledState = LOW;
unsigned long previousMillisA = 0;
unsigned long previousMillisB=0;
unsigned long time=0;
const long intervalA = 20000; //charging time
const long intervalB = 1000; //sampling time
int led = 8; //charging-discharging pin

void setup()
{
Serial.begin(9600);
pinMode(led, OUTPUT);
}

void loop()
{
unsigned long currentMillisA = millis();
unsigned long currentMillisB = millis();
unsigned long time = millis(); //time counter
if (currentMillisA - previousMillisA >= intervalA)
{
previousMillisA = currentMillisA;
if (ledState == LOW)
{
ledState = HIGH;
} else
{
ledState = LOW;
}
```

```
digitalWrite(led, ledState);
}
if (currentMillisB - previousMillisB >= intervalB)
{
int Uc = analogRead(AnalogPin0);
Serial.print(Uc, DEC);
Serial.print(","); //send data to Processing
Serial.print(time);
Serial.print(".");
previousMillisB = currentMillisB;
}
}

//End of Arduino code.
```

The charging-discharging time and the voltage of the capacitor are sent to Processing via serial port. Processing is used only to display the data, the time and U_C. To do this we open Processing software and we upload the next code. We must set exactly the same port as set in the Arduino code.

```
//Processing code
import processing.serial.*;
PFont F;
Serial myPort;
String Uc="";
String SentTime="";
String data="";
int iSentTime;
float iUc;
int index1=0;
```

```
void setup()
{
F = createFont("Arial", 18, true);
size (1000, 600);
smooth();
myPort = new Serial(this,"COM5", 9600);
//change the port according to your Arduino
myPort.bufferUntil('.');
}
void draw()
{
line(50, height-50,width-50,height-50);
line(50, height-50,50,50);//draw frame axis with origin in (50;50)
textFont(F);
fill(20);
text("Uc (V)",70,40);
text("time (ms)",width-100,height-20);
text("RC transient",500,40);
fill(255,200,0);
ellipse(iSentTime+50, height-iUc*height/1023-50,10,10);
//displays time and Uc data

if (iSentTime >= width)
{
iSentTime=iSentTime-width;
background(200);
//refresh the screen when time exceeds the width
}
}

void serialEvent (Serial myPort)
{
```

```
data = myPort.readStringUntil('.');
data = data.substring(0,data.length()-1); //read the data from the string
index1 = data.indexOf(",");
Uc= data.substring(0, index1);
SentTime= data.substring(index1+1, data.length());
iUc=float(Uc);
iSentTime = int(SentTime)/100;
print(SentTime,",");
println(iUc*5/1023); //maps data from 0-1023 points to 0-5V
}
//End of Processing code.
```

The real data of charging-discharging, processed with Processing, are presented in figure 3. The data, in decimal form, are displayed on the windows working area of Processing, can be copied and then processed

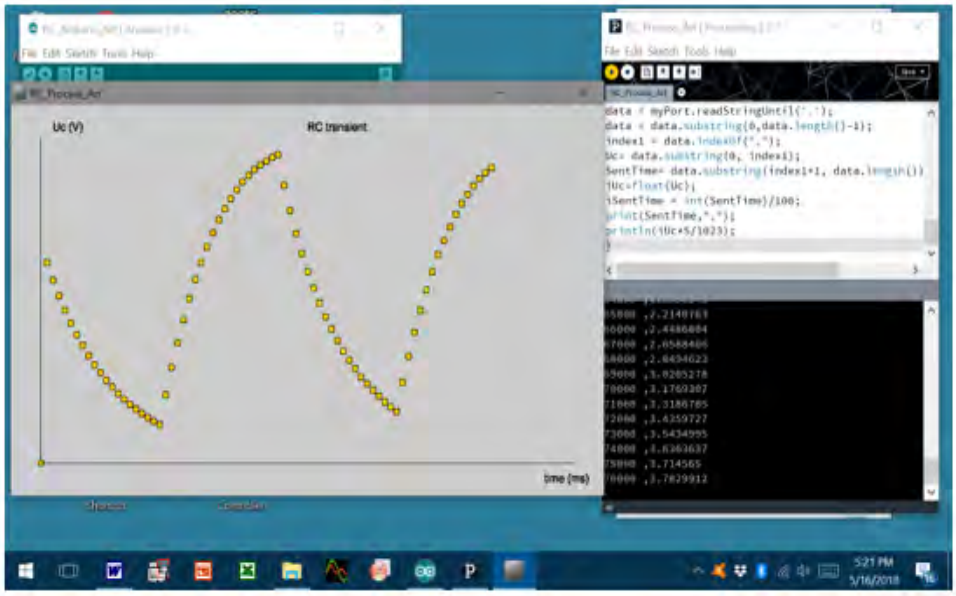

Fig. 3. Print screen of the working area of Processing. The data Uc and time are displayed on the working windows of Processing.

with specific software. The plot of recorded data with Kaleidagraph is presented in figure 4. Both curves, charging and discharging, represent exponential curves. However for quantitative analyze the discharging curve is most useful, allowing direct and very accurate measure of time constant $\tau = RC$. We can fit the experimental discharging data with the equation (3), but more suggestive is the following representation [8]:

$$ln\left(U_C\right) = ln\left(U_1\right) - \frac{t}{RC} \tag{4}$$

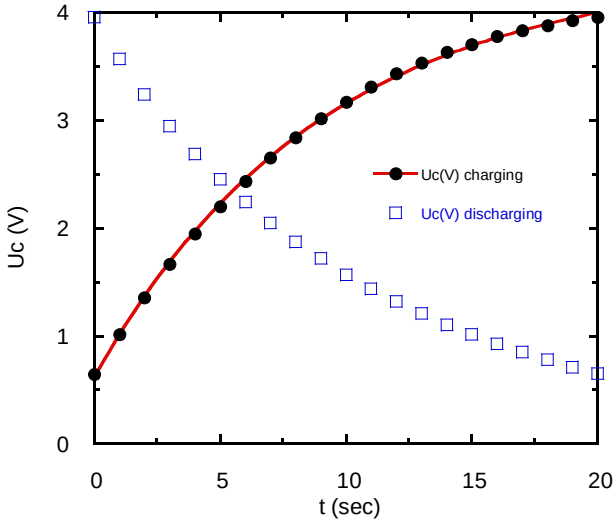

Fig. 4. The experimental data $U_c(t)$ of charging-discharging process. The charging data are fitted with equation 7.

We obtain a straight line with the intercept $ln\left(U_1\right)$ and the slope $-\frac{1}{RC}$, (Fig. 5). From here we found $U_1 = 3.9V$. We can see that the slope of the line is not affected by the value of the initial voltage U_1 of the capacitor. We found the value $\tau_{exp} = 11.22s$ in good agreement with the theoretical value $\tau_{theor} = 11.28s$ obtained with the known values C=24 μF and R=470 KΩ. The accuracy of calculation is 0.17%.

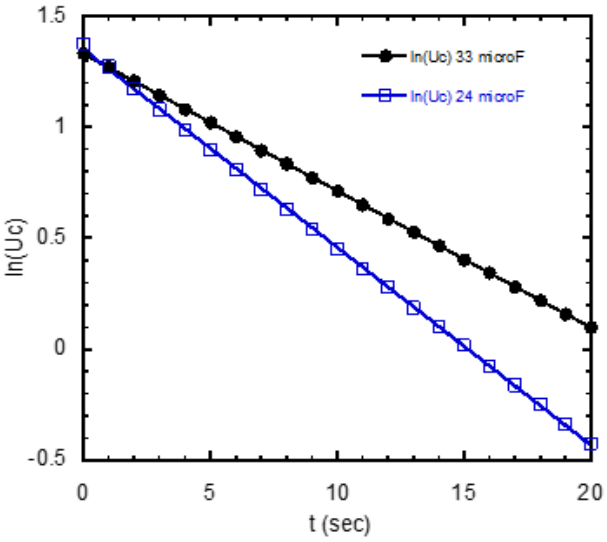

Fig. 5. Logarithmic representation of the discharging voltage of the capacitor for C=24 μF and C=33 μF.

The analyze of charging data is more complicate and gives less accurate values for the time constant. The equation 3 describes the charging process starting from zero voltage of the capacitor, (completely discharged). In our experiment the discharging process is not completely, so that the charging process starts from a given voltage U_{C0}. This voltage can be expressed considering the charging process starting at *t = 0* and ending at time t_0. The process is described by the equation:

$$U_{C0} = E\left[1 - exp\left(\frac{-t_0}{RC}\right)\right] \tag{5}$$

In our experiment we start the measurements at t_0 and stop the recording data at the instant *t*, when the voltage of the capacitor is $U_C(t)$.

We doesn't known the value of t_0, we can measure only the time interval $\Delta t = t - t_0$ from the start to the stop of the charging. The voltage $U_C(t)$ of the capacitor at the instant *t* is given by the equation:

$$U_C(t) = E\left[1 - exp\left(\frac{-(t_0 + \Delta t)}{RC}\right)\right] \tag{6}$$

Combining equations (5) and (6) we found the relation which describes the voltage of the capacitor during the charging from U_{C0} to $U_C(t)$.

$$U_C(t) = \frac{U_{C0}}{\left[1 - exp\left(\frac{-t_0}{RC}\right)\right]}\left[1 - exp\left(\frac{-(t_0 + \Delta t)}{RC}\right)\right] \tag{7}$$

U_{C0}, t_0, and $\tau^*_{exp} = RC$ are unknown parameters. We can fit the experimental data with equation (7), (Fig. 4). We obtained the value $\tau^*_{exp} = 9.04s$ smaller than the theoretical value $\tau_{theor} = 11.28s$. The accuracy of this method of is 19%, much small that the previous method. The source of errors is given by the great number of unknown parameters, three. In conclusion we can affirm that the method of discharging is the best way to calculate the time constant *RC*. To validate ours hypotheses we repeated the experiment with another capacitor *C*=33 μF*. Using the discharging protocol we obtained the value $\tau_{exp} = 16.2s$ and $U_1 = 3.8V$, (Fig. 5). Compared with the theoretical value $\tau_{theor} = 15.5s$ we obtained an accuracy of 4.5%. With equation (7) we found $\tau^*_{exp} = 15.8s$ that means an accuracy of 1.9%. In this case both algorithm of calculation provide good values for the time constant. Taking into account the obtained results, we suggests to apply both algorithms of analyze and average of the data.

CONCLUSION

The work demonstrates the possibility to use very simple equipment for digital data acquisition from physics experiments. We applied the method to collect the data from the transient RC experiment, but the protocol can be applied to other experiments. The method allows quantitative calculation of the parameters of the charging-discharging phenomena in RC circuits. The method is based on the use of very simple equipment, Arduino Uno board, and free software processing available on the internet. Despite its simplicity the method can be used for didactic and scientific experiments, providing accurate and reliable data.

REFERENCES

1. S. D. Anghel, Bazele Electronicii analogice si digitale, Presa Universitară Clujeană, Cluj-Napoca, **2007**, ISBN: 978-973-610-554-8
2. I. Burda, Microprocesoare si microcontrolere, Presa Universitară Clujeană, Cluj-Napoca, **2002**, ISBN 973-610-046-4.
3. D. Rădoiu, G.D. Popescu, Introducere în ştiinţa sistemelor de calcul, Editura Universităţii "Petru Maior", Târgu-Mureş, **1999**, ISBN 973-98726-7-0
4. A. Nicula, M. Todica, G. Buzas, S. Astilean, I. Berindean., Studia, Univ. "Babes-Bolyai", Physica, XXXIII, 2, (1988), pg. 15-19.
5. https://processing.org/download/
6. R. M. Eisberg, L. S. Lerner, Physics Foundations and Applications, McGraw-Hill, London, **1982**, ISBN 0-07-066268-1.
7. B. M. Yavorsky and A. A. Pinsky, Fundamental of Physics, Mir Publishers, Moscow, **1987**.
8. M. Todica, C. V. Pop, Fizica generala aplicata, Presa Universitara Clujeana, Cluj-Napoca, **2007**, ISBN (10)973-610-498-2; ISBN (13) 978-973-610-498-5

STUDIA UBB PHYSICA, Vol. 63 (LXIII), 1-2, 2018, pp. 49-60
(RECOMMENDED CITATION)
doi:10.24193/subbphys.2018.05

^{1}H NMR RELAXOMETRY AND ATR-FT-IR SPECTROSOPY USED FOR THE ASSESMENT OF WASTEWATER TREATMENT IN SLAUGHTERHOUSE

R. CRAINIC[1], L. R. DRĂGAN[1], R. FECHETE[1,2,*]

ABSTRACT. Advanced ^{1}H NMR relaxometry based on fast Laplace inversion analysis combined with ATR-FT-IR spectroscopy, pH, electric conductivity and TDS (total dissolved solids) measurements were used to assess the purification process for chicken slaughterhouse wastewater. The ^{1}H NMR T_2-distribution (able to separate the effect of dissolved pollutants from undissolved pollutants), various integrated areas of IR spectra, the behavior of pH, electric conductivity and TDS show an efficient purification treatment for chemically treated water and evacuated water.

Keywords: *^{1}H NMR relaxometry, T_2-distribution, ATR-FT-IR spectroscopy, wastewater monitoring, slaughterhouse.*

INTRODUCTION

Large volume of water (15 000 - 20000 L per 1000 birds) is consumed daily into a chicken slaughterhouse along the entire production line. Unfortunately, this water consumption leads to an intense poultry process,

[1] *Technical University of Cluj-Napoca, Faculty of Material and Environmental Engineering, B-dul Muncii 103-105, Cluj-Napoca, Romania*
[2] *Babeş-Bolyai University, Faculty of Physics, 1 Kogălniceanu str., 400084 Cluj-Napoca, Romania*
[*] *Corresponding author: rfechete@phys.utcluj.ro*

since the resulted water is loaded with organic matters and can no longer be returned to the environment, usually via effluents [1, 2]. Therefore, purification treatments of wastewater before evacuation are mandatary. Regular methods largely used to monitor the wastewater purification process are based on the global measurements of apparent color, turbidity, electric conductivity (EC), total suspended solids (TSS), total dissolved solids (TDS), pH, chemical oxygen demand (COD), and ammoniacal nitrogen (NH3-N).

The aim of this work is to implement and to use advanced methods like: i) ^{1}H NMR relaxometry combined with FLI (fast Laplace inversion) analysis and ii) ATR-FT-IR spectroscopy to assess the efficiency of the wastewater treatment process starting with the untreated water up to evacuated water passing through biologically and chemically treated water. The resulted sludge is also characterized. The main advantage of the use of ^{1}H NMR relaxometry method is the fact that by FLI analysis the distribution of microscopic parameters like transverse relaxation time (T_2) is obtained. This allows the discrimination between dissolved and undissolved solids (pollutants) which further can be differentiated by their degree of mobility. Finally, the results are compared with the classic measurements of pH, electric conductivity and total dissolved solids (TDS).

EXPERIMENTAL

The wastewater samples (untreated water, biologically treated water, chemically treated water, evacuated water and sludge) were collected from a chicken slaughterhouse from the north of the Transylvania, stored into 0.5 l plastic container, transported to Technical University of Cluj-Napoca and measured as soon as possible. Before each measurement the samples bottles were agitated to homogenize the content. We started with the measurement of the pH, electric conductivity and totally dissolved solids (TDS), then with ^{1}H NMR measurements and at the end we finish with the FT-IR spectroscopy. Between measurements the samples were stored in dark at room temperature.

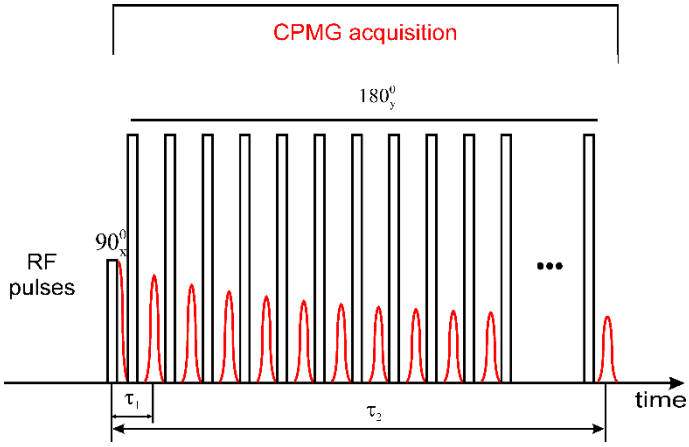

Fig. 1. The CPMG pulse sequence used for the [1]H NMR data acquisition.

The [1]H NMR relaxometry measurement of all wastewater samples was performed using a Bruker Minispec MQ 20 spectrometer (19.69 MHz working frequency) using the well knows CPMG pulse sequence (see Fig. 1) with echo time τ_1 = 5 ms. A number of 3000 echoes were registered. The recycle delay (RD) was set at 3 s and a number of 32 scans were acquired. The data were then processed using a fast Laplace-like inversion algorithm, intensively used in the last years to analyze multi-exponential decay curves [3-10].

The FT-IR spectra were recorded using a Jasco 6200 FT-IR spectrometer. For our liquid samples the ATR (attenuated total reflection) accessory was used and the ATR correction was performed for each spectrum. For background we use distilled water. The spectrometer set-up was as follow: i) the start wavenumber $\tilde{\nu}$ was 349.053 cm^{-1} but due to the noisy data at low wavenumber values the spectra were cutoff at 700 cm^{-1}; ii) the end $\tilde{\nu}$ was 4000.6 cm^{-1}; iii) to increase the signal to noise ratio (SNR) a number of 64 scans were accumulated; iv) the resolution was 4 cm^{-1}; v) a zero filling procedure was enabled and a cosine apodization procedure was performed; vi) the auto gain was set at 8, the auto aperture was 7.1 mm and the auto filter was 10 kHz; vii) the scanning speed was 2 mm/sec.

RESULTS AND DISCUSSION

The CPMG decay curves recorded for the slaughterhouse wastewater and sludge in the month 2 of monitoring are presented in Fig. 2a. One can observe a fast decay curve corresponding to biologically treated water indicating the presence of components with a reduced mobility. The slowest decay CPMG curve is obtained for the untreated water. A large superposition is observed between CPMG decays belonging to chemically treated water and evacuated water, suggesting that these samples have similarly properties. A slightly faster decay was obtained for the sludge resulted from wastewater treatment. As they are, these curves are hard to be further interpreted. A proper way of interpretation of the specific relaxometry data is via the analysis of the T_2-distribution obtained from CPMG decay, assumed to be multi-exponential [6-10].

The ^{1}H NMR T_2-distributions measured for the untreated water, the biologically and chemically treated water, the evacuated water and sludge resulted from treatment process are presented in Fig. 2b. The transverse relaxation

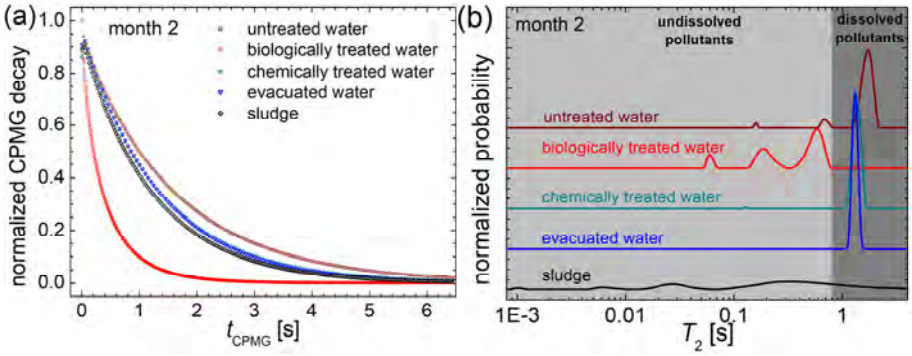

Fig. 2. (a) The ^{1}H NMR CPMG echo trains decays measured for the chicken slaughterhouse wastewater and sludge in the month 2 of monitoring; (b) The corresponding T_2-distributions.

times specific to wastewater were obtained in the range from ~ 50 ms up to 2.3 s. The untreated water and the biologically treated water are characterized by tree peaks, the chemically treated water is characterized by a main peak located at large T_2 values ($T_2 \cong 1.35$ s) and a very small peak located at small T_2

values ($T_2 \cong 128$ ms). The evacuated water is characterized by only one peak located at large T_2 values. With the exception of month 1 of monitoring, where for the untreated water and biologically treated water four peaks are observed, for the month three and four of monitoring only three peaks were also observed.

For the interpretation of these distributions the full T_2-distributions domain was spitted in two subdomains and associated, base on our experimental expertise on this subject, to: i) the domain of dissolved pollutants in water for T_2 values larger than 800 ms and ii) the domain of undissolved pollutants in water for T_2 values smaller than 800 ms. In our experimental set-up the distilled water is characterized by the most probable relaxation time T_2 value (at the peak maximum) of 2.4 s [4]. The dissolved solids with paramagnetic properties will lead to a decrease of this T_2 value. This decay is proportional with the content of dissolved solids but is also dependent on the pollutant nature. Nevertheless, one can say that a pure water is characterized by a large T_2 value.

The peaks that appear in the T_2-distributions in the domain of undissolved pollutants can be assigned to water molecules attached to solids of various sizes having then different mobility. Flotation and sedimentation processes of pollutants were observed at a simplest visual inspection. It is natural to associate the large T_2 value with more mobile water molecules hence with small undissolved pollutants. The medium mobile water molecules attached to medium size undissolved solids are characterized by peaks with T_2 values in the range of ~ 60 ms to ~ 170 ms. For month 1 of observation the T_2-distributions (not shown here) presents four peaks for untreated water and biologically treated water samples. There the fourth peak appearing to the smallest T_2 values (in the range of 45 – 47 ms) were associated with the less mobile water molecules attached to the largest pollutant particles.

In all 4 mounts of monitoring the T_2-distributions measured for the sludge are characterized by four peaks. These can be found in the range from ~ 0.9 ms up to ~ 515 ms. The peaks are more broaden compared to the peaks belonging to wastewater, regardless of the stage of treatment process, suggesting a more heterogeneous environment.

Further, in this paper the largest T_2 values characterizing the more mobile water pools (which may contain only dissolved pollutants) will be labeled as $T_{2,1}$ (see Fig. 3). The next peaks going from largest to smaller T_2 values (from right to left in Fig. 2b) are labeled, in order, with $T_{2,2}$, $T_{2,3}$, and $T_{2,4}$.

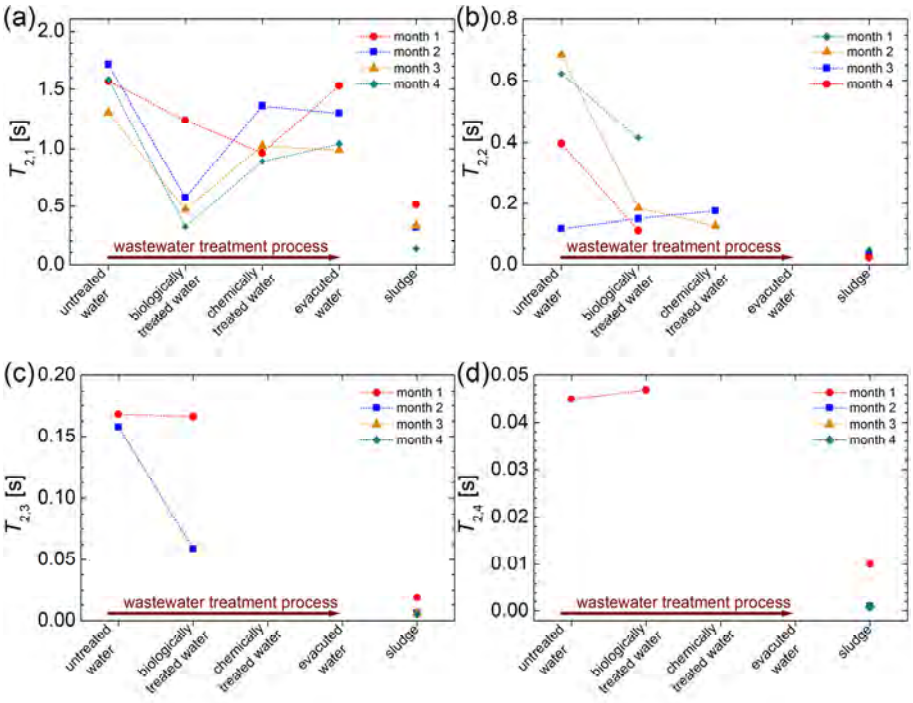

Fig. 3. The values of most probable transverse relaxation times associated to (a) dissolved pollutants ($T_{2,1}$); (b) most mobile water ($T_{2,2}$); (c) medium mobile water ($T_{2,3}$) and (d) water with restricted mobility ($T_{2,4}$) measured for the slaughterhouse wastewater (untreated water, biologically treated water, chemically treated water and evacuated water) and sludge for all four months of monitoring.

From the integral area under the peaks, which is proportional with the number of protons (^{1}H) mainly from each specific water pools, one can say that the untreated water is characterized (see Fig. 2b) by: i) a large amount of water with dissolved pollutants; ii) some undissolved pollutants with small dimensions and large mobility and iii) a small number of undissolved pollutants with medium size/mobility. As a result of biologically treatment

the peak characterized by the largest T_2 value ($T_{2,1}$) is found at the most lower values (see Fig. 3a) indicating that a large amount of pollutants were decomposed and dissolved in water. Other significant components of biologically treated water (see the relative area of peaks of the red distribution in Fig. 2b) are pollutants with reduced mobility of small and medium sizes (see the decay of $T_{2,2}$ in Fig. 3b and $T_{2,3}$ in Fig. 3c).

The efficiency of chemically purification treatment can be observed by the insignificant amount of proton signals associated with water molecules attached to the undissolved pollutants (see the dark cyan distribution in Fig. 2b). Such small amount of water with undissolved pollutants was measured in the months two and three of monitoring as can be seen from the existence of $T_{2,2}$ data in Fig. 3b. Also the increase of $T_{2,1}$ values for chemically treated water compared to those measured for biologically treated water indicates that the chemical treatment applied by the chicken slaughterhouse in this stage is efficient. The evacuated water in all four months of monitoring contain only a small amount of dissolved pollutants (see the $T_{2,1}$ values in Fig. 3a) while no water with undissolved pollutants was observed (lack of data for $T_{2,2}$ - $T_{2,4}$ in Figs. 3b to 3d).

In general all four T_2 values measured for sludge are smaller than the corresponding values measured for the wastewater (see Figs. 3). There is one exception where the $T_{2,1}$ values measured for sludge are comparable with those measured for biologically treated water. This is an indication of some similarities between the composition of water with dissolved pollutants from sludge and biologically treated water, which was also observed in the ATR-FT-ITR spectra. Such spectra were measured for samples obtained in months 2, 3 and 4 and are presented in Fig. 4.

At a visual inspection, the efficiency of the purification treatment process can be assessed from the overall spectral intensity. For the months 3 of monitoring the decay in the overall spectral intensity is not obvious. One can remark the relative decay of peak doublet located at ~ 2852 cm^{-1} and ~ 2920 cm^{-1} compared to the broad peak found between 2600 cm^{-1} and 3290 cm^{-1}. Contrary for the months 2 and 4 of monitoring the overall intensity of wastewater decay from untreated water (bottom spectra with wine color in

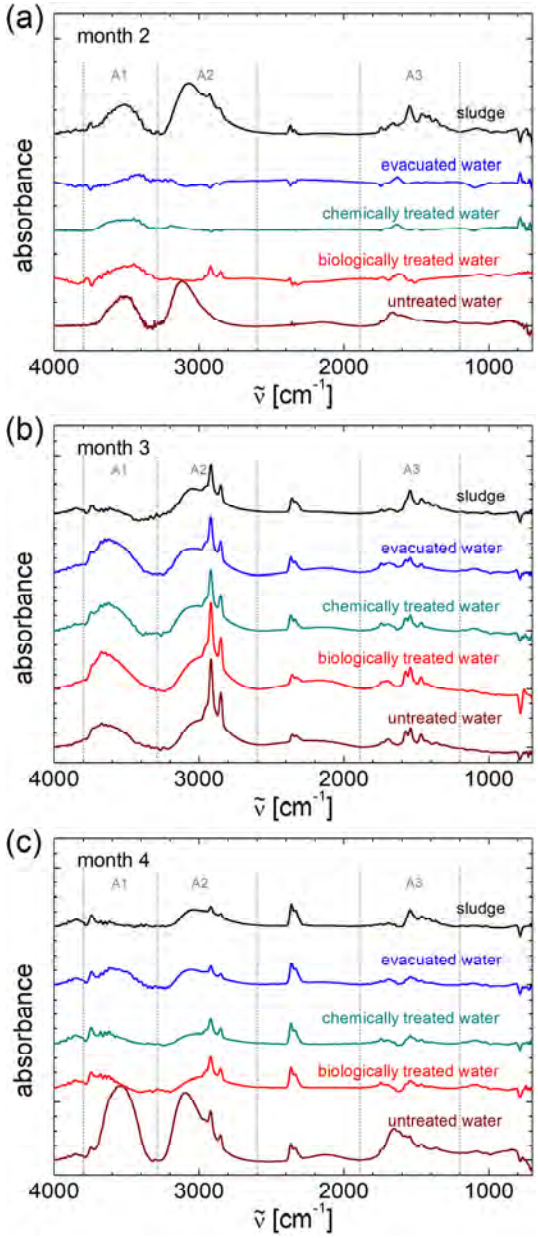

Fig. 4. The ATR-FT-IR spectra of measured for the slaughterhouse wastewater (untreated water, biologically treated water, chemically treated water, evacuated water) and sludge in the (a) second; (b) third and (c) forth month of monitoring.

Figs. 4) to evacuated water (spectra with blue line). As example, for the evacuated water sample obtained in month 2 one almost no absorption is observed. The sludge samples present similar features with the water samples since only the wet part could be measured.

The standard spectral analysis is hard to be interpreted since the pollutants are constituted from many types of organic matter. Therefore, the ATR-FT-IR spectra are divided in three specific regions as can be seen from Fig. 4 where light gray dashed lines delimitated the limits. The integral areas were calculated for these three domains as: i) A1 for the wavenumber domain from $\tilde{\nu}$ = 3290 cm^{-1} to $\tilde{\nu}$ = 3800 cm^{-1}, graphically represented in Fig. 5a; ii) A2 for $\tilde{\nu}$ = 2600 cm^{-1} to $\tilde{\nu}$ = 3290 cm^{-1}, graphically represented in Fig. 5b and iii) A3 for the wavenumber domain from $\tilde{\nu}$ = 1200 cm^{-1} to $\tilde{\nu}$ = 1890 cm^{-1}, graphically represented in Fig. 5c.

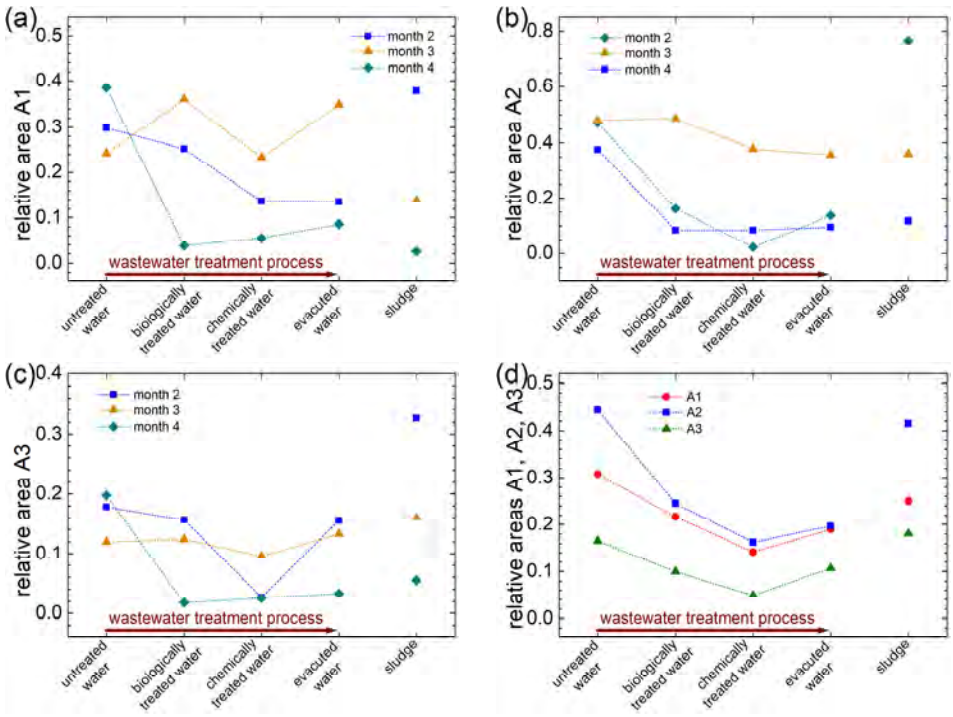

Fig. 5. The areas (a) A1; (b) A2 and (c) A3 as were defined for ATR-FT-IR spectra represented in Fig. 4 for the slaughterhouse wastewater and sludge.

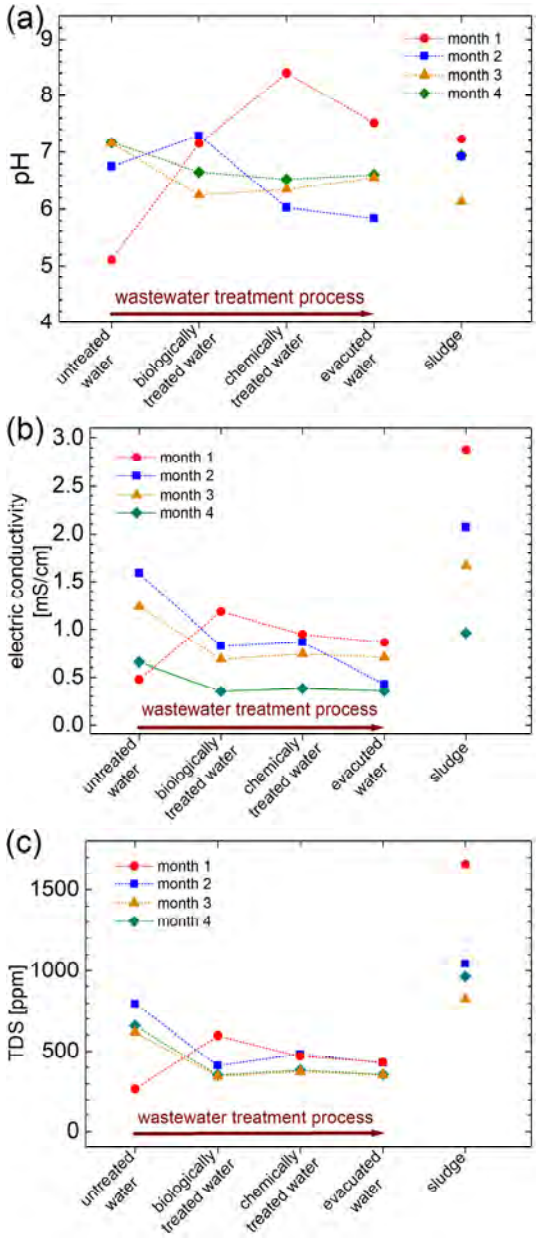

Fig. 6. The (a) ATR-FT-IR spectra of measured for the slaughterhouse wastewater (untreated water, biologically treated water, chemically treated water, evacuated water) and sludge in the (a) second; (b) third and (c) forth month of monitoring.

The average values of integrated areas A1, A2 and A3 over all three months are presented in Fig. 5d. Mainly the values of these integral areas calculated from absorbance spectra should reflect the concentration of pollutants but also the nature of pollutants may have a certain influence. All three parameters present a net decay from a higher value obtained for untreated water to biologically treated water and to chemically treated water. A slight increase of these areas can be observed for evacuated water. More increased values are obtained for sludge.

Selections of classic parameters were also measured and are graphically represented as follows: pH (Fig. 6a), electric conductivity (Fig. 6b) and TDS (Fig. 6c). With the exception of samples measured in the first months of monitoring for the reset of water samples one can observe an initial decay of pH, electric conductivity and TDS. Then, the values of these parameters, in the experimental error limit, will have similarly values. This is an indication of the fact that these parameters are not so sensitive.

CONCLUSIONS

The ^{1}H NMR T_2-distributions were used together with ATR-FT-IR spectra to evaluate the efficiency of the wastewater along the purification process (based on both biologically and chemically treatment) into a Transylvanian chicken slaughterhouse. We show that the advantage of using the T_2-distributions based analysis is the that one can discriminates between the water with dissolved solids from the water with undissolved solids and one can quantify the amount of pollutants in each reservoirs. By ^{1}H NMR relaxometry and IR spectroscopy it was shown that the quality of wastewater is significantly improved after chemical treatment. The measurement of classic parameters such as: pH, electric conductivity and TDS shown that they are not so sensitive, having similarly values for biologically and chemically treated water and for evacuated water, but in average indicating the water purification process.

REFERENCES

1. L. O. Paulista, P. H. Presumido, J. D. Peruço Theodoro, A. L. Novaes Pinheiro, *Environ. Sci. Poll. Res.*, 25, 19790–19800 (2018).
2. N. Boughou, I. Majdy, E. Cherkaoui, M. Khamar and A. Nounah, *ARPN J. Agric. Biol. Sci*., 13, 19-24 (2018).
3. R. I. Chelcea, D. Moldovan, D. E. Demco, E. Culea, R. Fechete, *Studia UBB Chemia*, 62(1), 73-88 (2017).
4. E. Jumate, D. Moldovan, D. L. Manea, D. E. Demco, R. Fechete, *App. Magn. Reson*., 47 (12), 1353-1373 (2016).
5. O. Cozar, N. Cioica, E. M. Nagy, C. Cota, R. Fechete, C. Filip, *Studia UBB Ephemerides*, 62 19-28 (2017).
6. R. S. Sipos, R. Fechete, D. Moldovan, I. Sus, Z. Pávai, D. E. Demco, *App. Magn. Reson.*, 47 (12), 1419-1437 (2016).
7. R. Fechete, D. E. Demco, X. Zhu, W. Tillmann, R. Vinokur, M. Möller, *Chem. Phys. Lett.*, 597, 6-15 (2014).
8. L. Venkataramanan, Y. Q. Song, M. D. Hürlimann, *IEEE Trans. Sign. Proc*., 50, 1017–1026 (2002).
9. Y. Q. Song, L. Venkataramanan, M. D. Hürlimann, M. Flaum, P. Frulla, C. Straley, *J. Magn. Reson*., 154, 261–268 (2002).
10. M. D. Hürlimann, M. Flaum, L. Venkataramanan, C. Flaum, R. Freedman, G. J. Hirasaki, *Magn. Reson. Imag.*, 21, 305–310 (2003).

STUDIA UBB PHYSICA, Vol. 63 (LXIII), 1-2, 2018, pp. 61-73
(RECOMMENDED CITATION)
doi:10.24193/subbphys.2018.06

A COMPARATIVE STUDY FOR NATURAL DEGRADATION OF THREE LOCAL ANESTHETIC DRUGS FOR HUMAN USE BY ^{1}H NMR RELAXOMETRY AND FT-IR SPECTROSCOPY

L. R. DRĂGAN[1], R. CRAINIC[1], R. FECHETE[1,2,*]

ABSTRACT. Three anesthetics, lidocaine (xylene), ropivacaine and propofol, with localized area of action while used in human surgery, were investigated by ^{1}H NMR relaxometry and ATR-FT-IR spectroscopy. The injectable liquid anesthetics were then subjected to degradation in natural condition during 36 days by exposure to direct sunlight radiation. The sunlight radiation intensity in the infrared and visible domain as well as UV index was monitored using Adafruit SI1145 breakout board sensor. The temperature and humidity was monitored using a digital DHT11 sensor. The evolution of ^{1}H NMR T_2-distributions, IR spectra, pH, refraction index, electric conductivity and total dissolved solids (TDS) show a degradation of studied anesthetics but also in some cases a certain recovery.

Keywords: *ATR-FT-IR spectroscopy, ^{1}H NMR relaxometry, T_2-distribution, lidocaine, ropivacaine, propofol.*

INTRODUCTION

Modern surgery cannot longer be performed without the use of local anesthetics which decrease the pain feeling into specific area and

[1] *Technical University of Cluj-Napoca, Faculty of Material and Environmental Engineering, B-dul Muncii 103-105, Cluj-Napoca, Romania.*
[2] *Babeş-Bolyai University, Faculty of Physics, 1 Kogălniceanu str., 400084 Cluj-Napoca, Romania*
[*] *Corresponding author: rfechete@phys.utcluj.ro*

relax the muscle power [1]. Therefore, the quality of local anesthetics is a very important factor which can be easily be lost, even in the guaranty period, by improper storage. Modern investigation methods like NMR spectroscopy, GC-FID, GC, GC-MS, HPLC and LC-MS are used for the study forced degradation of some liquid anesthetics in different stress condition such as acidic, basic, and oxidative environment or exposed to sunlight, UV light, elevated temperature and/or humidity [1, 2].

The aim of this study is to evaluate the degradation effect of direct exposal to sunlight radiation during a longer time period up to 36 days from 3 April 2018 to 9 May 2018 of three liquid anesthetics (lidocaine/xylene, ropivacaine and propofol) with local action while are used in human surgery. For that ^{1}H NMR T_2-distributions, ATR-FT-IR spectra, refraction index, pH, electric conductivity and TDS (total dissolved solids) were regularly measured. The natural degradation conditions: relative infrared and visible intensity, UV index, temperature and relative humidity were monitored using Adafruit specialized sensors connected to an Arduino Leonerdo ETH microcontroller and the data were recorded onto SD card.

EXPERIMENTAL

Three injectable liquid anesthetics with local action such as xylene 1 % (generally known as lidocaine), ropivacaine (10 mg/ml) and propofol (10 mg/ml) were used for the present study. The anesthetics were preserved in dark at room temperature in their original bottle package and extracted using a syringe with a needle for specific measurements of undegraded samples. For degradation in natural conditions the anesthetics were transferred in small volume, cylindrical plastic bottles and exposed at the laboratory window to the direct action of sunlight. Near to the closed bottles two digital sensors: i) Adafruit SI1145 breakout board sensor and ii) DHT11 sensor were placed to monitor the infrared and visible uncalibrated intensity calibrated UV index, temperature and humidity conditions. The data were stored on the onboard microcontroller SD card and recorded if the UV index was larger than 0.6.

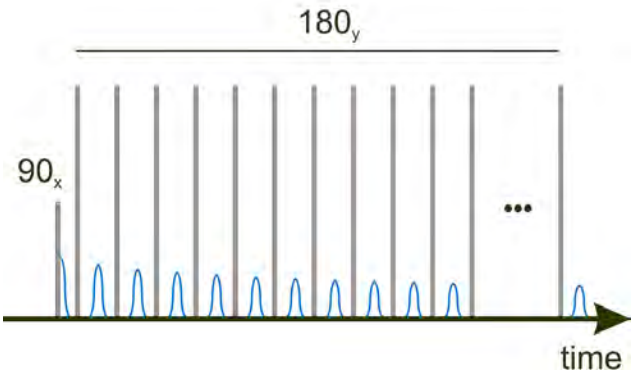

Fig. 1. The CPMG pulse sequence used for the ^{1}H NMR data acquisition.

The low field Bruker Minispec MQ 20 spectrometer working at 19.69 MHz frequency was used for the ^{1}H NMR relaxometry measurement [3-5]. The echo time in the CPMG (Carr-Purcell-Meiboom-Gill) pulse sequence (see Fig. 1) was 5 ms. To cover the full decay of liquid samples a number of 3000 echoes was recorded. The recycle delay (RD) was set at 3 s and a number of 32 scans were accumulated. A Laplace-like inversion algorithm described by [6-8]:

$$M(\tau) = \int_0^\infty f(T_2) e^{-\frac{\tau}{T_2}} dT_2 , \quad (1)$$

was used for data processing and normalized transverse relaxation time T_2-distibutions, $f(T_2)$ were obtained [9, 10].

A Jasco 6200 FT-IR spectrometer was used for the measurements of the FT-IR spectra. The ATR (attenuated total reflection) accessory was used for our liquid samples. For background we use distilled water and we perform the specific ATR correction after each data measurement. The spectrometer set-up was as follow: i) the measurement domain was between 349.053 cm^{-1} up to 4000.6 cm^{-1}; ii) due to the noisy data at low wavenumber values the IR spectra were cutoff at 700 cm^{-1}; iii) a number of 128 scans were accumulated; iv) the resolution was set at 4 cm^{-1}.

The refraction index was measured using a Hanna instrument. This device originally give the refraction index in Brix units. After calibration, finally the refraction index was calculated using:

$$n = 1.13913 + 0.19366 \cdot e^{\frac{Brix}{134.2178}}. \quad (2)$$

For the measurement of pH and electric conductivity we used a IP67 Combo multi-parameter. The TDS (totally dissolved solids) was measured with a pocket TDS&EC instrument with temperature correction.

RESULTS AND DISCUSSION

In Fig. 2a the normalized ^{1}H CPMG decay curves measured for the undegraded anesthetics are compared. At a visual inspection, for the full 15 s decay, small differences can be observed between anesthetics. One can see that the CPMG curve for propofol initially decays faster than the curves measured for xylene and ropivacaine suggesting the existence of a rigid component, then the decay become slower suggesting the existence of a more mobile component. The differences between CPMG decays of xylene and ropivacaine are small even in the initial time regime (see the insert in Fig. 2a).

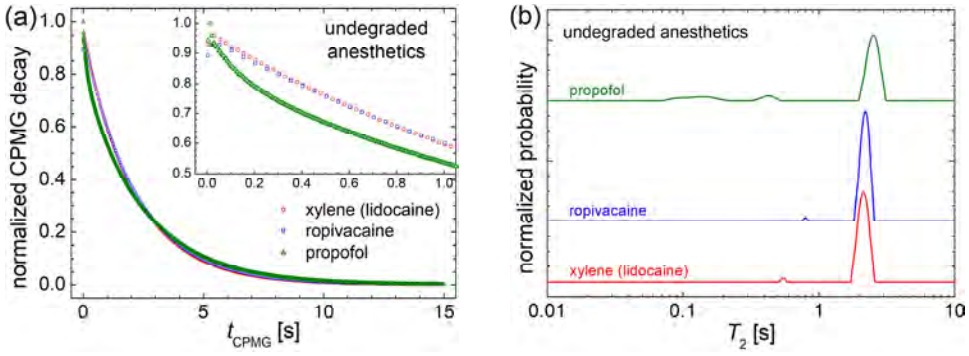

Fig. 2. (a) ^{1}H NMR CPMG decays and (b) the corresponding T_2-distributions measured for undegraded anesthetics: xylene (red), ropivacaine (blue) and propofol (olive).

A better interpretation in terms of components (protons - ^{1}H reservoirs) with different mobility can be performed by considering the transverse relaxation time (T_2) distributions which are presented in Fig. 2b. The T_2-distributions of xylene (lidocaine) and ropivacaine are similar presenting two peaks: i) a large peak located at most probable T_2 (maximum of peak) 2.1 s and 2.2 s respectively, which compared to a 2.4 s value measured for distilled water (see ref. [9]) suggests a small amount of dissolved solid and ii) a small peak suggesting a small quantity of undissolved solids. The T_2-distributions measured for propofol is different. There it is present one large peak centered at ~ 2.5 s belonging to water and three components with a reduced mobility where two of them (the doublet located at ~ 10 ms) being partially overlapped. These components are most probable responsible with the milky aspect of propofol anesthetic.

Large differences can be observed also in the ATR-FT-IR spectra of our studied liquid anesthetics (see Fig. 3) between propofol spectrum, characterized by well defines absorption lines and xylene and ropivacaine spectra characterized by broad bands. Generally, all spectra can be divided into three regions:

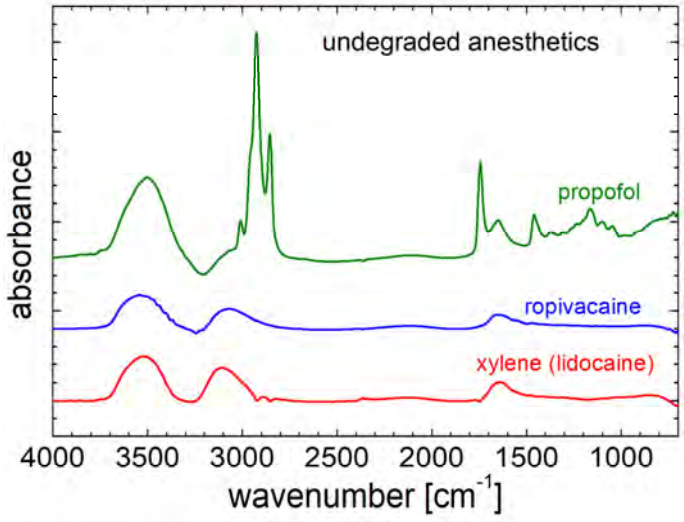

Fig. 3. The ATR-FT-IR spectra of undegraded propofol, ropivacaine and xylene(lidocaine).

i) the first one from low wavenumber (here 700 cm^{-1}) up to ~ 1900 cm^{-1} present only broad bands for xylene and ropivacaine but for propofol four elevated peaks at ~ 1163, 1462, 1649 and 1747 cm^{-1} can be observed; ii) the middle region between 2690 cm^{-1} up to 3260 cm^{-1} is characterized by broaden absorption peaks for xylene and ropivacaine but again three relatively well resolved peaks belonging to propofol located at ~2857, 2926 and 3012 cm^{-1} are present and iii) the region located between 3260 cm^{-1} and 3780 cm^{-1} which is characterized by broaden peaks for all three samples of liquid anesthetic.

Into an attempt of a specific characterization of the studied anesthetics, a molecular mechanics simulation was performed using Gaussian 09 software. The structure of lidocaine molecule was constructed (see Fig. 4 – top right) and optimized using default settings parameters (Hartree-Fock/ground state method with 3-21G basis set). The vibrational frequencies were also calculated (see Fig. 4 – top left) and the IR spectrum was simulated (Fig. 4 bottom).

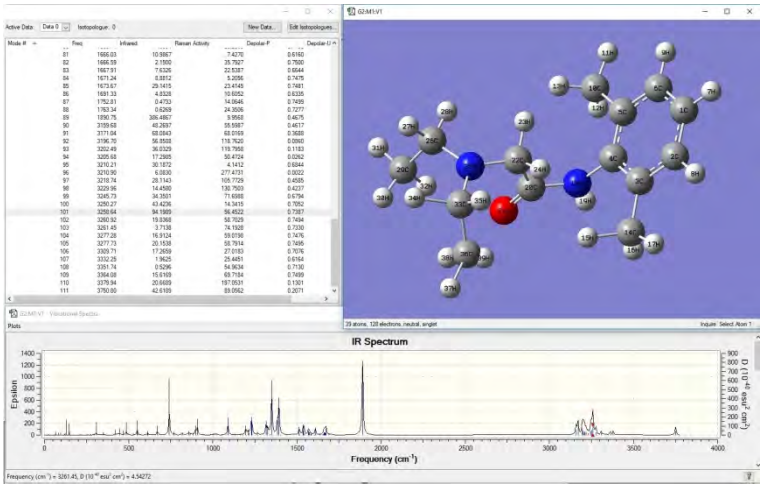

Fig. 4. Gaussian 09 simulation of lidocaine (xylene) structure and IR spectrum

The simulated spectra differ from the measured spectrum of lidocaine in to many essential points, then we consider that our broad spectra of small amount of anesthetics in water can be interpreted by numeric simulations

only after a large investigating time which is beyond our present purpose. Therefore, the physico-chemical properties characterization effort of anesthetics was oriented into another direction.

The refraction index, pH, electric conductivity and TDS (total dissolved solids) were measured for our anesthetics and the results are presented in Fig. 5. The larges refraction index was measured for propofol (which present also a milky-like visual aspect) while the refraction index for colorless xylene and ropivacaine (see Fig. 5a) is closed to the distilled water (1.33). Slightly acid character was observed from the pH of our three anesthetics. While xylene 1 % presents an almost neutral character (pH ≅ 6.29) the ropivacaine is the most acid anesthetic (pH ≅ 5.22). Nevertheless, all of these values are into desired limits.

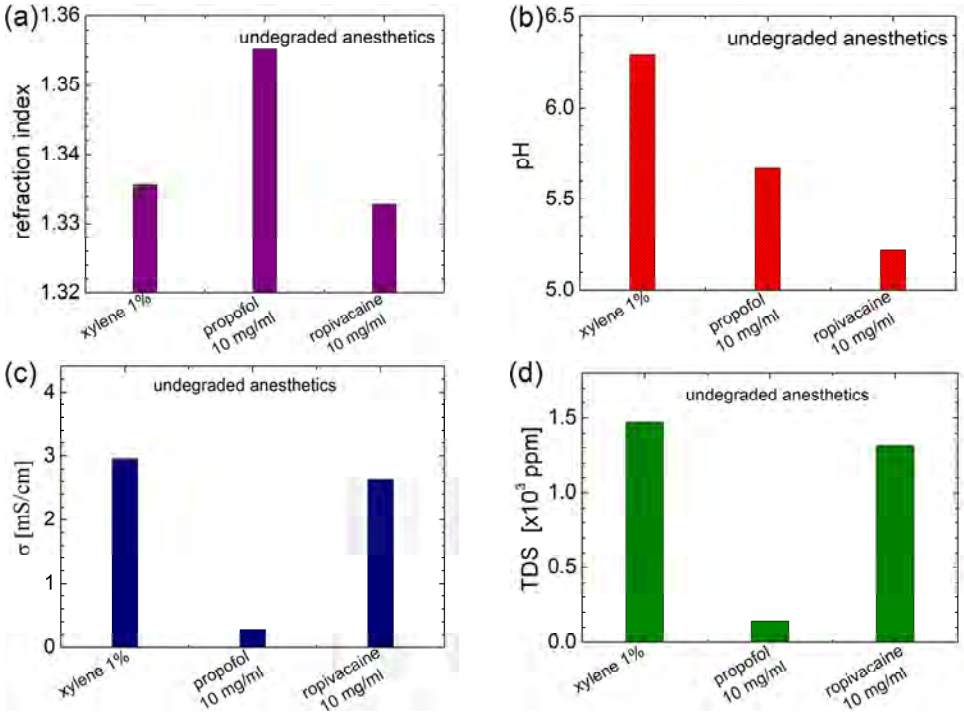

Fig. 5. (a) Refraction index; (b) pH; (c) electric conductivity and (d) total dissolved particles measured for undegraded xylene, propofol and ropivacaine.

Elevated values are measured for electric conductivity (Fig. 5c) and TDS (Fig. 5d) parameters of xylene and ropivacaine. These are between 2600 and 3000 µS/cm for electric conductivity (EC) and between 1300 and 1500 ppm

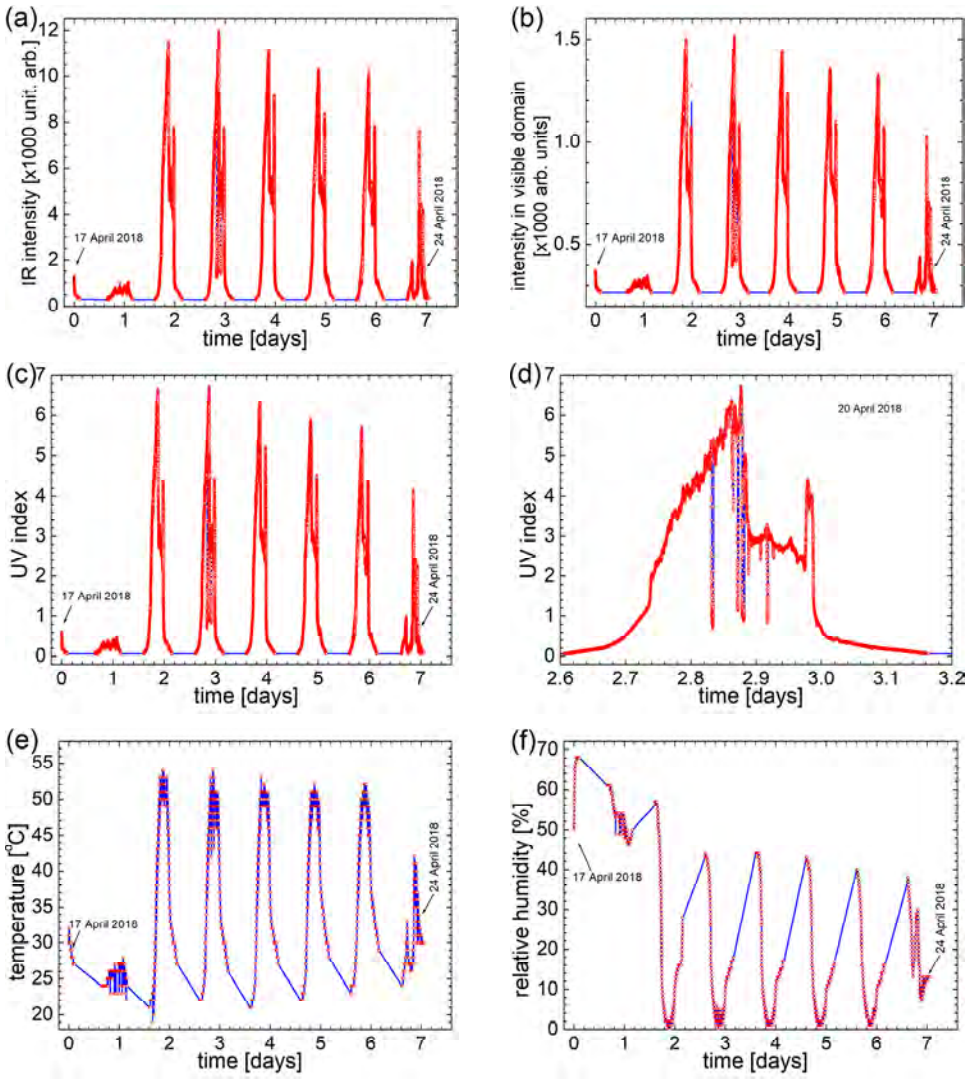

Fig. 6. Infrared**,** visible, ultraviolet radiation characteristics, temperature and relative humidity of environmental measured for the natural degradation of anesthetics.

for TDS suggesting the existence of a large number of dissolved solids with electric properties (ions) in anesthetic injectable solution. Much lower values were obtained for propofol: 284 μS/cm for EC and 142 ppm for TDS.

For the study of natural degradation under natural conditions the liquid anesthetics were exposed to the direct sunlight for a period of 36 days in the spring-summer of 2018. Some environmental parameters were measured and presented in Fig. 6 for a period of one week in the middle of monitored period from 17 to 24 April 2018. These parameters are the uncalibrated infrared intensity (Fig. 6a) and light intensity (Fig. 6b), and the calibrated UV index (Fig. 6c), temperature (Fig. 6e) and relative humidity (Fig. 6f). The data were collected from 3 to 3 minutes if the UV index was larger than 0.6. In Fig. 6d the UV index data were represented for a period of approximately one day (20 April 2018). Fine features of UV index variation can be observed during this monitored period. In fact all parameters such as the sun radiation (in IR, visible and UV) as well as the measured temperature and humidity are largely sensitive to the clouding conditions. For example, in 18 April (day 1 as it is presented here) it was mostly clouded reflected into small values of monitored parameters. One can remark also that the relative humidity of air surrounding the anesthetic samples is inversely proportional with the rest of measured parameters.

For the characterization of the degradation effect due to the direct exposure at sunlight of our three anesthetics the samples were periodical measured. In Fig. 7 the T_2-distributions measured for the xylene, propofol and ropivacaine degraded for 14 (Fig. 7a) and 36 (Fig. 7b) days in natural conditions are presented. While the T_2-distributions measured at 14 days of degradation under direct light exposure are similarly for all samples compared with the corresponding distributions measured for undegraded samples, at 36 day of exposure the degradation effect is visible from the changed in peaks positions, number, and width. From the T_2-distributions of xylene the small peak disappeared indicating a dissolution process of solids (see the red curve in Fig. 7b). In the T_2-distributions of ropivacaine two peaks appears indicating a dissociation process of undissolved solids into two components with different mobility (hence probably with different size). The doublet located at ~ 10 ms

in the T_2-distributions of propofol merges into a single peak indicating (also from the displacement of main peak to smaller T_2 values) the dissolution process of less mobile components.

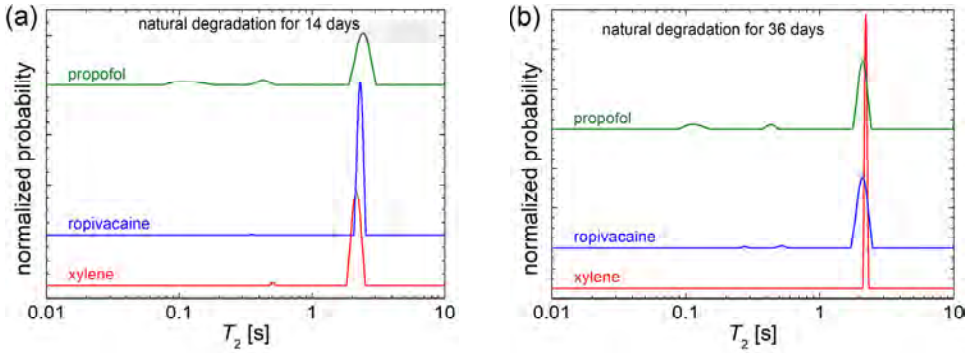

Fig. 7. The T_2-distributions measured for xylene (lidocaine), ropivacaine and propofol subjected to natural degradation for (a) 14 and (b) 36 days.

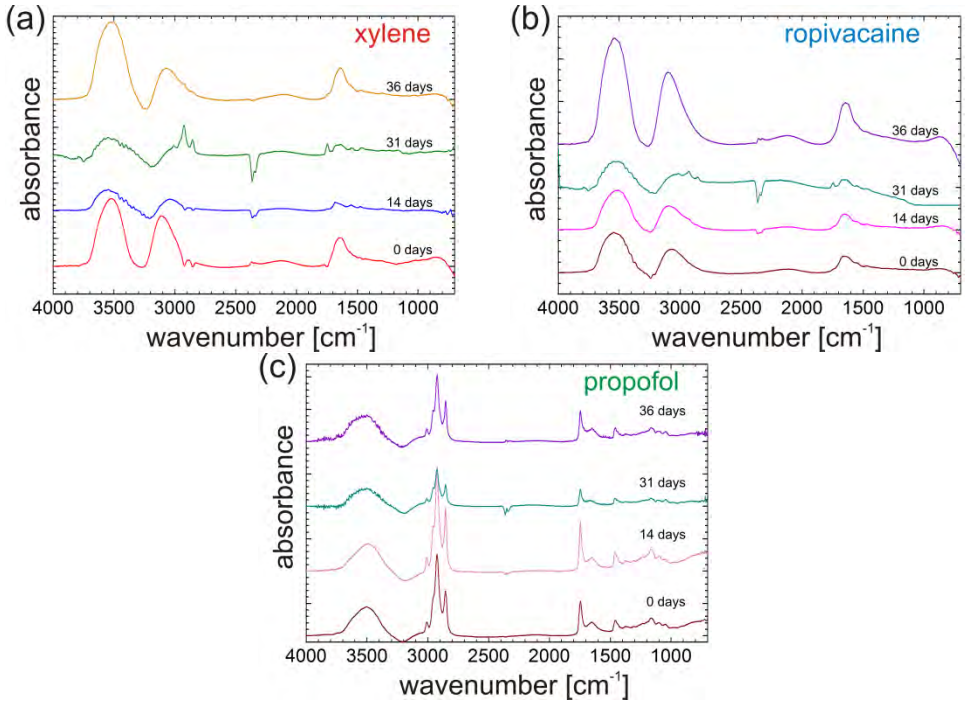

Fig. 8. ATR-FT-IR spectra measured for (a) xylene; (b) ropivacaine and (c) propofol undegraded and degraded under natural conditions for 14, 31 and 36 days.

The ATR-FT-IR spectra of degraded anesthetics subjected to direct sunlight are comparatively presented in Fig. 8a for xylene, Fig. 8b for ropivacaine and Fig. 8c for propofol. The samples were measured at 14, 31 and 36 days of natural degradation. As a general remark is the fact that in all cases a degradation effect can be observed from the decay of the overall intensity, in the three spectral regions discussed before, but also a recovery process can be remarked for samples measured in day 36 of degradation in natural conditions. Such recovery process is supported by our other measurements.

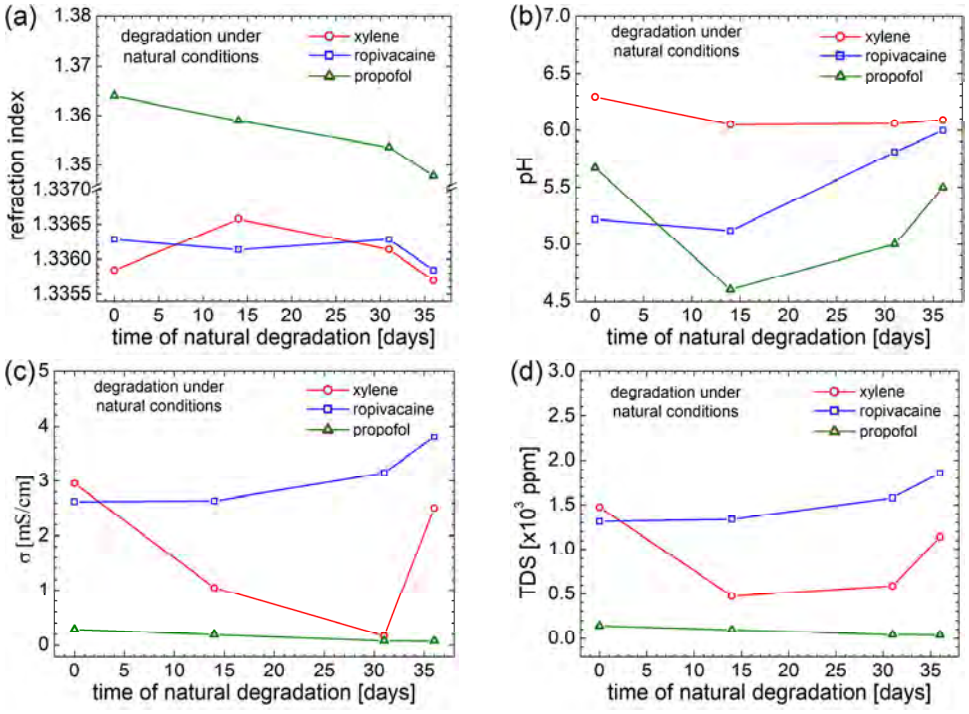

Fig. 9. The dependence of (a) refraction index; (b) pH; (c) electric conductivity and (d) TDS function of natural degradation time for human use anesthetics (xylene, ropivacaine and propofol).

In Fig. 9 the refraction index, pH, electric conductivity (EC) and TDS are presented for degraded anesthetics in natural conditions. The continue degradation of propofol (olive triangle) exposed to direct sunlight is observed from the monotone decay of refraction index, EC and TDS. Only the pH of propofol presents a certain recovery after day 14 up to day 36.

The degradation of ropivacaine (blue square) is observed as a monotone increase of pH, EC and TDS parameters. In the case of ropivacaine the refraction index presents a slight recovery. For xylene (red circles) the initial degradation and recovery is most evident for all four measured parameters but especially for electric conductivity (Fig. 9c).

CONCLUSIONS

The degradation process in natural conditions, by direct exposure to sunlight into a plastic package of three liquid anesthetics, with local action while used in human surgery, was monitored by specific changes of advanced Laplace ^{1}H NMR T_2-distributions, Fourier ATR-FT-IR spectra, but also by global refraction index, pH, electric conductivity and total dissolved solids. Some parameters present changes at a short exposure duration but all measured parameters present significant changes after 36 of exposure to direct sunlight of local xylene, ropivacaine and propofol anesthetics.

REFERENCES

1. K. M. Patel and A. D. Patel, *Int. J. Curr. Res.*, 9(6) 53036-53043 (2017).
2. Y. Kadioglu, A. Atila, M. S. Gultekin, N. A. Alp, *Iranian J. Pharma. Res.*, 12(4) 659-669 (2013).
3. O. Cozar, N. Cioica, E. M. Nagy, C. Cota, R. Fechete, C. Filip, *Studia UBB Ephemerides*, 62 19-28 (2017).

4. R. I. Chelcea, D. Moldovan, D. E. Demco, E. Culea, R. Fechete, *Studia UBB Chemia*, 62(1), 73-88 (2017).
5. R. Fechete, D. E. Demco, X. Zhu, W. Tillmann, R. Vinokur, M. Möller, *Chem. Phys. Lett.*, 597, 6-15 (2014).
6. L. Venkataramanan, Y. Q. Song, M. D. Hürlimann, *IEEE Trans. Sign. Proc*., 50, 1017–1026 (2002).
7. Y. Q. Song, L. Venkataramanan, M. D. Hürlimann, M. Flaum, P. Frulla, C. Straley, *J. Magn. Reson*., 154, 261–268 (2002).
8. M. D. Hürlimann, M. Flaum, L. Venkataramanan, C. Flaum, R. Freedman, G. J. Hirasaki, *Magn. Reson. Imag.*, 21, 305–310 (2003).
9. E. Jumate, D. Moldovan, D. L. Manea, D. E. Demco, R. Fechete, *App. Magn. Reson*., 47 (12), 1353-1373 (2016).
10. R. S. Sipos, R. Fechete, D. Moldovan, I. Sus, Z. Pávai, D. E. Demco, *App. Magn. Reson.*, 47 (12), 1419-1437 (2016).

STUDIA UBB PHYSICA, Vol. 63 (LXIII), 1-2, 2018, pp. 75-88
(RECOMMENDED CITATION)
doi:10.24193/subbphys.2018.07

OPTIMIZATION OF TITANIUM NITRIDE FILM SYNTHESIS: CORRELATIONS BETWEEN THE STRUCTURE / MICRO-HARDNESS AND DEPOSITION CONDITIONS

MARIANA POP[1,*], G. NEGREA[1], A. POP[2]

ABSTRACT. The DC sputtering method based on the variation of the potential of target function of nitrogen flow rate, for the deposition of titanium nitride (TiN) films, with the elementary chemical composition close to the stoichiometric one is presented. The process control method used in these experiments is the identification of the nitrogen flow required for the deposition of stoichiometric TiN layers by using the target potential as the reference parameter. The effects of the nitrogen flow, polarization voltage and discharge current on the structure, microstructure and micro-hardness of TiN films was studied.

Keywords: *TiN films, DC sputtering, XRD,hardness.*

INTRODUCTION

TiN is considered nowadays as one of the most technologically important materials. A wide variety of fabrication techniques have been used for the growth of B1-TiN films, such as Magnetron Sputtering (MS) [1–7].

[1] *Technical University, Faculty of Materials and Environmental Engineering, Bvd.Muncii 103-105, Cluj-Napoca*
[2] *Babeş-Bolyai University, Faculty of Physics, 1 Kogălniceanu str., 400084 Cluj-Napoca, Romania*
[*] *Corresponding author: mariana.pop@ipm.utcluj.ro*

The development of film microstructure in various growth conditions is commonly represented by structure zone models (SZM) [8], which tend to relate the effects of the process parameters on the resulting microstructure of polycrystalline thin film materials. These diagrams are compiled as a function of the homologous temperature, $T_h = T_s/T_M$, where Ts is the substrate temperature and T_M is the melting point of the deposited material (T_M = 3222 K for TiN). For the case of sputter-deposition, it also necessary to take into account the working pressure [9], and more generally the energy deposited per incident particle [10]. Typical deposition conditions to obtain stoichiometric TiN films with a relatively dense microstructure require sufficient adatom mobility. TiN films have high electrical conductivity, adhesion, hardness and chemical inertness therefore they are used as decorative, wear-resistant and corrosion-resistant coatings, for modifying the metal surface against fretting corrosion. Also they are applied in silicon technology as diffusion barriers for aluminum and copper metallization, when creating MOS transistors, ohmic and rectifying contacts. TiN films, exhibit excellent physical and chemical properties combining metal-like and covalent characteristics,such as high electrical conductivity, adhesion, hardness and chemical inertness therefore they are used as decorative, wear-resistant and corrosion-resistant coatings, for modifying the metal surface against fretting corrosion. [11–13].

Some studies have been conducted to investigate the effect of physical parameters on TiN morphology and microstructure as well as electrical properties. Pononetal et.al. [14] found that with increasing nitrogen content, surface roughness,relative intensity of(111)to(200) and film resistivity decrease. Yehetal et al. reported that when sputtering pressure decreases, preferred orientation of TiN films transforms from (111) to (200), and film resistivity decreases while film density increases [15]. The reactive deposition process is considered complex and difficult to control [16, 17], showing maximum instability in the partial nitrogen pressure required to form the stoichiometric layers of nitrides. For the deposition of nitride layers, most of the deposition systems use the partial nitrogen pressure as a control parameter, being maintained within the limits set by the nitrogen flow [16, 18].

Sundgren et al. [19] have shown that at low temperatures due to the low mobility of condensed atoms on the surface of the substrate, the partial pressure range in which stoichiometric layers can be obtained is very narrow and therefore difficult to control. Kuruppu et al. [3] have shown that under conditions of a constant current discharge, the cathode's potential changes depending on the partial pressure of the nitrogen and that it can be used to determine the nitrogen flow required for the deposition of stoichiometric layers. This control method is experimented for depositing layers in the Ti-Si-N system using two magnetrons.

In this work, a simple method of controlling the process of deposition of TiN layers by low temperature reactive DC magnetron sputtering was achieved. The method, based on the variation of the potential of the target according to the nitrogen flow rate, is simple and allows for the quick setting of the conditions required for the deposition of titanium nitride layers with the elementary chemical composition close to the stoichiometric one. The influence of some parameters of the deposition process (nitrogen flow, polarization voltage, discharge current) on the microstructure and layer microstructure on the TiN films was studied.

EXPERIMENTAL

The DC magnetron sputtering system was installed in confocal geometry with two debit-meters; one with neutral Ar gas and other with nitrogen (N_2) reactive gas. The magnetrons was inclined with 24 degrees between their symmetry axes. The Si (001) single crystalline substrate with the size of 25x15x0.54 mm is heated (reaching a maximum temperature of 700 ° C) and a thermo-regulator controls the substrate temperature. The substrate was ultrasonically cleaned in trichlorethylene, acetone and then methanol. A titanium target of 99.95% purity was used. The deposition was carried out at a pressure of 0.66 Pa (5 mTorr) under Ar + N_2 atmosphere at a 6 Amper discharge current. The substrate temperature of was measured by using a chromium-aluminum thermocouple in direct contact with it. As the

films were not heated further, their temperature did not exceed 200^0 C at the end of the deposition. The installation also contains a flat electromagnetic probe of Langmuir type, mounted on a support behind the substrate and having the same dimensions as the substrate. An auxiliary coil is located behind the substrate support. The role of the Langmuir sample is to characterize the plasma in the substrate area, and the role of the coil is to modify the magnetic field distribution and, implicitly, the trajectory of charged particles (ion and electron flow) into the film deposition area on the substrate. The structural analysis of deposited layers was done by the X-ray diffraction (XRD) in the Bragg-Brentano configuration. The radiation used was Cu $K_{\alpha 1}$, the acceleration voltage of 40 kV and the current of 30 mA. The tests were carried out with a step of 0.02^o in 2θ and a counting time of 2 sec / step. The micro-hardness measurements were made with 0.1 N load, on layers with thicknesses in the range of 3.9-4.2 μm, deposited on Si substrate. Determinations were made using the Vickers method. Because weights of less than 1.96 Newton were used, the notion of micro-hardness was used.

RESULTS AND DISCUSSIONS

A. Controlling and adjusting the deposition process

The classical method for controlling cathodic sputter deposition processes is based on the measurement and adjustment of the partial pressure of reactive gas (nitrogen or oxygen), depending on the nature of the deposition layer. Reactive cathodic sputtering deposition leads to complex phenomena on the surface of the target. As the reactive gas flow increases, the target surface is covered with a compound layer, which has other characteristics compared to the target material. The sputtering yield decreases, implicitly decreasing the deposition rate and prolonging the time required to achieve a layer of a certain thickness. Figure 1 shows the dependence of the target potential (V_T) function of the nitrogen flow (Φ_{N2}) recorded for a discharge current I_d = 6 A at a partial argon pressure p_{Ar} = 0,66

Pa (5 mTorr) and a voltage polarization of the substrate Vs =- 20 V. It is noted that this curve has a maximum (V_{Tmax}), which, for the specified conditions, has a value of ≈550 V and corresponds to a nitrogen flow $\Phi_{N2} \approx 6,4$ cm^3 / min. The tests performed showed that this peak is associated with nitrogen flow around which Ti layers with stoichiometry close to the theoretical (atomic ratio N / Ti = 1) can be deposited.

The optimal deposition regime is close to the point where the partial pressure of the active gas tends to rise rapidly (point B in figure 1).

The process control method used in these experiments is based on the rapid identification of the nitrogen flow required for the deposition of stoichiometric TiN layers by using the target potential as the reference parameter.

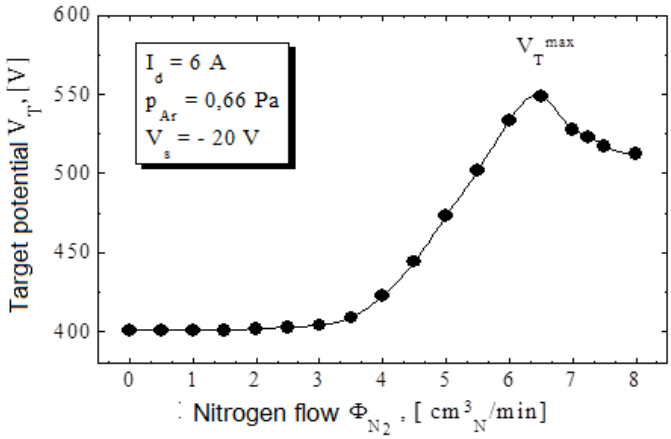

Figure 1. Variation of target potential according to nitrogen flow in constant current discharge mode.

By correlating the data regarding the variation of the potential of the target with those related to the variation of the partial pressure of nitrogen according to the nitrogen flow, the following conclusions can be drawn:

- For nitrogen flow rates less than ≈ 4 cm^3 / min, the cathodic sputtering is done in a metallic regime, for nitrogen flow rates higher than ≈ 7.5 cm^3 / min, the sputtering is in the compound mode and for flows in the range 4-7 cm^3 / min there is a transient regime.

- The transition from preferential metal deposition (RM) to predominantly compound (RC) deposition takes place within the critical range (IC) $\Phi_{N\,2} \approx$ 6-7 cm^3 / min and is characterized by a more pronounced increase in pressure partial nitrogen.

Within this range, the nitrogen flow required to deposit layers with composition as close to stoichiometric as possible, but without passing through (RC) should be determined.

- Increase of partial nitrogen pressure in (IC) is $\Delta p_{N2\,cd}$ = 0,26 mTorr (0,035 Pa), a very narrow pressure range, which, in order to be used as process parameter, requires special measuring means.

- The target potential variation in the (IC) is $\Delta V_T \approx$ 17 V, a variation easily measurable with ordinary devices. In addition, unlike the partial pressure p_{N2cd}, which increases continuously in (IC), the potential of the target exhibits a peak (V_{Tmax}), which makes the area (IC) very fast and accurate.

- This process control method, based on monitoring the variation of the potential of the target according to the nitrogen flow (with an X-Y coordinate recorder under the experimental conditions imposed here), is particularly simple and proved to be effective.

In order to study the microstructure of layers obtained using the $V_T = f(\Phi_{N\,/\,2})$ curve as the process regulating tool, two series of depositions were made at two different polarization stresses at the characteristic points of this curve, marked with A, B, C and A_1, B_1, C_1 according to figure 1.

Layers deposited at lower nitrogen flow rates (e.g., 3.4 cm^3/ min) did not show the gold color specific for TiN nitrides but were white to yellow in color, indicating a high nitrogen deficiency.

Using nitrogen flows with values ranging from 5-8 cm^3 / min, we obtained films where the Ti / Ni ratio tends to the unit.

Deposition conditions were: discharge current I_d = 6 A and argon pressure p_{Ar} = 0,66 Pa (5 mTorr). Table 1 lists the other deposition conditions as V_T of target potential and the values of the Vs substrate potential. Knowing the deposition time and the thickness *h* of the deposited layers we determined the deposition rate.

Table 1. Nitrogen flow Φ_{N2}, V_T of target potential, Vs of substrate polarization voltage, deposition time t, layer thickness h, and v_d deposition rate for sample series A, B, C and A1, B1, C1, deposited in the appropriate points marked in figure 1.

Sample	Φ_{N2} cm^3/min	V_T Volt	V_s Volt	t min	h μm	v_d μm/h
A	5,0	472	-25	10	1,68	10,08
B	6,2	540	-25	10	1,65	9,90
C	8,0	507	-25	10	0,95	5,70
A_1	5,0	470	-350	10	1,35	8,10
B_1	6,2	540	-350	10	1,30	7,80
C_1	8,0	500	-350	15	1,00	4,00

Figure 2 shows the dependence of film deposition rate function of nitrogen flow rate, for the two series of samples. It is noted that the deposition rate decreases quite rapidly with the increase of the nitrogen flow above the maximum value of the $V_T = f(\Phi_{N2})$ curve, indicating the coverage of the target surface with a layer of TiN and the change of the sputtering rate.

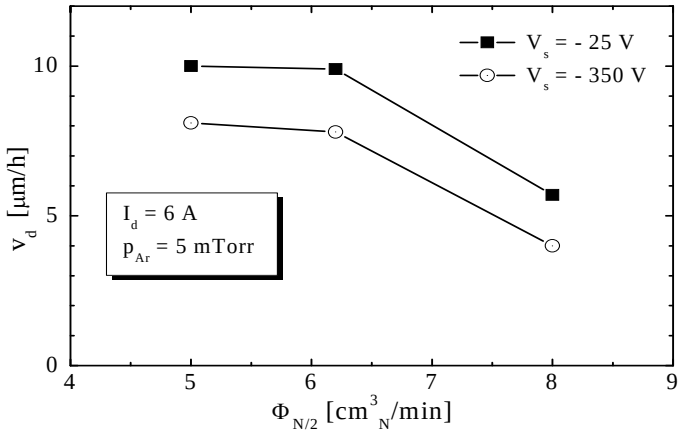

Figure 2. Dependence of the deposition rate v_d vs. the nitrogen flow Φ_{N2}, for two polarization voltage of the substrate: -25 and - 350 V.

Film deposition of sample B was made at a nitrogen flow slightly lower than that corresponding to the peak curve $V_T = f(\Phi_{N\,2})$ in order to avoid passing the discharge in compound mode.

Irrespective of the nitrogen flow rate used, the deposition rate is reduced by approximately 20% by increasing the polarization voltage of the sample from -25 V to -350 V. More probably the decrease of the deposition rate is due to the re-sputtering of N and Ti atoms deposited as a result of higher energy of ion bombardment and densification of the deposited layer. The deposition rate is reduced by approximately 20% by increasing the polarization voltage of the sample from -25 V to -350 V.

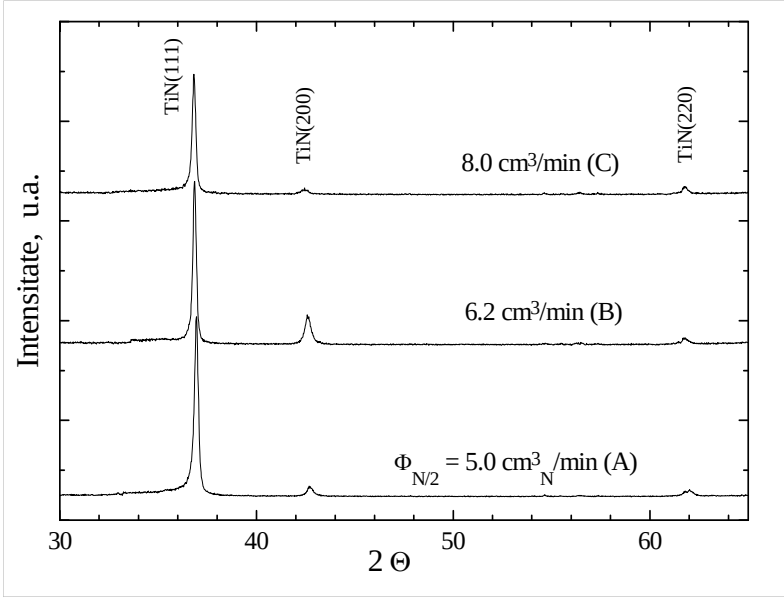

Figure 3. The XRD spectrum of samples A, B and C (see Table 1).

Figure 3 shows the X-ray diffraction measurements spectra for the samples A, B, C deposited at a polarization voltage of -25 V. It is noted that the increase in the nitrogen flow rate from 5.0 to 8.0 cm^3/min does not affect the phase composition of the deposited layers. The relative ratio of line intensities in the diffraction spectra indicates a pronounced preferential

crystallographic orientation (111) compared to the standard spectrum of TiN powder. The tendency for preferential orientation of TiN grains is slightly lower for the layer deposited at the maximum point of the curve $V_T = f(\check{N}_{N/2})$, (sample B). The TiN films deposited under relatively low intensity bombardment conditions have surface chemistry processes that favour the formation of [111] preferential orientation [20]. Therefore, based on the analysis of X-ray patterns it can be concluded that the nitrogen flowrate has stronger impact on the film properties when the current density is higher [21].

XRD show that all 6 samples, deposited at nitrogen flows around the maximum point of the $V_T = f(\Phi_{N/2})$ curve, show only the peaks of the TiN compound.

A significant difference was found between the XRD spectra of the A_1, B_1, and C_1 series samples compared to those of the A, B, C series samples. Figure 4 shows the XRD spectra for the samples B and B_1 deposited at a polarization voltage of -25 V and -350 V, and obtained at peak curve points $V_T = f((\Phi_{N2})$, respectively.

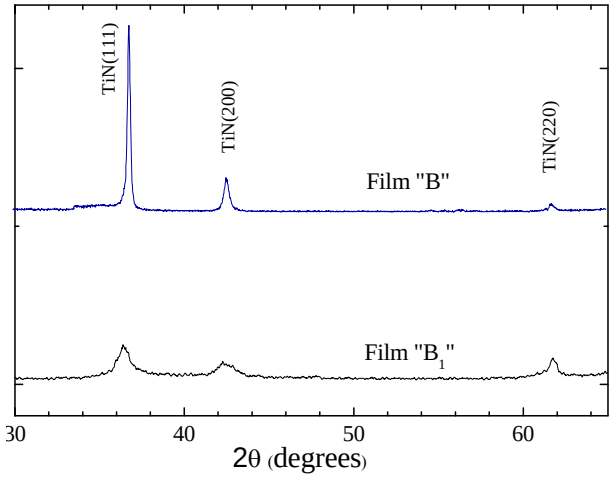

Figure 4. XRD for samples B and B1 (see Table 6.1).

The diffraction peaks of sample B_1 shows a low intensity and a wide line width at half intensity. The decreasing of the intensity peaks and widening them by increasing the polarization voltage of the sample from -

25 V to -350 V suggest the increase of the defects density of the TiN layer, the reducing of the average grain size and the increase of the remaining tensions in the film.

The examination of the color of the layers deposited at different nitrogen flows in the range 3.4 - 8.0 cm^3 / min showed that the films deposited at:

- nitrogen flows lower than the maximum flow rate $V_T = f(\Phi_{N2})$ have lighter colors indicating sub-stoichiometric compositions (N /Ti < 1.0);

- the maximum point of the curve $V_T = f(\Phi_{N/2})$, respectively B and B_1 have a titanium nitride-specific golden color;

- nitrogen flows higher than the flow corresponding to the maximum curve VT = f (ΦN / 2) are darker to brown, indicating over-stoichiometric compositions (N /Ti > 1.0).

Figure 5 shows the dependence of micro-hardness function of the nitrogen flow of the TiN films. The maximum value of the micro-hardness obtained was 1930 HV0,01, somewhat lower than the reference value of TiN hardness in the literature (2200 HV). This difference could be due to the presence of micro-pores in the layer structure.

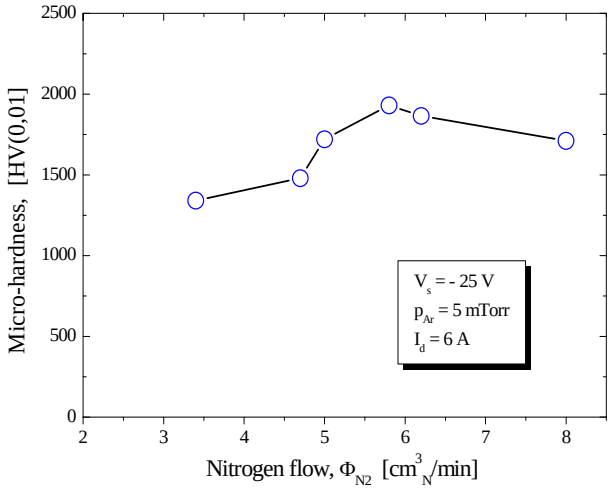

Figure 5. Variation of micro-hardness of TiN layers according to nitrogen flow.

The micro-hardness increases rapidly from 1520 to 1870 HV0,01 with the increase of the polarization voltage from Vs = - 25 V to -150 V. For Vs = -350 V, a micro-hardness of 1950 HV0,01 is obtained. These results show that the micro-hardness of the TiN layers increases with increasing the polarization stress of the substrate, but for the deposition of higher hardness layers, it is not necessary for the deposition system to be modified to allow not only the increase in the ion flux density of their energy.

B. Checking the control / process control solution

In order to check the viability of the method applied for controlling / adjusting the process, in figure 6, the characteristic curves $V_T = f(\Phi_{N/2})$ for the three discharge currents are recorded for: 2 A, 4 A and 6A. It can be seen that even in the case of lower discharge currents, the $V_T = f(\Phi_{N/2})$ curves have well-defined maxima which can be used for rapid determination of the nitrogen flow over which the cathodic sputtering lead to stoichiometric TiN films.

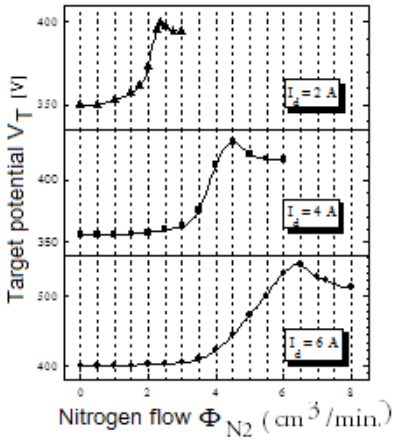

Figure 6. Characteristic curves $V_T = f(\Phi_{N/2})$ for three different values of the discharge current I_d=2; 4 and 6 A (p_{Ar} = 0,66 Pa).

For the lower discharge current (2 A), a film was deposited on the silicon substrate under the following conditions: p_{Ar} = 0.66 Pa; $\Phi_{N/2}$ = 2.2 cm3 N / min;

($V_T = V_{Tmax}$ for $\Phi_{N/2} = 2.3$ cm^3 / min); V_T = -393 V; Vs = - 25 V; time deposition 10 min. The thickness of the layer was determined to be 0.48 μm, resulting in a deposition rate of approx. 2.9 μm / hr. The color of the deposited layer was identical to that deposited on sample B indicating very close N/Ti atomic ratios. Figure 7 shows the XRD peaks of film obtained by using a current of 2A. It is noted that only the TiN diffraction lines appear in the XRD spectrum, and that ratio of the intensity of the diffraction lines (111) / (200) / (220) is similar to sample B.

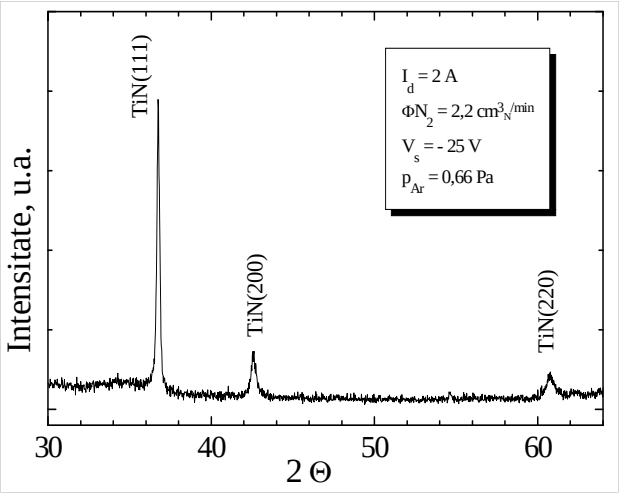

Figure 7. XRD of TiN film deposited at a discharge current I_d = 2 A.

The obtained results confirm the viability of the method used to regulate the deposition process of the TiN layers in the constant discharge mode.

CONCLUSIONS

DC sputtering method, based on the variation of the potential of the target according to the nitrogen flow rate, is simple and allows for the quick setting of the conditions required for the deposition of titanium nitride films with the elementary chemical composition close to the stoichiometric one.

The parameters of the deposition process (nitrogen flow, polarization voltage, discharge current) influenced microstructure and the micro-hardness of the TiN films. The correlations between the structure / micro- hardness and deposition conditions was evidenced.

The maximum hardness of the TiN layers obtained was slightly lower than that reported by other authors. A likely explanation hardness values TiN films obtained is the low deposition temperature, is the formation of columnar structures with a low compaction degree.

REFERENCES

1. L. Hultman, S.A. Barnett, J.E. Sundgren, J.E. Greene, *J. Cryst. Growth* 92, 639–656 (1988).
2. W.D. Sproul, P.J. Rudnik, M.E. Graham, S.L. Rohde, *Surf. Coat. Technol.* 43, 270–278 (1990).
3. M. L. Kuruppu, G. Negrea, I. P. Ivanov, and S. L. Rohde, *Journal of Vacuum Science and Technology A*, 16(3),1949-1955 (1998).
4. P. Patsalas, C. Charitidis, S. Logothetidis, *Surf. Coat. Technol.* 125, 335–340 (2000).
5. P.H. Mayrhofer, F. Kunc, J. Musil, C. Mitterer, *Thin Solid Films* 415, 151– 159 (2002).
6. G. Abadias, P. Guerin, *Appl. Phys. Lett.* 93, 111908 (2008).
7. S. Mahieu, D. Depla, *J. Phys. D: Appl. Phys.* 42, 053002 (2009).
8. S. Mahieu, P. Ghekiere, D. Depla, R. De Gryse, *Thin Solid Films* 515, 1229 (2006).
9. J.A. Thornton, *J. Vac. Sci. Technol. A* 4, 3059–3065 (1986).
10. A. Anders, *Thin Solid Films* 518, 4087–4090 (2010).
11. R.Kröger, M.Eizenberg, C.Marcadal, L.Chen, *J.Appl.Phys*.91, 5149–5154 (2002).
12. Z.Peng, H.Miao, L.Qi, S.Yang, C.Liu, *ActaMater.*51, 3085–3094 (2003).
13. R.W.Poon, J.P.Ho, X.Liu, C.Chung, P.K.Chu, K.W.Yeung W.W. Lu, K.M.Cheung, *Thin Solid Films* 488, 20–2 (2005)
14. N.K.Ponon, D.J.Appleby, E.Arac, P.King, S.Ganti, K.S.Kwa, A. O'Neill, *Thin Solid Films* 578,31–37 (2015)

15. T.-S.Yeh, J.-M.Wu, L.-J.Hu, *Thin Solid Films* 516, 7294–7298 (2008).
16. B. Window, *Surface and Coatings Technology*, 81(1), 92-98 (1996).
17. J. Musil, S. Kadlec, J. Vyskočil, V. Valvoda, *Thin Solid Films*, 167(1-2), 107-120 (1988).
18. M. Ohring, "The Materials Science of Thin Films", Academic Press, New York, (1992).
19. J. -E. Sundgren, B.O. Johansson, A. Rockett, S.A. Barnett, J.E. Greene, „American Institute of Physics- Conference Proceedings", 149, 95-115 ,(1996).
20. J.C. Oliveira, F. Fernandes, R. Serra, A. Cavaleiro, *Thin Solid Films* 645, 253-264 (2018). 21. A A Kozin, V I Shapovalov, V V Smirnov, A S Useinov,К S Kravchuk, E V Gladkikh, A V Zavyalov and A A Morozova , IOP Conf. Series: *Journal of Physics: Conf. Series* **872** (2017) 012019

STUDIA UBB PHYSICA, Vol. 63 (LXIII), 1-2, 2018, pp. 89-99
(RECOMMENDED CITATION)
doi:10.24193/subbphys.2018.08

STRUCTURAL AND OPTICAL CHARACTERIZATION OF ZnO FILMS DOPED WITH Ni

M. TOMA[1,2,*], C. LUNG[1], D. MARCONI[1,3], A. POP[1]

ABSTRACT. Zinc oxide (ZnO), and Ni-doped ZnO (NZO) thin films were deposited on glass substrates by radio frequency (RF) magnetron sputtering for three different distances between substrate-target. The influence of the distance between substrate-target upon structure of the thin films was analyzed by X-ray diffraction (XRD) and the grain size was determined by theoretical calculations. Optical transmission measurements show the influence of doping and distance between substrate-target on the optical band gap.

Keywords: *XRD, transmittance, Ni-ZnO thin films, RF magnetron sputtering*

INTRODUCTION

It is not a novelty that zinc oxide is used to generate energy, however, its field of application has never ceased to expand by doping with various impurities to improve its optical and electrical qualities. Because

[1] *Babes-Bolyai University, Physics Faculty, M. Kogalniceanu No.1, 400084, Cluj-Napoca, Romania*
[2] *Research Center for Advanced Medicine Iuliu Hatieganu University of Medicine and Pharmacy, 400337, Cluj-Napoca, Romania*
[3] *Department of Molecular and Biomolecular Physics, National Institute for Research and Development of Isotopic and Molecular Technologies, Cluj-Napoca, Romania*
[*] *Corresponding author: mary02.toma@gmail.com*

ZnO is cheaper, non-toxic and more abundant in nature it has more advantages compared to ITO films (indium tin oxide). Also, being chemically stable to hydrogen plasma processes, doped-ZnO thin films are used to produce solar cells [1], gas sensors [2-4], diodes [5], display devices [6], spintronics [7], air filters [8] etc. These impurities work as a donor for the metallic ZnO when it replaces an occupied Zn^{2+} state or a state in between the zinc oxide composition structures, the donor offering the optical transparency.

The Ni-doped ZnO (NZO) can be analyzed in many forms such as powders, nanostructures, nanoparticles and thin layers. Some recent articles regarding Ni-doped ZnO thin films, it was found that a lower Ni concentration (3% -5%) possesses better crystallinity and a higher magnetic moment [9]. Furthermore, a concentration of 12% Ni show that with the introduction of Ni, the refractive index (ne) decreases as a result of doping. This decrease can be explained by the annihilation of oxygen vacancies, but the same method shows that the prepared samples also showed ferromagnetic properties [10]. Thus, NZO study still leaves room for progress. Although Ms has values smaller than those of ZnO: Co, Ni remains one of the most promising and most used dopants in the transitional metals group.

For fabricating metal oxide thin films and related materials, radio-frequency magnetron sputtering technique is considered one of the best deposition methods, as it allows growth of uniform thin films at low temperature with high reproducibility and with strong adhesion to substrates over large area surfaces [11].

In the present study, we present the structural and optical characterization of NZO thin films obtained by FR magnetron sputtering. This technique is often used to deposit thin films because of its efficiency, low cost and good reproducibility [12]. Thus, taking into account the decrease of the distance between the target substrate and the residual compressive stress at the film-substrate interface arising during the film growth, significant changes in the structural and optical properties have occurred.

EXPERIMENTAL DETAILS

We prepared two ceramic targets, one undoped using just ZnO of 99.99% purity, that acts as a reference for the next one that was doped with NiO (3% w.p.) obtained by solid state reaction method, using mechanically mixed powders of ZnO (99.99% purity), NiO (99.99%). They were mechanical processed at a pressure of 490 MPa and annealed at a temperature of 930 °C for 60 minutes. The deposition was performed on soda-lime glass substrates heated at a constant temperature of 150 ^{o}C and a controlled atmosphere of O_2 and Ar, having the mass flows d_{Ar} and d_{O2}. The RF-power density was 19.72 W/cm^2 and the deposition pressure was maintained at 6×10^{-2} mbar and the deposition time was maintained constant at **a value of 90 minutes**.

The films thicknesses, t, measured with a quartz monitor were around t=105 nm for d=4 cm, t=45 nm for d=6 cm and t=15 nm for d=8 cm, respectively. This result show that the growth rate (*R*) decreases as the substrate to target distance increases.

The crystal phases were identified by comparing the 2θ values and intensities of reflections on X-ray diffractograms with JCP data base using the Diffraction AT-Brucker program. Optical transmission measurements were done with a Carry 500 Spectrometer (300 nm – 1000 nm range). From the transmission spectra, the optical constants were calculated using the program PARAV-V2.0 [13].

RESULTS AND DISCUSSIONS

A. Structural measurements

For the preparation of films, we started by synthesizing two ceramic targets, the zinc oxide first, and the second was prepared by adding nickel oxide to the ZnO composition with 3% NiO (99.99% purity) and 97% percent ZnO mass (purity 99.9%). The percent fraction calculated from the diffractogram

respects the percentages in the recipe used by 97% ZnO and 3% NiO, respectively. However, the fact that the calculated percentage of the diffractogram is 2.2% (*table 1*) shows that in the solid phase reaction method NiO did not react completely, as emphasized in the experimentally obtained diffractogram (see *figure 1*).

Table 1. Calculated phase percentage

Name	**Formula**	**Matched phase**	**Quantity (%)**
Zinc oxide	O Zn	Zincite	97.8
Nikel oxide	Ni O		2.2

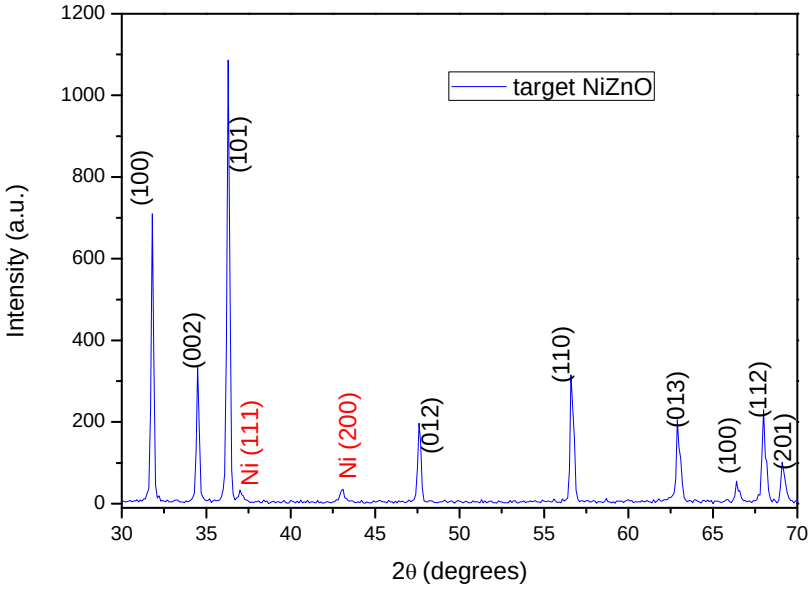

Figure 1. XRD pattern of NZO target

Targets were analyzed by X-ray diffraction, and the diffraction peaks obtained for an angle scan of 2Θ, in the range of 30° and 70°, with the Miller indeces (100), (002), (101), (012), (110), (013), (112) and (201) are assigned

to the crystalline planes of ZnO. NiO, (111) and (200) diffraction peaks are also observed, which means that the parameters of the solid phase reaction method used for target synthesis were not optimal.

Films were deposited at three different distances between target-substrate, namely 4 cm, 6 cm and 8 cm respectively, aiming to optimize the manufacturing parameters as well as improving their structural and optical properties.

The crystallite size was calculated with Scherrer's equation: $D = \frac{0.9\lambda}{B\cos\theta}$

where λ, ϑ, and B are: the X-ray wavelength $\lambda_{CuK\alpha 1}$, diffraction angle and FWHM (full width at half maximum) of the (002) diffraction peak, respectively [14].

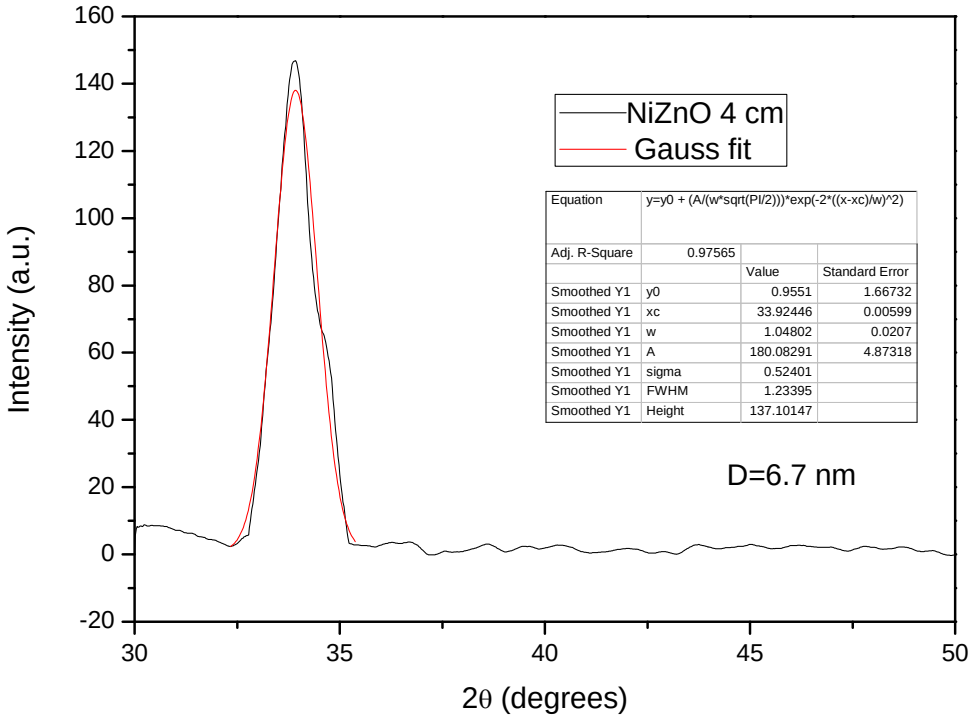

Figure 2. Diffractogram pattern of NZO film deposited at a distance of 4 cm

The films deposited at d = 4 cm (figure2) and d = 6 cm (figure3) have a preferential orientation along the c axis, perpendicular to the surface of the substrate, and the diffraction peaks correspond to 33.9 ° and the wound structure, according to the study of the literature [15]. The crystallite size is influenced by the distance between substrate-target, *d,* for NZO doped films (see *Table 2*).

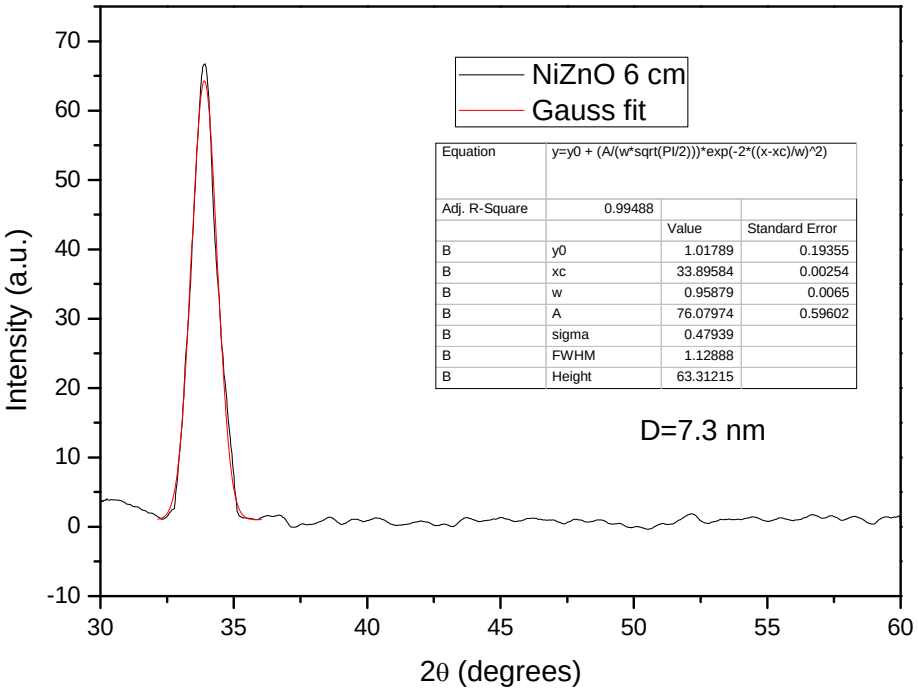

Figure 3. Diffractogram pattern of NZO film deposited at a distance of 6 cm

Table 2. Structural and optical characteristics of NZO thin films

Sample name	d (cm)	D (nm)	t (nm)	E_g (eV)	n (nm)
NZO	4	6.7	105	3.23	1.92
NZO	6	7.3	45	3.26	
NZO	8	-	15	3.28	

Diffractograms belonging to the above-mentioned films are made up of a single maximum of diffraction, which corresponds to the crystalline planes with Miller indices (002). In the case of the film deposited at d = 8 cm, the X-ray diffraction was inconclusive because it is the thinnest, respectively 15 nm.

The values of the thin film parameters shown in *Table 2*, with respect to the size of the crystals obtained using the Scherrer equation. These values increase with the increase of the distance between target-substrate, the ***optimum distance with the best crystallinity being 6 cm*** in agreement with the result of the correlation coefficient illustrated in *Figure 3.*

B. Transmittance measurements

Optical transmittance measured as function of wavelength (in the region 375-1000 nm) for NZO films using an ellipsometer J.A. Wollam, the results are illustrated in *Figure 4* and *Figure 5.* By ellipsometry measurements we determined the optical band gap and the thickness of NZO thin films. Optical constants were determined from reflection, and then the thickness of each film was calculated*. Using the Complete EASE program, a fitting process was made between the measurements and the model, thus determining the thickness of the films.* The data shows that the films are transparent in the visible region. The effect of distance between target- substrate on the optical transmittance, thickness of the films, t, and the band gap (E_g) values of the films have been studied by using the program PARAV [13].

The optical band gap is given by the energy difference between Fermi pulse states in the band and the valence band.

The linearity of the plot of (□h□)^2 versus 'h□' indicates a direct transition [16]. By increasing d from 4 cm to 8 cm, the optical band gap E_g value were the same for all samples, which is in accordance with other literature results (*see table 2*).

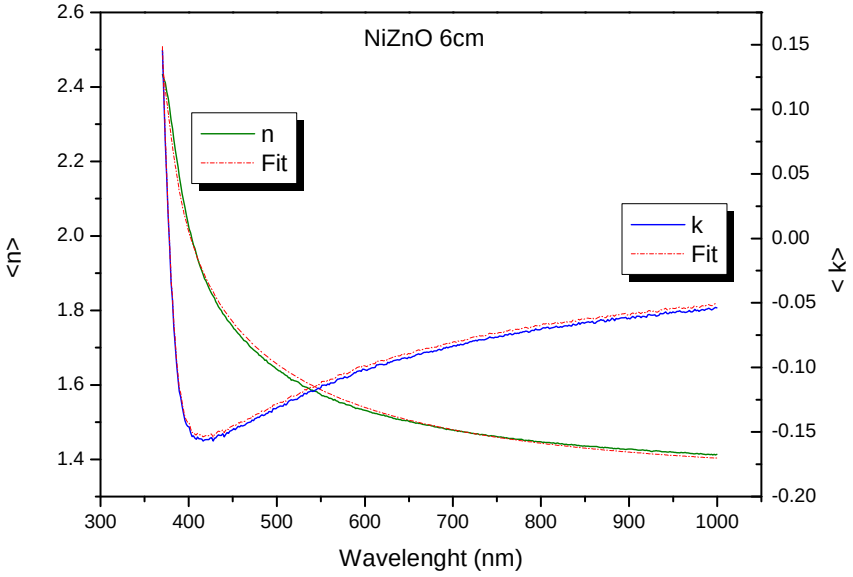

Figure 4. Ellipsometric measurements and fitting pattern for NZO film deposited at d = 6 cm

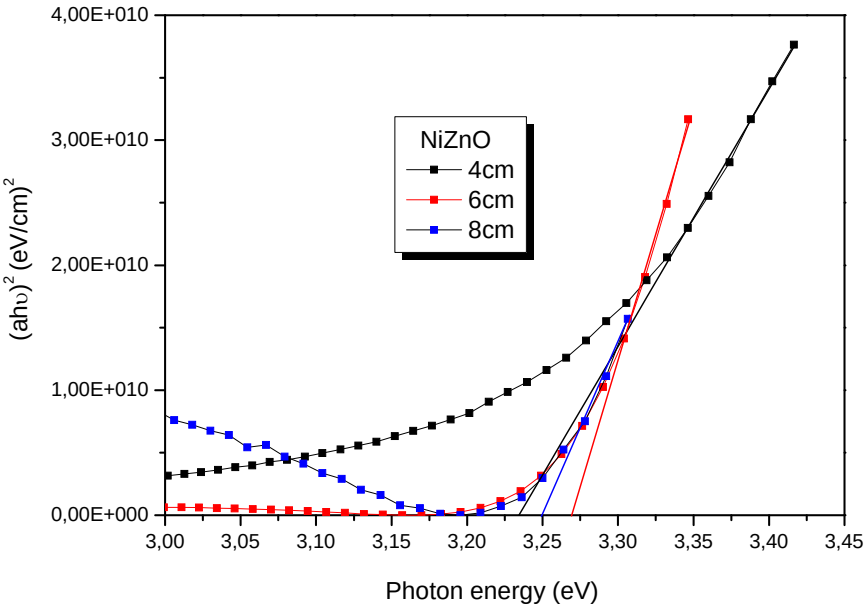

Figure 5. Tauc plotting of NZO thin films obtained for three distances

The band gap, E_g, was determined according to the Tauc relation:

$$(\alpha h\nu)^2 = A^2(h\nu - E_g),$$

where A is a constant that depends on the electron-hole mobility, h is Planck's constant. The optical absorption coefficient is defined as $\alpha = \frac{1}{t}\ln\frac{(1-R)^2}{T}$, where t is the thickness of the thin films [17].

To entail, the optical band gap and the absorption limit of the nanostructured materials is shifted due to the quantum effects because of the dimensions (the electronic properties differ with particle size reductions) [18].

For the film deposited at 4 cm, the value of E_g is 3.23eV and with the increase of the target-substrate distance, the E_g value increases as shown in *table 2.*

CONCLUSIONS

Ni doped ZnO thin films were deposited on glass substrates by RF magnetron sputtering method. The effect of Ni doping on the optical and structural properties of ZnO films was analyzed.

From the XRD measurements it was found that the values for the grain size was between 6.7 nm and 7.3 nm depending on the target-substrate distances used. The diffraction pattern of to the films deposited at d = 4 cm and d = 6 cm show a single peak, corresponding to the crystalline planes with Miller indices (002). Furthermore, the films deposited at d = 4 cm and d = 6 cm have a preferential orientation along the c axis, perpendicular to the surface of the substrate, and the diffraction peaks correspond to 33.9 ° of the wurtzite structure.

The maximum value of E_g was obtained for the film deposited at a distance of 6 cm, this being 3.26 eV. The refractive index, n, calculated at the specific wavelength of 632.8 nm, has the same value for all three films obtained.

Thus, these results emphasize that the optimum distance between target-substrate was 6 cm, where the crystallinity as well as optical properties show good results.

REFERENCES

[1] S.Ilican, Y.Caglar, M. Caglar, B. Demirci, Polycrystalline indium-doped ZnO thin films: preparation and characterization, Journal of optoelectronics and advanced materials, 10, 10, 1, (2008).

[2] M. Suchea, S. Christoulakis, K. Moschovis, N. Katsarakis, G. Kiriakidis, ZnO transparent thin films for gas sensor applications, Thin Solid Films, 515, 551-554, (2006).

[3] Jia Huang, Zhigang Yin, Qingdong Zheng, Applications of ZnO in organic and hybrid solar cells, Energy&Environmental Science, 4, 3861-3877, (2011).

[4] I. G. Dimitrov, A Og Dikovska, P. A. Atanasov et. al., Al doped ZnO thin films for gas sensor application, Journal of Physics: Conference series, 113, **1**, (2008).

[5] Chennupati Jagadish and Stephen J. Pearton, Nanostructures, Elsevier, Amsterdam, (2006).

[6] U. Ozgur, Ya. I. Alivov, C. Liu, A. Teke, M. A. Reshchikov, S. Dogan, V. Avrutin, S. J. Cho, H. Morkoc, J. Appl. Phys. 98, 041301, (2005).

[7] S. Calnan, A.N. Tiwari, Thin Solid Films 518 (7), p.1839–1849, (2010).

[8] C. Kingshirn, ChemPhysChem 8, 782-803, (2007).

[9] *E. Liu, P. Xiao, J.S. Chen, B.C. Lim, L. Li, Ni doped ZnO thin films for diluated magnetic semiconductor materials, Current Applied Physics, 8, 408-411, 2008*

[10] Zhigang Yin, Nuofu Chen, Fei Yang, Shulin Song, Chunlin Chai, Jun Zhong, Haijie Qian, Kurash Ibrahim, *Structural, magnetic properties and photoemission study of Ni-doped ZnO*, Solid State Communications, 135, 430-433, (2005).

[11] J.Lee, D. Lee, D. Lim and K. Yang, Thin Solid Films 515, p. 6094-6098, (2007).

[12] C. Lung, D. Marconi, Maria Toma and A.V. Pop, Analytical Letters 49:8, p. 1278-1288, (2016).

[13] A. Ganjoo, R. Golovchak, J. Opt. Adv. Mat. Vol. 10, nr.6, p. 1328–1332, (2008).

[14] Toma Maria-Iuliana, Studiul și analiza filmelor subțiri de ZnO dopate cu Al și elemente 4f, (2014).

[15] Zhigang Yin, Nuofu Chen, Fei Yang, Shulin Song, Chunlin Chai, Jun Zhong, Haijie Qian, Kurash Ibrahim, *Structural, magnetic properties and photoemission study of Ni-doped ZnO*, Solid State Communications, 135, 430-433, (2005).

[16] U. Alver, T. Kilinc, E. Bacaksiz, T. Kucukomeroglu, S. Nezir, I.H. Mutlu, F. Aslan, Thin Solid Films 515, p. 3448-3451, (2007).

[17] C. Lung, M. Toma, M. Pop, D. Marconi, A. Pop, Characterization of the structural and optical properties of ZnO thin films doped with Ga,Al and (Al+Ga), Journal of Alloys and Compounds, doi: 10.1016/j.jallcom.2017.07.265, (2017).

[18] Alia Colniță, Daniel Marconi, Ioan Turcu, *Fabrication of interdigitated electrodes using molecular beam epitaxy and optical lithography,* Analytical letters, 49, 3, (2017).

STUDIA UBB PHYSICA, Vol. 63 (LXIII), 1-2, 2018, pp. 101-110
(RECOMMENDED CITATION)
doi:10.24193/subbphys.2018.09

DISPERSION EQUATION FOR PLASMA WAVE PROPAGATION AT THE INTERFACE OF A STOCHASTIC ENVINRONMENT

A. MARCU[1,*], G. MOCANU[†]

ABSTRACT. The present paper investigates the effect of a stochastic term in the equation of motion in the MHD approximation. The end purpose is to find whether or not, for the case of an interface between two media of different physical properties, the stability behavior of the waves characteristic to the interface changes. Our results show that, for a certain parameter set, the stability behavior does change: namely a configuration which is stable in the deterministic approach may become unstable when stochastic effects are considered.

Keywords: *MHD waves, Stochastic processes, instabilities*

1. SHORT INTRODUCTION IN THE PHYSICS OF STOCHASTIC PROCESSES

The archetypical **Brownian Motion** [4] consists of a massive particle subjected to two types of forces: a frictional force, that dissipates the kinetic energy of the particle and a random force that pushes the particle in an erratic way. This random force stands for the effects of the interactions (collisions) of the particle with all the other particles in the system. The characteristics

[1] *Babes Bolyai University, Faculty of Physics, Kogalniceanu Street no. 1, Cluj-Napoca, Romania*
[†] *Romanian Academy, Cluj-Napoca Branch, Astronomical Observatory, Ciresilor Street no. 19, Romania*
** Corresponding author: gabriela.mocanu@academia-cj.ro*

(mean value and variance) of the random term are determined by the energy content available in the system. The archetypical Brownian motion assumes that the many particle system is in contact with a heat reservoir. However, the energy content of the system might also be given by the presence of a magnetic field and so on. The development of the Brownian motion toy model was necessary in order to be able to perform analytical treatment on systems of many coupled interacting elements. Insight to this problem may be gained by using inferences about the statistical behaviour of the particle interaction. One studies the motion of just one particle and considers that the influence of all the other particles is given by the action of a stochastic force with certain statistical properties. As such, we will only have access to information regarding macroscopic characteristics of the underlying processes.

The system under analysis consists of *N* Brownian particles, "living" in an isotropic 3 dimensional coordinate space, of a finite volume and moving with friction. Each Brownian particle is characterized by a mass m, position r and velocity v. Due to friction, one part of the deterministic force will be given by $-\nu v$, with ν the friction coefficient acting on the particle. The rest of the deterministic force can be derived from a potential $U\ (r1,..,rN\ )$. The fluctuations in velocity space are given by realizations of a Gaussian-like process (i.e. they are Gaussian random variables), characterized by diffusion coefficients B. At thermodynamic equilibrium the values of the diffusion coefficients are constrained by the value of the temperature of the system. The velocity is then itself a stochastic variable. For a zero external potential, historically, this velocity is called Brownian motion. The general mathematical name is Wiener process.

Taking the above considerations into account, the A-Langevin equation describing the system may be written as

$$\frac{d\mathbf{v}}{dt} = -\nu\mathbf{v} - \frac{1}{m}\nabla U(\mathbf{r}_1, .., \mathbf{r}_N) + \sqrt{2B}\vec{A}_t(t), \tag{1.1}$$

where

$$\mathbf{v} = \frac{d\mathbf{r}}{dt}, \tag{1.2}$$

and $\vec{A}_t$ is white noise of parameter t with statistical properties

$$\langle \vec{A}_t(t) \rangle = 0, \tag{1.3}$$

$$\langle A_{ti}(t) A_{tj}(t') \rangle = \sigma \delta_{ij} \delta(t - t'). \tag{1.4}$$

A property of white noise is that its derivative is the Wiener process β_t

$$A_t = \frac{d\beta_t}{dt} \tag{1.5}$$

where the properties of the Wiener process are

- $\beta_0 = 0$
- β_t is almost surely continuous
- β_t has independent increments
- $\beta_t - \beta_s \in \mathcal{N}(0, t - s)$.

2. POSING OF THE PROBLEM AND ALGORITHM

The common feature of all types of classical wave analysis is the fact that the adopted mathematical model of the phenomenon is deterministic. It turns out, that – just as in investigation of many other phenomena – deterministic modelling of waves does not always result in an adequate presentation of reality. Because of the existence of many uncontrolled factors determining real wave processes a stochastic description, i.e., one based on probability theory, is often more adequate. A stochastic nature of real wave processes results above all from the inhomogeneity and uncertainty of the structure of most wave - transmitting media. In order to account for the complexity of real media one usually introduces a mathematical model called a stochastic or random medium. In general, this means a medium whose properties are described in terms of probability theory, or, more specifically, by means of random functions $A(\vec{r}, t)$ of position and time. *Temporal variations of the properties of the medium are often very slow; consequently, we mostly use a spatial random field* $A(\vec{r}, t)$ which can take

scalar, vector or tensor values depending on the particular situation. A random field $A(\vec{r},t)$ may possess continuously and smoothly varying sample functions, or it may just be a discrete - valued random function [3].

The purpose of this work is to study the effect of a stochastic force on wave propagation in ionized plasmas. The route undertaken is to work in the MHD framework in an A-Langevin equation approach, i.e., to include a stochastic term in the equation of motion.

The general approximation is that the stochastic term is seen as constant by the fluid, i.e., the characteristic timescale of the noise is much smaller than any characteristic timescale of the fluids, such that $\vec{A}=\vec{A}_z(z)$.

3. GOVERNING EQUATIONS AND BASIC ASSUMPTIONS

We consider the case of the interface between two media; particular numerical values are taken for an interface between the solar corona and a prominence. We will follow closely the derivation in [1].

The starting linearized equations are

$$\nabla\cdot\vec{v}_i=0,\quad \nabla\cdot\vec{b}_i=0\quad i\in\{1,2\},\tag{3.1}$$

for the perturbed velocity and magnetic field in both regions. The momentum equations are

$$\rho_1\frac{\partial\vec{v}_1}{\partial t}=-\nabla P_1+\frac{B_{01}}{\mu_0}\frac{\partial\vec{b}_1}{\partial x}+\rho_1\mathcal{V}+\vec{A}_1,\tag{3.2}$$

$$\rho_2\frac{\partial\vec{v}_2}{\partial t}+\rho_2 v_0\frac{\partial\vec{v}_2}{\partial x}=-\nabla P_2+\frac{B_{02}}{\mu_0}\frac{\partial\vec{b}_2}{\partial x}+\vec{A}_2,\tag{3.3}$$

where $\vec{A}_i=\left(A_{ix},A_{iy},A_{iz}\right)=\imath\vec{W}_z e^{\imath(k_x x-\omega t)}$ and $\vec{W}_z$ is Gaussian white noise in argument z

$$\langle\vec{W}_z(z)\rangle=0,\quad \langle W_{zi}(z)W_{zj}(z')\rangle=\sigma\delta_{zz'}\delta_{ij}.\tag{3.4}$$

The term $\vec{A}$ has complex amplitude in our approach because we will use these equations to perform the usual normal mode analysis. Since the noise term is akin to the friction term and we know that friction will lead to an imaginary component in the dispersion equation, we make sure that the noise term will have a similar kind of contribution by making the amplitude of A complex.

The induction equations are

$$\frac{\partial \vec{b}_1}{\partial t} = B_{01}\frac{\partial \vec{v}_1}{\partial x}, \tag{3.5}$$

$$\frac{\partial \vec{b}_2}{\partial t} + v_0\frac{\partial \vec{b}_2}{\partial x} = B_{02}\frac{\partial \vec{v}_2}{\partial x} + \mathcal{R}, \tag{3.6}$$

where

$$\mathcal{V} = 3\nu\left[\tilde{\vec{b}}\left(\tilde{\vec{b}}\cdot\nabla\right) - \frac{1}{3}\nabla\right]\left[\tilde{\vec{b}}\cdot\left(\tilde{\vec{b}}\cdot\vec{v}_1\right)\right], \quad \tilde{\vec{b}} = \vec{b}/|\vec{b}|, \tag{3.7}$$

$$\mathcal{R} = \eta\nabla^2\vec{b}_2 + \frac{(\eta_c - \eta)}{|\vec{B}_0^2|}\nabla\times\left\{\left[(\nabla\times\vec{b}_2)\times\vec{B}_0\right]\times\vec{B}_0\right\}. \tag{3.8}$$

Jump condition at the interface

Imposing the jump condition is done as follows: consider the z component of the equation of motion, denoting it by α. Use the approximation of one dimensional steady state $\nabla\rightarrow\hat{z}\frac{d}{dz}$ and $\partial/\partial t = 0$ and the two equations of motion become

$$\frac{d}{dz}\alpha = 0 \tag{3.9}$$

where

$$\begin{aligned}\alpha &= -P_1 + \rho_1\nu\frac{\partial v_z}{\partial z} + \imath\beta_{z1}e^{\imath(k_x x-\omega t)} \text{ for region 1} \\ &= -P_2 + \beta_{z2}e^{\imath(k_x x-\omega t)} \text{ for region 2}\end{aligned} \tag{3.10}$$

Integrating across the surface, from region 1 to region 2

$$\int_1^2 \frac{d\alpha}{dz} dz = 0 \text{ yields } \alpha(2) = \alpha(1) \tag{3.11}$$

i.e.

$$-P_1 + \rho_1 \nu \frac{\partial v_z}{\partial z} + \imath \beta_{z1} e^{\imath(k_x x - \omega t)} = -P_2 + \imath \beta_{z2} e^{\imath(k_x x - \omega t)}. \tag{3.12}$$

Normal mode analysis

The usual procedure at this point in MHD wave theory is to perform normal mode analysis (NMA). This means looking for solutions of some imposed type, where the time behavior is swept under the rug as an exponential $\sim e^{-\imath \omega t}$. Normal mode analysis does not use the extra step of integrating that the Fourier analysis uses.

For illustration purposes, consider the Langevin equation

$$\frac{dv}{dt} = -\nu v + \tilde{A}, \tag{3.13}$$

where $\tilde{A}$ is a noise term of known statistical properties. Decide that you want to perform NMA for this equation. That means that you will look for a solution of the type $v = \hat{v}(z)\ exp\{\imath(k_x x - \omega t)\}$. The equation then becomes

$$-\imath\omega\hat{v} \exp\{\imath(k_x x - \omega t)\} = -\nu\hat{v} \exp\{\imath(k_x x - \omega t)\} + A, \tag{3.14}$$

and thus

$$-\imath\omega\hat{v} = -\nu\hat{v} + A \exp\{-\imath(k_x x - \omega t)\}. \tag{3.15}$$

The term $A\ exp\{-\imath(k_x x - \omega t)\}$ is a noise term, of known statistical properties. We may denote it by some other symbol and carry on the usual calculations. Note that when we will apply this approach to the MHD equations ofmotion, $\vec{A}\ exp\{-\imath(k_x x - \omega t)\}$= $\imath\vec{W}_z$.

For the more complex set of MHD equations, we proceed exactly as in [1]. Technically, we will obtain the dispersion equation for the case in which the equations of motion are not homogeneous.

Because the mean of the white noise is zero, we obtain, just as in [1] the expressions for the two pressures

$$P_1 = \zeta \frac{\rho_1}{k_x}\left(D_{A1} - \frac{\imath}{2}k_x^2 \nu\omega\right) \tag{3.16}$$

$$P_2 = -\zeta \frac{\rho_2 D_{A2}}{k_x}\left(1 + \frac{\imath}{2}\frac{k_x^2 \eta_C}{\Omega}\right). \tag{3.17}$$

The jump condition in the NMA assumption (using the expressions for the pressure Eqs. (3.16)-(3.17)) becomes

$$-\imath\beta_{z1} + \zeta\left(\frac{D_{A1}}{k_x}\rho_1 + \frac{\imath}{2}k_x \nu\rho_1\omega\right) = -\imath\beta_{z2} - \zeta\left(\frac{D_{A2}}{k_x}\rho_2 + \imath\frac{D_{A2}k_x\eta_C\rho_2}{2\Omega}\right). \tag{3.18}$$

The result obtained for the dispersion equation is

$$D(\omega) = D_r + \imath D_i = 0, \tag{3.19}$$

where in this case

$$D_r = D_{A1} + dD_{A2}, \tag{3.20}$$

and it does not contain a stochastic term, and

$$D_i = \beta + \frac{1}{2}\left(k_x^2\nu\omega + \frac{dD_{A2}k_x^2\eta_c}{\Omega}\right), \quad \text{with } \beta = \frac{\beta_{z2} - \beta_{z1}}{\zeta_0}, \tag{3.21}$$

where ζ_0 is the perturbation at the interface calculated for some typical scale of the plasma, and the stochastic term is beta.

4. RESULTS

We now follow the algorithm in [2] and find ω_0 as a solution of $D_r = 0$. This is a second order algebraical equation which produces two solutions, ω_0^+ and ω_0^-. These are identical to the ones obtained in the deterministic case, since there is no stochastic term in D_r.

Further, it is assumed that the terms in D_i produce a perturbation $\delta\omega$ and as such $\delta\omega$ is obtained by a Taylor expansion of $D(\omega)$ for $\omega = \omega_0 + \delta\omega$; it will thus present with two solutions (for each of the ω_0): $\delta\omega_+$ and $\delta\omega_-$.

As shown in [2],

$$\delta\omega(\omega_0) = -\left(\frac{1}{\partial D_r(\omega)/\partial\omega} D_i(\omega)\right)|_{\omega=\omega_0}, \tag{4.1}$$

and so

$$\delta\omega(\omega_0) = -\frac{\left[2\beta + k_x^2\nu\omega + \frac{dk_x^2\eta_c(-k_x^2v_{A2}^2+(-k_xv_0+\omega)^2}{-k_xv_0+\omega}\right]}{4\omega + 4d(-k_xv_0+\omega)}\Bigg|_{\omega=\omega_0}. \tag{4.2}$$

We checked that at all times the ratio between the perturbation frequency and ω_0 is very small, of the order 10^{-5} (Figure 1).

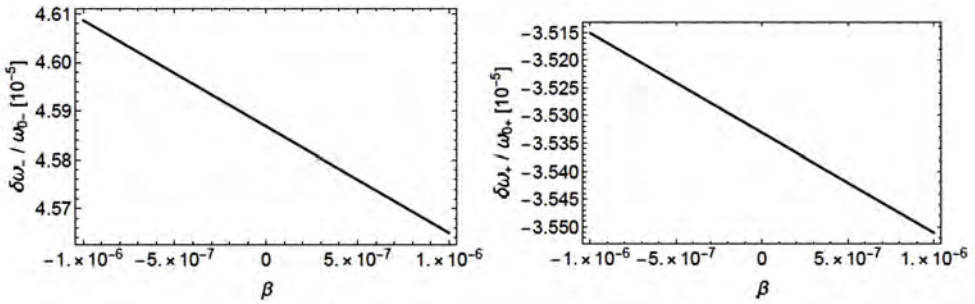

Figure 1. Ratio of the frequency $\delta\omega$ to its corresponding ω_0.

If the $\delta\omega$ are positive, an instability appears.

In the limit $\beta \to 0$ the classical result is recovered, in which $\delta\omega$ is always negative. However, allowing for a nonzero β leads to positive values of the $\delta\omega$, and thus the appearance of instability.

Analytically, the condition that $\delta\omega > 0$, i.e., there is instability, has the form

$$\beta > \frac{1}{8}\left[\omega + d\Omega - 4k_x^2\omega\nu + \frac{4d_x^2\eta_C D_{A2}}{\Omega}\right]\Bigg|_{\omega=\omega_0}. \tag{4.3}$$

So for each of the two cases

$$\delta\omega_- > 0 \text{ if } \beta > \frac{1}{8}\left[\omega + d\Omega - 4k_x^2\omega\nu + \frac{4d_x^2\eta_C D_{A2}}{\Omega}\right]\Big|_{\omega=\omega_{0-}}. \quad (4.4)$$

$$\delta\omega_+ > 0 \text{ if } \beta > \frac{1}{8}\left[\omega + d\Omega - 4k_x^2\omega\nu + \frac{4d_x^2\eta_C D_{A2}}{\Omega}\right]\Big|_{\omega=\omega_{0+}}. \quad (4.5)$$

For $\beta \to 0$, the deterministic case of [1] is recovered and the $\delta\omega$ frequencies are negative. Since in the absence of noise, the frequencies are always negative, the mathematical result is that the presence of a stochastic component is a source of instability. The condition for instability says that there will be instability at the interface provided that the noise difference on the two sides of the interface exceeds a certain threshold.

This can be seen for both solutions of the $\delta\omega$ in Figure 2, for parameter values used in [1].

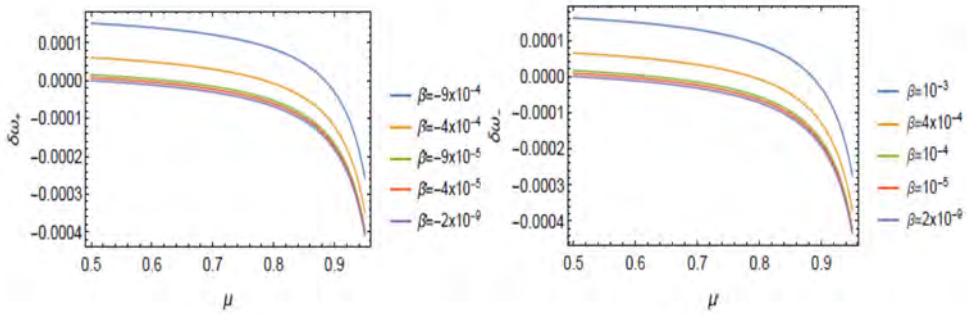

Figure 2. Variation of $\delta\omega$ as a function of the ionization parameter μ, for different values of the parameter β, which quantifies the influence of the noise. The numerical values used to obtain the plots are: $T_2 = 10^4$, $\nu = 10^{-10}$, $k_x = 5 \cdot 10^{-6}$, $\rho_2 = 5 \cdot 10^{-11}$, $v_{a1} = 315000$, $v_{a2} = 28000$, $v_0 = 20000$, $d = \sqrt{10}$.

Forward mode

Let us focus on the forward mode, i.e., the one identified by ω_{0+} and $\delta\omega_+$. The results obtained for the deterministic case are shown in Figure 3. It is always negative, i.e., stable. But as seen in Figure 2 left, there are combinations of $\{\mu, \beta\}$ for which $\delta\omega_+$ becomes positive.

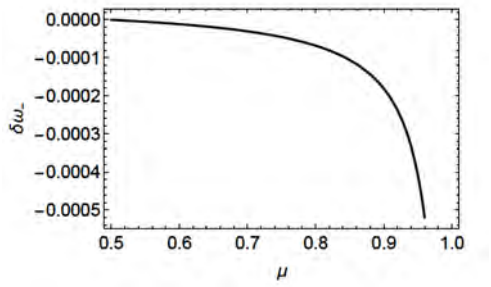

Figure 3. Variation of $\delta\omega$ in the forward wave case, as a function of the ionization parameter μ, for $\beta = 0$.

5. CONCLUSIONS

In the present paper the MHD approximation was considered for the case of an interface between two plasmas with different properties. A stochastic term was allowed for in the equation of motion. With the purpose of obtaining a dispersion equation for the waves present at the interface, the jump condition between the two media was obtained. Numerical implementation of the dispersion equation indeed shows that a stochastic term might change the stability behavior of the system.

ACKNOWLEDGEMENTS

This work was supported by a grant of the Ministry of National Education and Scientific Research, RDI Program for Space Technology and Advanced Research - STAR, project number 181/20.07.2017.

REFERENCES

1. Ballai, I., Oliver, R., & Alexandrou, M. 2015, A&A, 577, A82 (2015)
2. Cairns, R.A., *J. Fluid. Mech.,* 92, 1 (1979)
3. Sobczyk, K., Stochastic waves: The existing results and new problems, *Probabilistic Engineering Mechanics*, 1, 3, 1986
4. P. Talkner and J. Luczka, Brownian Motion in a d-Dimensional Space with Fluctuating Friction, 2000, *Stochastic Processes in Physics, Chemistry and Biology*, J.A. Freund and T. Poschel (eds.), LNP 557, 85-96

STUDIA UBB PHYSICA, Vol. 63 (LXIII), 1-2, 2018, pp. 111-116
(RECOMMENDED CITATION)
doi:10.24193/subbphys.2018.10

STRUCTURAL AND MAGNETIC PROPERTIES OF FERROMAGNETIC Co-Zr ALLOYS OBTAINED BY MECHANICAL ALLOYING

R. HIRIAN[1], M. VALEANU[2], F. TOLEA[2], P. PALADE[2] AND V. POP[1,*]

ABSTRACT. The structural and magnetic properties of $Co_{11}Zr_2$ and $Co_{82}Zr_{12}$ ferromagnetic alloys, produced via the non-equilibrium synthesis method of mechanical alloying, were investigated. The formation of the magnetic phases was investigated at milling times of up to 20 h. As the powders became amorphous during the alloying process, annealing was performed to allow for a more thorough investigation of the crystalline structure of the resulting alloys. The magnetic properties of the final samples were investigated via demagnetization curves.

Keywords: *mechanical alloying, rare-earth free permanent magnets, Co-Zr hard magnetic phase.*

INTRODUCTION

Permanent magnets are essential in industrial and technological applications, however a major disadvantage is that the materials for high performance permanent magnets contain large quantities of rare earths, which are exploited and processed in only a few regions on the globe, a major downside for industry as supply could always be shut off or the price

[1] *Faculty of Physics, Babeş-Bolyai University, Cluj-Napoca, RO-400084 Romania*
[2] *National Institute for Material Physics, P.O. Box MG-7, R-76900 Măgurele, Bucharest, Romania*
* *Corresponding author: viorel.pop@phys.ubbcluj.ro*

may inflate drastically in a short amount of time [1][2]. Therefore solutions to the dependence on rare earth materials are being sought. The $Co_{11}Zr_2$ hard magnetic phase has been proposed as a candidate material for rare-earth free permanent magnets [3-7], while the composition $Co_{82}Zr_{12}$ is a spring magnet [8] ($Co_{11}Zr_2$ as the hard magnetic phase and Co as the soft magnetic phase).

In this work we employ a non-equilibrium synthesis method, mechanical alloying (MA), in order to obtain the hard magnetic $Co_{11}Zr_2$ phase and hopefully exchange couple it with soft magnetic Co.

EXPERIMENTAL

The samples were made from elemental powders with the compositions $Co_{82}Zr_{12}$ and $Co_{11}Zr_2$. The powder mixtures were thoroughly mixed for half an hour, using a Turbula mixer and were then milled for up to 20 h in Fritsch Pulverisette 4 planetary ball mill, under purified Ar atmosphere. The ratio between the disk and planet speeds was 333 rpm/-900 rpm. The milling media is made of 440C steel. Nine 15 mm diameter balls were placed in each 80 ml steel vial which translates to an impact energy of 77 mJ/ball adding up to a total useful power of 5 W.

Differential scanning Calorimetry (DSC) measurements, carried out using a TA Instruments Q600 equipment, were done on the powders at different stages in the MA process.

The powders were annealed at 1030 °C for 7 days in order to ensure their homogeneity. The annealed samples were reheated to 1030 °C and kept there for 1 hour followed by quenching in water.

The structure of the samples was investigated by X-Ray diffraction (XRD) on a Bruker D8 Advance diffractometer equipped with a Cu Kα source.

The magnetic properties of the samples were investigated using a Cryogenics vibrating sample magnetometer, in applied fields of up to 4 T. The powder samples were blocked in epoxy resin for these measurements.

RESULTS AND DISCUSSION

DSC measurements were used to evaluate the MA process and to determine the annealing temperature required for the samples (Figure 1). After 2 h of MA we can see a large peak at low temperatures (convoluted signal from strain release and the phase transition of Co). Additional peaks are observed at high temperature due to the formation of various Co-Zr alloys. After 20 h MA we can see that only one sharp peak, at 620 °C, remains for the $Co_{11}Zr_2$ composition (Figure 1a), while for the $Co_{82}Zr_{12}$ samples we can still see a small peak (at 400 °C) indicative of the phase transition of Co (Figure 1b).

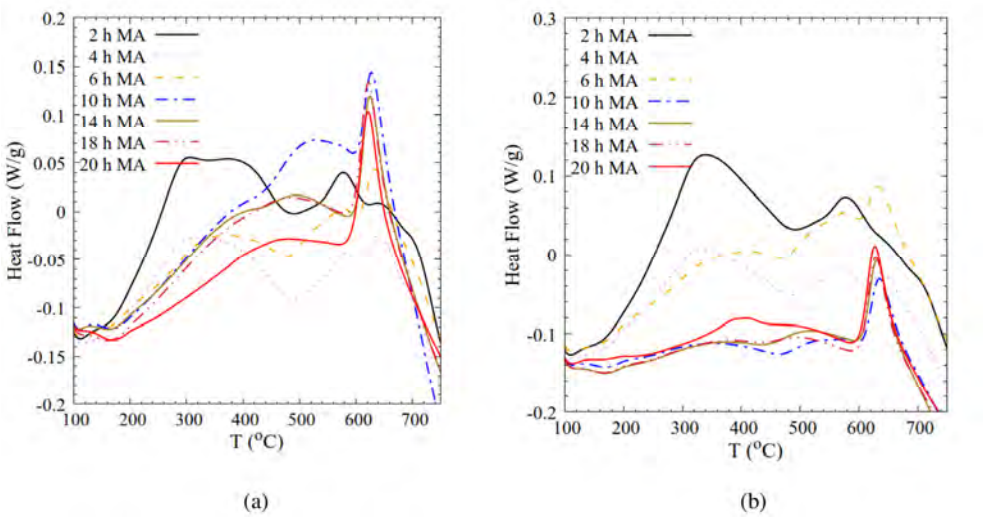

Figure 1. DSC curves for $Co_{11}Zr_2$ (a) and $Co_{82}Zr_{12}$ (b) MA powders at different milling times

The structure of the MA samples was investigated using XRD, Figure 2. We can see that for both compositions ($Co_{11}Zr_2$ and $Co_{82}Zr_{12}$), the samples become completely amorphous after 20 h MA, with only a very broad structure being visible. Because the 20 h MA powders seem to be fully alloyed, but amorphous, annealing at high temperature was used in order to recrystallize them.

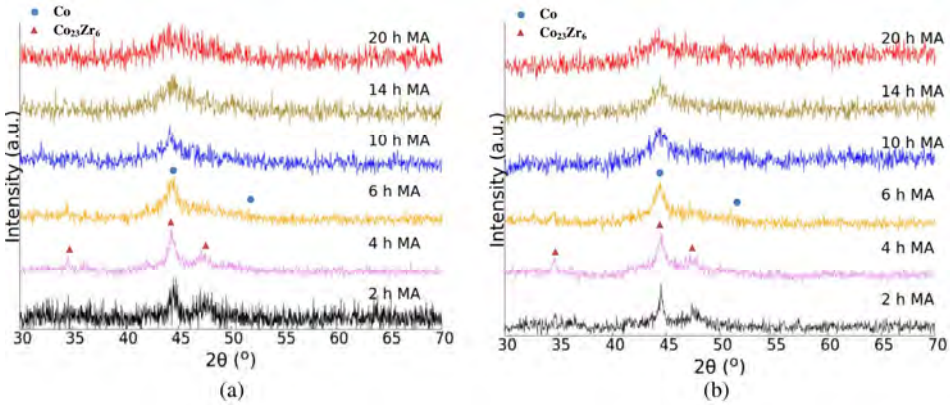

Figure 2. XRD patterns for the 2 to 20 h MA (a) $Co_{11}Zr_2$ and (b) $Co_{82}Zr_{12}$ powders

Two successive heat treatments were done on both samples: the samples were first annealed at 1030 °C for 7 days and slowly cooled to room temperature (TT), secondly a part of the powder was re-annealed at the same temperature for 1 hour and quenched in water (TT+Q). The fully crystalized samples (Figure 3) are multiphase (a mixture between Co, $Co_{11}Zr_2$ and $Co_{23}Zr_6$ phases), with quenching having made little difference. However we must note that the $Co_{82}Zr_{12}$ sample seems to have a higher concentration of the Orthorhombic $Co_{11}Zr_2$ phase, alongside the rhombohedral structure.

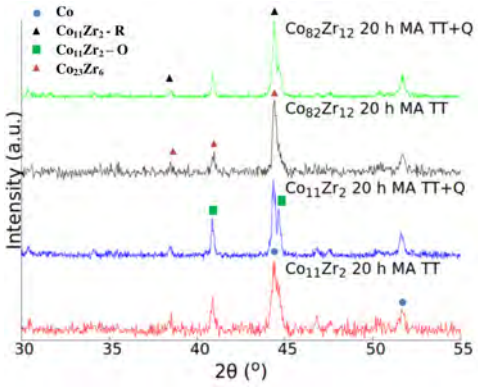

Figure 3. XRD patterns after annealing for the $Co_{11}Zr_2$ and $Co_{82}Zr_{12}$ compositions

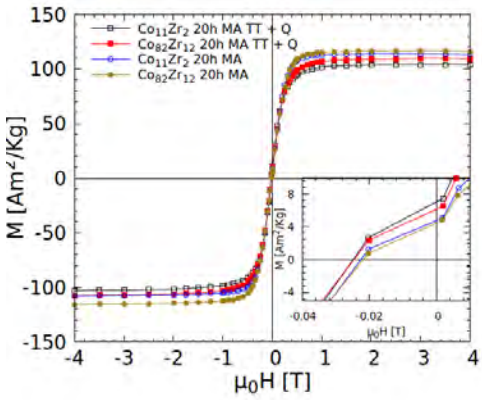

Figure 4. Demagnetization curves for the20 h MA and for annealed and quenched samples

Demagnetization curves, Figure 4, show little difference between the two compositions. The as-milled samples have very low remanence and coercivity (0.02 T). The annealing process improves these values by 25% and reduces saturation magnetization slightly, which leads us to conclude that by annealing the magnetic structure of the samples is hardened.

CONCLUSIONS

Mechanical alloying was investigated as a synthesis route for magnetic Co-Zr alloys, with potential applications as rare earth free permanent magnet materials. Even though the alloying process was effective, as determined via DSC and XRD measurements, the final alloys showed little coercivity and remanent magnetization, even after annealing.

ACKNOWLEDGMENTS

This work was supported by the Romanian Ministry of Research and Innovation, Grant No PN-III-P1.2PCCDI-2017-0871

REFERENCES

1. J. M. D. Coey, *IEEE Trans. Magn.,* 47, 4671 (2011)
2. M D Kuz'min, K P Skokov, H Jian, I Radulov, O Gutfleisc *J. Phys.: Condens. Matter,* 26, 064205 (5pp) (2014)
3. S. Manjura Hoque, S.K. Makineni, A. Pal, P. Ayyub, K. Chattopadhyay, *J. Alloy. Compd.,* 620, 442 (2015)
4. W.Y. Zhang, X.Z. Li, S. Valloppilly, R. Skomski, D.J. Sellmyer, *Mat. Sci. Eng. B,* 186, 64 (2014)

5. G.V. Ivanova, N.N. Shchegoleva, A.M. Gabay, *J. Alloy. Compd.,* 432, 135 (2007)
6. X.-Z. Li, W.Y. Zhang, D.J. Sellmyer, X. Zhao, M.C. Nguyen, C.Z. Wang, K.M. Ho*, J. Alloy. Compd*. 611, 167 (2014) B. Neelima, N.V. Rama Rao, V. Rangadhara Chary, S. Pandian, *J. Alloy. Compd*., 661, 72 (2016)
7. E. F. Kneller, R. Hawig*, IEEE Trans. Magn.*, 27, 3588 (1991)

STUDIA UBB PHYSICA, Vol. 63 (LXIII), 1-2, 2018, pp. 117-122
(RECOMMENDED CITATION)
doi:10.24193/subbphys.2018.11

SUPERCONDUCTIVITY IN LOW DIMENSIONAL SYSTEMS WITH DIFFERENT ENERGY DISPERSIONS

I. GROSU[1]

ABSTRACT. We analyzed the possibility for occurrence of superconductivity in low dimensional systems, taking into consideration a linear and a constant dispersion law for the electronic excitations. Using a mean field BCS-like model we calculate the zero temperature energy gap, the critical temperature, and the Gelikman-Kresin ratio. In the case of graphene with a linear dispersion the coupling strength should exceed a critical value. Taking realistic parameters it was shown that the occurrence of the superconducting state is not possible. We find out an opposite situation for a two-dimensional system with a constant dispersion.

Keywords: *Superconductivity, low dimensional systems, graphene, linear dispersion, constant dispersion.*

Superconductivity is a quantum phenomenon of the electron system that manifests at macroscopic scale. This phenomenon is due to an instability of the Fermi liquid state which leads to a new ground state of correlated paired electrons [1]. Here it was shown that this state is stabilized whenever there exist an attractive interaction between electrons. In a common metal such an attraction is always provided by the electron-phonon interaction. This behaviour however is strongly modified in the case of high-temperature

[1] *Babes-Bolyai University, Faculty of Physics, 1 Kogalniceanu str., 400084 Cluj-Napoca, Romania, e-mail: ioan.grosu@phys.ubbcluj.ro*

superconductors [2]. These are layered compounds with possible new pairing mechanism which leads to unconventional superconductivity. It was proposed that superconductivity emerges from antiferromagnetic spin fluctuations in a doped system and in the weak coupling [3, 4]. Other theoretical models proposed the non-Fermi character of these compounds [5]. Here, in contrast to classical Fermi liquid behaviour the superconducting state appear only if the coupling factor exceeds a critical value [6]. Other models consider the Bose-Einstein condensation phenomenon [7, 8]. More recent, after the discovery of graphene [9, 10], experiments on doped graphene reveal that graphene can be driven to the superconducting state [11]. A weak-coupling theory of superconductivity of Dirac electrons in graphene layers was proposed by Kopnin and Sonin [12]. On the other hand, experiments indicate the lack of superconductivity in undoped graphene, even an attractive electron-electron interaction λ could exist. The absence of superconductivity is rather due to the small density of states close to the Dirac point. In order to see this we adopt a simple mean-field model using a self-consistent equation for the order parameter Δ [13, 14]

$$\Delta = 4\lambda \int_0^{k_c} \frac{d^2k}{(2\pi)^2} \cdot \frac{\Delta}{E_k} \cdot \tanh\left(\frac{E_k}{2k_B T}\right) \tag{1}$$

The factor 4 comes from summation over the valley and band indices, k_c is cut-off momentum, $E_k = \sqrt{\varepsilon_k^2 + \Delta^2}$, k_B is the Boltzmann constant, and T the temperature. At the Dirac point $\varepsilon_k^2 = \hbar^2 v_F^2 k^2$, where v_F is the Fermi velocity. First we consider the $T = 0$ K case, when $\Delta \to \Delta_0$, and $\tanh(E_k / 2k_B T) \to 1$. We obtain

$$\Delta_0 = 4\lambda \int_0^{k_c} \frac{2\pi k dk}{(2\pi)^2} \cdot \frac{\Delta_0}{\sqrt{\hbar^2 v_F^2 k^2 + \Delta_0^2}} \tag{2}$$

or

$$1 = \frac{2\lambda}{\pi} \int_0^{k_c} \frac{dk \cdot k}{\sqrt{\hbar^2 v_F^2 k^2 + \Delta_0^2}} \tag{3}$$

Introducing a new variable $x = \hbar^2 v_F^2 k^2$, we get after integration

$$1 = \frac{2\lambda}{\pi\hbar^2 v_F^2}\left[\sqrt{\varepsilon_c^2 + \Delta_0^2} - \Delta_0\right] \qquad (4)$$

where $\varepsilon_c = \hbar v_F k_c$. Define the critical coupling λ_c through

$$\lambda_c = \frac{\pi\hbar^2 v_F^2}{2\varepsilon_c} \qquad (5)$$

and solving eq.(4) for Δ_0 one obtains

$$\Delta_0 = \varepsilon_c \cdot \frac{\lambda^2 - \lambda_c^2}{2\lambda\lambda_c} \qquad (6)$$

Since $\Delta_0 \geq 0$, one conclude that $\lambda \geq \lambda_c$.

In the opposite limit, when $T \to T_c$, T_c being the critical temperature, the order parameter $\Delta \to 0$. We will have

$$1 = 4\lambda \int_0^{k_c} \frac{d^2 k}{(2\pi)^2} \cdot \frac{1}{\varepsilon_k} \cdot \tanh\left(\frac{\varepsilon_k}{2k_B T_c}\right) \qquad (7)$$

or

$$1 = \frac{2\lambda}{\pi\hbar v_F} \int_0^{k_c} dk \cdot \tanh\left(\frac{\hbar v_F k}{2k_B T_c}\right) \qquad (8)$$

With the variable $y = \hbar v_F k / 2k_B T_c$, one obtains

$$1 = \frac{2\lambda}{\lambda_c} \cdot \frac{k_B T_c}{\varepsilon_c} \int_0^{\varepsilon_c / 2k_B T_c} dy \cdot \tanh(y) \qquad (9)$$

After evaluating the integral, and define $b = \varepsilon_c / 2k_B T_c$, we have

$$\frac{\lambda_c}{\lambda} \cdot b = \ln\left[\cosh(b)\right] \qquad (10)$$

Assuming $\varepsilon_c >> T_c$, ($b >> 1$), eq.(10) reduces to the approximate expression

$$\ln\left(\frac{1}{2}\right) \cong b \cdot \frac{\lambda - \lambda_c}{\lambda} \qquad (11)$$

From here we obtain the critical temperature

$$k_B T_c \cong \frac{\varepsilon_c}{2 \cdot \ln 2} \cdot \frac{\lambda - \lambda_c}{\lambda} \tag{12}$$

Again, in order to have a critical temperature λ should exceed λ_c. Finally, the Gelikman-Kresin ratio will be

$$\frac{2\Delta_0}{k_B T_c} \cong 2 \cdot \ln 2 \cdot \left(1 + \frac{\lambda}{\lambda_c}\right) \tag{13}$$

The results given by eqs.(6) and (12) should be carefully analyzed. In the case of pristine graphene, taking realistic parameters [14], one conclude that λ_c exceeds λ, and $\lambda_c \approx 20 \cdot \lambda$. In this case the superconducting phase is absent even in the presence of a finite electron-phonon coupling strength. This conclusion remains valid for the case of twisted graphene bilayer far away from the magic angle, when the two graphene layers are almost uncoupled. The situation changes if one consider the case of linear dispersion in the presence of doping (characterized by finite chemical potential μ). In this case it was shown [14] that the superconducting state exist, and the critical temperature is of order of $T_c \approx 10$ K.

In the following we will consider a model of a two-dimensional system, with spin and valley degeneration, and with a constant dispersion $\varepsilon_k^2 = \Delta_g^2$, in order to find out if the superconducting state exist. At $T = 0$ K the equation for the energy gap becomes

$$\Delta_0 = 4\lambda \int_0^{k_c} \frac{2\pi k dk}{(2\pi)^2} \cdot \frac{\Delta_0}{\sqrt{\Delta_g^2 + \Delta_0^2}} \tag{14}$$

with $k_c = \varepsilon_c / \hbar v_F$. Using eq.(5), the momentum cut-off will be $k_c = \pi \hbar v_F / 2\lambda_c$. The energy gap is given by

$$\Delta_0 = \sqrt{\left(\frac{\lambda}{\lambda_c} \cdot \frac{\varepsilon_c}{2}\right)^2 - \Delta_g^2} \tag{15}$$

which shows the possibility of occurrence of the superconducting state if $\Delta_g < \lambda \varepsilon_c / 2\lambda_c$. Assuming that $\lambda << \lambda_c$, one has $\Delta_g << \varepsilon_c$. The critical temperature is obtained from the equation

$$1 = 4\lambda \int_0^{k_c} \frac{2\pi k dk}{(2\pi)^2} \cdot \frac{1}{\Delta_g} \cdot \tanh\left(\frac{\Delta_g}{2k_B T_c}\right) \qquad (16)$$

Introducing the notation $a = 2\Delta_g \lambda_c / \varepsilon_c \lambda$, the critical temperature will be

$$k_B T_c = \frac{\Delta_g}{\ln\left(\frac{1+a}{1-a}\right)} \qquad (17)$$

with $a \leq 1$. With this notation eq.(15) can be rewritten as

$$\Delta_0 = \varepsilon_c \cdot \frac{\lambda}{2\lambda_c} \cdot \sqrt{1-a^2} \qquad (18)$$

The Gelikman-Kresin ratio, that measures the departure from the BCS (3.53) result [15, 16, 17], will be

$$\frac{2\Delta_0}{k_B T_c} = \frac{2}{a} \cdot \sqrt{1-a^2} \cdot \ln\left(\frac{1+a}{1-a}\right) \qquad (19)$$

Taking the following parameters: $\varepsilon_c \approx 200$ meV, $\lambda / \lambda_c \approx 1/20$, and $\Delta_g = 4$ meV, the energy-gap at zero temperature will be $\Delta_0 \cong 3$ meV, the critical temperature $T_c \approx 20$ K, and the Gelikman-Kresin ratio $2\Delta_0 / k_B T_c \cong 3.3$.

One can conclude that a BCS-mean field model with a weak attractive interaction, due to the electron-phonon coupling, can explain the occurrence of the superconducting state, in low dimensional systems, if a constant dispersion law is considered. Such a dispersion can occur in highly doped two dimensional systems.

REFERENCES

1. J.Bardeen, L.N.Cooper, J.R.Schrieffer, *Phys. Rev.,* 108, 1175 (1957)
2. J.G.Bednorz, K.A.Müller*, Z. Phys. B,* 64, 189 (1986)
3. P.Monthoux, A.Balatski, D.Pines, *Phys. Rev. B,* 46, 14803 (1992)
4. I.Grosu, M.Crisan, *Phys.Rev. B,* 49, 1269 (1994)
5. C.M.Varma, Z.Nussinov, W.von Saarloos, *Phys. Repts*., 361, 267 (2002)
6. I.Grosu, I.Tifrea, M.Crisan*, J. Supercond*., 11, 339 (1998)

7. S.Fujita, S.Godoy, "*Quantum Statistical Theory of Superconductivity*", Plenum Press, New York (1996)
8. M.Crisan, I.Tifrea, D.Bodea, I.Grosu, *Phys. Rev. B,* 72, 184414 (2005)
9. A.K.Geim, K.S.Novoselov, *Nature Mater*, 6, 183 (2007)
10. A.H.Castro Neto, F.Guinea, N.M.R.Peres, K.S.Novoselov, A.K.Geim, *Rev. Mod. Phys*., 81, 109 (2009)
11. B.M.Ludbrook et al., *PNAS* 112, 11795 (2015)
12. N.B.Kopnin, E.B.Sonin, *Phys.Rev.Lett*., 100, 246808 (2008)
13. A.L.Fetter, J.D.Walecka, "*Quantum Theory of Many-Particle Systems*", McGraw-Hill, New York (1971)
14. T.J.Peltonen, R.Ojajärvi, T.T.Heikkilä, *arXiv*: 1805.01039
15. B.Krunavakarn, P.Udomsamuthirun, S.Yoksan, I.Grosu, M.Crisan, *J.Supercond*., 11, 271 (1998)
16. P.B.Allen, B.Mitrovic, "*Solid State Physics*", edited by H.Ehrenreich, F.Seitz, D.Turnbull, Academic, New York (1982)
17. D.C.Mattis, M.Molina, *Phys. Rev. B,* 44, 12565 (1991)

STUDIA UBB PHYSICA, Vol. 63 (LXIII), 1-2, 2018, pp. 123-126
(RECOMMENDED CITATION)
doi:10.24193/subbphys.2018.12

ON THE ABSENCE OF SUPERCONDUCTIVITY IN GAPPED GRAPHENE SYSTEMS

I. GROSU[1]

ABSTRACT. We analyzed the possibility of the superconducting state in the case of gapped graphene systems. For the electron excitations we consider the case of massive gapped spectrum and the case of massless gapped spectrum. Using realistic parameters we showed that the superconducting state is absent.

Keywords: *Superconductivity, Graphene, Massive gapped spectrum, Massless gapped spectrum.*

Graphene is the first two dimensional crystal observed in nature that possesses remarkable physical properties [1]. Due to its band structure graphene is a zero density of states semimetal at the Fermi energy. The low energy excitations are characterized by linear dispersion of the quasiparticles in the vicinity of the Fermi points. Pristine graphene is less useful for practical applications because of its low carrier density and zero band gap. On the other hand, many electronic applications require the presence of an energy gap between the bands. Several experimental measurements [2, 3] reveal the presence of an energy gap Δ_g in the quasiparticle spectrum of graphene. The nature of the gap was attributed to the effect of the substrate. The gapped energy spectrum (massive gapped spectrum) was considered in order to

[1] *Babes-Bolyai University, Faculty of Physics, 1 Kogalniceanu str., 400084 Cluj-Napoca, Romania, e-mail: ioan.grosu@phys.ubbcluj.ro*

analyze the thermoelectric power in graphene [4], and the phenomenological massless gapped spectrum [5] was introduced to reconcile the gapped nature of the energy spectrum with several spectroscopic measurements. Other physical properties of gapped graphene systems were analyzed in Refs.[6, 7]. The presence of the gap Δ_g changes the electronic density of states and affect many of the physical properties of graphene. Recent experiments reveal that a doped bilayer graphene twisted around a certain angle becomes superconducting [8]. A weak-coupling theory of superconductivity for electrons in graphene was proposed in Ref.[9] and extended in Ref.[10]. Here was shown that the superconducting state, for Dirac electrons, occur if the attractive electron-electron interaction λ exceeds a critical value λ_c. Unfortunately, taking realistic parameters, $\lambda_c \cong 20 \cdot \lambda$, which shows that pristine graphene cannot reach the superconducting state. An opposite behaviour is obtained in the case of doped graphene where the superconducting state occur, and the superconducting parameters (superconducting energy-gap, critical temperature, Gelikman-Kresin ratio, etc.) [10-13] can be calculated.

In this paper we will analyze the possibility of the superconducting state in gapped graphene systems for both, the massive and the massless gapped spectrum. We will adopt the mean-field scenario where the superconducting gap equation has the self-consistent form [10]

$$\Delta = 4\lambda \int_0^{k_c} \frac{d^2k}{(2\pi)^2} \cdot \frac{\Delta}{E_k} \cdot \tanh\left(\frac{E_k}{2k_BT}\right) \tag{1}$$

Δ- is the superconducting energy gap, λ- the electron-electron coupling factor, T- the temperature, and k_c- the cut-off momentum. Here

$$E_k = \sqrt{\varepsilon_k^2 + \Delta^2} \tag{2}$$

For the case of massive gapped system one has

$$\varepsilon_k = \pm\sqrt{\hbar^2 v_F^2 k^2 + \Delta_g^2} \tag{3}$$

with v_F - the Fermi velocity. The zero temperature superconducting energy gap ($\Delta \to \Delta_0$, for $T \to 0$), will be calculated using eq.(1) with $\tanh(E_k / 2k_BT) \to 0$. We obtain

$$1 = \frac{2\lambda}{\pi}\int_0^{k_c} \frac{dk \cdot k}{\sqrt{\hbar^2 v_F^2 k^2 + \Delta_g^2 + \Delta_0^2}} \tag{4}$$

Introducing: $x = \hbar^2 v_F^2 k^2$, and evaluating the integral, we have

$$\frac{\pi\hbar^2 v_F^2}{2\lambda} = \sqrt{\varepsilon_c^2 + \Delta_g^2 + \Delta_0^2} - \sqrt{\Delta_g^2 + \Delta_0^2} \tag{5}$$

Here: $\varepsilon_c = \hbar v_F k_c$. We define now $\lambda_c = \pi\hbar^2 v_F^2 / 2\varepsilon_c$ - the critical coupling. The equation for the superconducting gap Δ_0 will be

$$\sqrt{\Delta_g^2 + \Delta_0^2} = \varepsilon_c \cdot \frac{\lambda^2 - \lambda_c^2}{2\lambda\lambda_c} \tag{6}$$

For realistic parameters of graphene it was shown [10] that $\lambda_c \approx 20 \cdot \lambda$. One conclude, using eq.(6), that the superconducting state for graphene with massive gapped spectrum is not possible.

For the case of massless gapped spectrum

$$\varepsilon_k = \pm\left(\hbar v_F k + \Delta_g\right) \tag{7}$$

and using eq.(1), the zero temperature superconducting energy gap equation will be

$$1 = \frac{2\lambda}{\pi}\int_0^{k_c} \frac{dk \cdot k}{\sqrt{\left(\hbar v_F k + \Delta_g\right)^2 + \Delta_0^2}} \tag{8}$$

With the new variable: $y = \hbar v_F k + \Delta_g$, splitting the integral above in two contributions, and after evaluating the integrals, we obtain

$$\varepsilon_c \cdot \frac{\lambda_c}{\lambda} = \sqrt{\left(\varepsilon_c + \Delta_g\right)^2 + \Delta_0^2} - \sqrt{\Delta_g^2 + \Delta_0^2} - \Delta_g \cdot \ln\left(\frac{\varepsilon_c + \Delta_g + \sqrt{\left(\varepsilon_c + \Delta_g\right)^2 + \Delta_0^2}}{\Delta_g + \sqrt{\Delta_g^2 + \Delta_0^2}}\right) \tag{9}$$

Due to the large value of the ratio λ_c / λ one can observe that the right hand side of eq.(9) cannot reach the value given by the left hand side. To give a more transparent result we will consider the following case: $\varepsilon_c, \Delta_g >> \Delta_0$. In this case one can expand the right hand side in Δ_0 to obtain

$$\varepsilon_c\left(\frac{\lambda_c}{\lambda}-1\right)+\Delta_g\cdot\ln\left(1+\frac{\varepsilon_c}{\Delta_g}\right)\cong-\frac{\Delta_0^2}{4\Delta_g}\left(\frac{\varepsilon_c}{\varepsilon_c+\Delta_g}\right)^2 \tag{10}$$

Due to the fact that: $\lambda_c>\lambda$, $\Delta_g>0$, $\varepsilon_c>0$, one can observe that the superconducting state is not possible nor in the case of massless gapped spectrum.

Our simple model show the absence of superconductivity in the case of graphene, in both the massive and the massless gapped spectrum models, even an attractive electron-electron interaction is present.

REFERENCES

1. A.H.Castro Neto, F.Guinea, N.M.R.Peres, K.Novoselov, A.K.Geim, *Rev.Mod.Phys.* 81, 109 (2009)
2. S.Y.Zhou et.al., *Nature Mater.* 6, 770, (2007); *Nature Mater.,* 7, 259 (2008);
3. G.Li, A.Luican, E.Y.Andrei, *Phys.Rev.Lett.,* 102, 176804 (2009)
4. S.G.Sharapov, A.A.Varlamov, *Phys.Rev.B,* 86, 035430 (2012)
5. L.Benfatto, E.Cappelutti, *Phys.Rev.B,* 78, 115434 (2008)
6. M.Crisan, I.Grosu, I.Tifrea, *Eur.Phys.J.B,* 89, 140 (2016)
7. I.Grosu, T.L.Biter, *Physica E,* 86, 154 (2017)
8. B.M.Ludbrook et.al., *PNAS* 112, 11795 (2015)
9. N.B.Kopnin, E.B.Sonin, *Phys.Rev.Lett.,* 100, 246808 (2008)
10. T.J.Peltonen, R.Ojajärvi, T.T.Heikkilä, *arXiv:* 1805.01039
11. P.B.Allen, B.Mitrovic, "*Solid State Physics"* edited by H.Ehrenreich, F.Seitz, D.Turnbull, Academic, New York (1982)
12. B.Krunavakarn, P.Udomsamuthirun, S.Yoksan, I.Grosu, M.Crisan, *J.Supercond*., 11, 271 (1998)
13. D.C.Mattis, M.Molina, *Phys.Rev.B,* 44, 12565 (1991)

STUDIA UBB PHYSICA, Vol. 63 (LXIII), 1-2, 2018, pp. 127-132
(RECOMMENDED CITATION)
doi:10.24193/subbphys.2018.13

RENORMALIZATION FUNCTION FOR THE ELECTRON-FLEXURAL PHONON INTERACTION

I. GROSU[1]

ABSTRACT. The renormalization function for the electron-phonon interaction is discussed. The system is considered as two-dimensional, and we consider the case of flexural phonons. The flexural phonons have a dispersion which is linear for wave-vectors less than a critical value q_c, and quadratic for $q > q_c$. The renormalization function differs from the standard expression, and leads to modifications of the normal and superconducting properties of materials.

Keywords: *Renormalization function, two-dimensional systems, flexural phonons.*

The electron-phonon interaction is one of the fundamental interactions in condensed matter, and plays, together with the Coulomb interaction, an important role in many physical phenomena. The electronic excitations in a solid are strongly modified due to the Coulomb interaction and to the coupling to the lattice vibrations. These modifications affect the transport and thermodynamic properties of a solid. The electron-phonon interaction plays also a fundamental role in the attractive electron-electron interaction which is the origin of the electron pairing mechanism of the phenomenon of superconductivity [1]. Here the transition temperature T_c is determined by the material dependent quantities, λ - the coupling factor, and μ^* - the Coulomb pseudopotential

[1] *Babes-Bolyai University, Faculty of Physics, 1 Kogalniceanu str., 400084 Cluj-Napoca, Romania, e-mail: ioan.grosu@phys.ubbcluj.ro*

$$T_c \cong \langle\omega\rangle \exp\left\{-\frac{1}{\lambda-\mu^*}\right\} \tag{1}$$

In this model, the adiabatic approximation for the dynamics of electrons and phonons is used. This situation correspond to the validity of the Migdal's theorem [2], because the ratio between the Debye energy ω_D, and the Fermi energy E_F is very small. This is the case of many common metals. However, in high-temperature superconductors, including the fullerene compounds, the Fermi energy is small ($E_F \approx 0.1$ eV) and is of order of the Debye energy. This situation implies a breakdown of Migdal's theorem [3]. More recent the validity of the Migdal's theorem in graphene and Weyl semimetals is analyzed in Ref.[4]. If other excitations (e.g. antiferromagnetic magnons) mediate the electron-electron attractive interaction, the Migdal's theorem seems to be also valid [5].

Here we will analyze the electron-phonon interaction, calculating the standard self-energy to the first order, and the wave-function renormalization term Z [6,7]. The self-energy is given by

$$\Sigma(i\omega_n) = -Tg^2 \sum_{k_s} \sum_{q} \sum_{s} G_0(i\omega_s, \varepsilon_{k_s}) D_0(i\omega_n - i\omega_s, \omega_q) \tag{2}$$

Here: T - is the temperature, g - the electron-phonon coupling strength, G_0 - the usual Green's function in the Matsubara representation

$$G_0(i\omega_s, \varepsilon_{k_s}) = \frac{1}{i\omega_s - \varepsilon_{k_s}} \quad ; \quad \omega_s = 2\pi T\left(s+\frac{1}{2}\right) \tag{3}$$

and D_0 - the Green's function for phonons

$$D_0(i\omega_m, \omega_q) = \frac{-\omega_q^2}{\omega_m^2 + \omega_q^2} \quad ; \quad \omega_m = 2\pi T m \tag{4}$$

For the sum over k_s we use the simplification

$$\sum_{k_s} \to N(0) \int_{-E/2}^{E/2} d\varepsilon \tag{5}$$

where we assumed a constant density of states in the band between $-E/2$ and $E/2$. Using eqs.(3-5) we obtain

$$\Sigma(i\omega_n) = -2iT\lambda \sum_q \sum_s \arctan\left(\frac{E}{2\omega_s}\right) \cdot \frac{\omega_q^2}{(\omega_n - \omega_s)^2 + \omega_q^2} \tag{6}$$

or

$$\Sigma(i\omega_n) = -i\omega_n \lambda T \sum_q \sum_{s>0} \arctan\left(\frac{E}{2\omega_s}\right) \cdot \frac{8\omega_q^2 \omega_s}{[(\omega_s - \omega_n)^2 + \omega_q^2][(\omega_s + \omega_n)^2 + \omega_q^2]} \tag{7}$$

Here we introduced the coupling factor $\lambda = g^2 N(0)$. The wave-function remormalization is given by

$$Z(i\omega_n) = 1 - \frac{1}{i\omega_n}\Sigma(i\omega_n) \tag{8}$$

In the following we will consider the static case ($\omega_n = 0$), and we neglect the temperature dependence ($T \to 0$), when we replace

$$T\sum_{s>0} \to \frac{1}{2\pi}\int_0^\infty d\omega \tag{9}$$

We will have

$$Z = 1 + \frac{\lambda}{2\pi}\sum_q \int_0^\infty d\omega \cdot \arctan\left(\frac{E}{2\omega}\right) \cdot \frac{8\omega_q^2 \omega}{\left(\omega^2 + \omega_q^2\right)^2} \tag{10}$$

Now we use the notation: $a = 2\omega_q / E$, and change the variable: $\omega / \omega_q = x$. We obtain

$$Z = 1 + \frac{4\lambda}{\pi}\sum_q \int_0^\infty dx \cdot \arctan\left(\frac{1}{a \cdot x}\right) \cdot \frac{x}{\left(x^2 + 1\right)^2} \tag{11}$$

The integral is easy evaluated and gives: $\pi/[4(1+a)]$. The renormalization function will be

$$Z = 1 + \frac{\lambda E}{2}\sum_q \frac{1}{\omega_q + \frac{E}{2}} \tag{12}$$

In order to find out an analytical form of the renormalization function we will consider a two-dimensional system, and consider the dispersion ω_q that correspond to flexural phonons [8, 9]:

$$\omega_q = \sqrt{\frac{\gamma q^2 + \kappa q^4}{\rho}} \tag{13}$$

Here: γ - is the sample specific coefficient induced by the external strain, κ - is the bending stiffness, and ρ - the mass density. This expression can be approximated as

$$\omega_q \cong q_c \alpha_0 q \tag{14}$$

for $q < q_c$, and

$$\omega_q \cong \alpha_0 q^2 \tag{15}$$

for $q > q_c$, with: $q_c = \sqrt{\gamma / \kappa}$ and : $\alpha_0 = \sqrt{\kappa / \rho}$. The sum over q wave-vectors is evaluated using

$$\sum_q \to \frac{A}{(2\pi)^2} \cdot B \cdot \int d^2 q \tag{16}$$

where we consider the unit area for A, and $B = 3\sqrt{3}/2$ for the case of honeycomb lattice. We split the wave-vector integral in two contributions, accoring to eqs.(14, 15). After evaluating these integrals one obtains

$$Z = 1 + \frac{3\sqrt{3}}{4\pi} \cdot \frac{\lambda q_c^2}{r} \cdot \left\{ 1 - \frac{1}{r} \cdot \ln(1+r) + \frac{1}{2} \cdot \ln\left[\frac{1 + r(q_M / q_c)^2}{1+r} \right] \right\} \tag{17}$$

where: $r = 2\alpha_0 q_c^2 / E$, and q_M is a wave-vector cut-off. In the wide-band approximation (E - large), the renormalization function becomes

$$Z \cong 1 + \frac{3\sqrt{3}}{8\pi} \cdot \lambda \cdot q_M^2 \tag{18}$$

This result differs from the standard expression $Z = 1 + \lambda$, and leads to modifications of many physical properties of solids, due to modifications of density of states and of the coupling g [10-14]. The magnitude of modifications can be estimated if we restore the dimensions by replacing

q_M with $a q_M$ in eq.(18) (a - the lattice constant), and taking $q_M \ 1/a$. One obtains $Z \approx 1+0.2\lambda$, a result which reveal the smallness of the correction factor. The renormalization function Z can also be evaluated for other bosonic excitations that are important for various properties of solids, as magnetic excitations [15-17], and even for the case of non-Fermi systems [18-21]. Here we obtained a simple result which can be used, as a starting point, in future investigations, in order to find out the modifications of the normal and superconducting properties of newly discovered materials. A more realistic result, for the case of graphene, can be obtained taking an energy dependent density of states, instead of simplification used in eq.(5).

REFERENCES

1. J.Bardeen, L.N.Cooper, J.R.Schrieffer, *Phys.Rev.,* 108, 1175 (1957)
2. A.B.Migdal, *Sov.Phys.JETP* 34, 996 (1958)
3. L.Pietronero, S.Strassler, C.Grimaldi, *Phys.Rev.B,* 52, 10516 (1995)
4. B.Roy, J.D.Sau, S.Das Sarma, *Phys.Rev B,* 89, 165119 (2014)
5. I.Grosu, M.Crisan, *Phys.Rev.B,* 49, 1269 (1994)
6. G.M.Eliashberg, *Sov.Phys.JETP,* 11, 696 (1960)
7. P.B.Allen, B.Mitrovic, *Solid State Physics,* edited by H.Ehrenreich, F.Seitz, D. Turnbull, Academic, New York (1982)
8. M.V.Fischetti, W.G.Vandenberghe, *Phys.Rev.B,* 93, 155413 (2016)
9. E.Mariani, F.von Oppen, *Phys.Rev.Lett*., 100, 076801 (2008)
10. A.V.Chubukov, D.L.Maslov, *Phys.Rev.B,* 68, 155113 (2003)
11. I.Grosu, T.Veres, M.Crisan, *Phys.Rev.B,* 50, 9404 (1994)
12. D.C.Mattis, M.Molina, *Phys.Rev.B,* 44, 12565 (1991)
13. B.Krunavakarn, P.Udomsamuthirun, S.Yoksan, I.Grosu, M.Crisan, *J.Supercond.,* 11, 271 (1998)
14. J.P.Carbotte, *Rev.Mod.Phys.,* 62, 1027 (1990)
15. A.J.Millis, H.Monien, D.Pines, *Phys.Rev.B,* 42, 167 (1990)
16. M.Crisan, I.Tifrea, D.Bodea, I.Grosu, *Phys.Rev.B,* 72*,* 184414 (2005)
17. N.F.Berk, J.R.Schrieffer, *Phys.Rev.Lett*., 17, 433 (1966)

18. P.W.Anderson, *Science,* 235, 1196 (1987)
19. S.Chakravarty, P.W.Anderson, *Phys.Rev.Lett.,* 72, 3859 (1994)
20. V.N.Muthukumar, D.Sa, M.Sardar, *Phys.Rev.B,* 52, 9647 (1995)
21. I.Grosu, I.Tifrea, M.Crisan, *J.Supercond*., 11, 339 (1998)

STUDIA UBB PHYSICA, Vol. 63 (LXIII), 1-2, 2018, pp. 133-142
(RECOMMENDED CITATION)
doi:10.24193/subbphys.2018.14

STUDY OF STRUCTURAL, MORPHOLOGICAL AND ELECTRICAL PROPERTIES IN THE $(Bi_{1.6}Pb_{0.4})(Sr_{1.8}Ba_{0.2})Ca_2(Cu_{1-x}Gd_x)_3O_y$ SUPERCONDUCTORS

C. LUNG[1,*], D. MARCONI[1,2] AND A. POP[1]

ABSTRACT. X-ray powder diffraction (XRD), scanning electron microscopy (SEM) and electrical resistivity measurements are performed to investigate some physical properties of $(Bi_{1.6}Pb_{0.4})(Sr_{1.8}Ba_{0.2})Ca_2(Cu_{1-x}Gd_x)_3O_y$ superconducting samples fabricated at sintering temperatures of 840 ^{0}C and 845 ^{0}C and the uniaxial pressures of 196MPa and 392MPa respectively. The samples were prepared by standard solid-state reaction methods. XRD measurements show that the samples obtained at 840 °C contain two phases. With the increase of the sintering temperature at 845 ^{0}C, a decrease in the diffraction peaks of the phase 2212 is observed, and with the increase of the pressure at 392MPa this phase falls below 10%. SEM analysis show that the superconductors have a uniform surface, but the size of the granules changes so that the sample sintered at 845 °C and the uniaxial pressure of 392 MPa has the best crystallinity.

Keywords: *BiPb 2223 doped superconductors, XRD, SEM, electrical properties*

[1] *Babes-Bolyai University, Physics Faculty, M. Kogalniceanu No.1, 400084, Cluj-Napoca, Romania*

[2] *Department of Molecular and Biomolecular Physics, National Institute for Research and Development of Isotopic and Molecular Technologies, Cluj-Napoca, Romania*

[*] *Corresponding author: claudiu.lung@phys.ubbcluj.ro*

1. INTRODUCTION

Since the discovery of the high-temperature ceramic superconductors; numerous researches have been carried out to characterize properties of the materials [1–14]. It is well-known that a CuO-based superconductor, in general, behaves like a Mott–Hubbard insulator at low carrier concentrations, like a superconductor with semiconducting normal state resistivity behavior at intermediate carrier concentrations and like a superconductor with a typical metallic normal state resistivity behavior at sufficiently high carrier concentrations. Gadolinium substitution in BSCCO (2212) system for various doping levels [15] showed that the density of states at the Fermi level was reduced with increasing gadolinium ion contents at calcium sites.

In this work, investigations were carried out to determine the structural and transport properties for Gd doped BSCCO samples fabricated at sintering temperatures of 840 ^{0}C and 845^{0}C and the uniaxial pressures used were 196MPa and 392MPa. In addition, X-ray diffraction (XRD) and scanning electron microscopy (SEM) measurements were performed to investigate the phase analysis and surface morphology of the samples considered.

2. EXPERIMENTAL

Policrystalline bulk samples with nominal composition $(Bi_{1.6}Pb_{0.4})(Sr_{1.8}Ba_{0.2})Ca_2(Cu_{1-x}Gd_x)_3O_y$ were prepared by the conventional solid-state reaction of appropriate amounts of the metal oxides and carbonates of 99.99% purity [16–18]. Two sets of samples were fabricated at sintering temperatures of 840 ^{0}C and 845^{0}C and samples were pressed in the form of pills with a diameter of 7 mm using a hydraulic press. The uniaxial pressures used were 196MPa and 392MPa. The calcination was carried out at 800 °C for 30 hours. Table 1 gives the composition and sintering temperatures for the two systems. The temperature dependence of electrical resistivity was

measured using standard four probe method. The sample was cooled down in the absence of magnetic field; excitation current was applied to the sample plane perpendicular to the pressing direction (in the (ab) plane).

Table 1. Composition and fabrication conditions for BSCCO compounds

Sample	**Sintering temperature**	**Uniaxial pressure**
$(Bi_{1.6}Pb_{0.4})(Sr_{1.8}Ba_{0.2})Ca_2(Cu_{1-x}Gd_x)_3O_y$	840 ^{0}C	196MPa
$(Bi_{1.6}Pb_{0.4})(Sr_{1.8}Ba_{0.2})Ca_2(Cu_{1-x}Gd_x)_3O_y$		392MPa
$(Bi_{1.6}Pb_{0.4})(Sr_{1.8}Ba_{0.2})Ca_2(Cu_{1-x}Gd_x)_3O_y$	845 ^{0}C	196MPa
$(Bi_{1.6}Pb_{0.4})(Sr_{1.8}Ba_{0.2})Ca_2(Cu_{1-x}Gd_x)_3O_y$		392MPa

3. RESULTS AND DISCUSSION

The samples of $(Bi_{1.6}Pb_{0.4})(Sr_{1.8}Ba_{0.2})Ca_2(Cu_{1-x}Gd_x)_3O_y$ were placed on the X-ray diffractometer support. The X-rays interact with electrons in atoms, causing elastic or inelastic collisions. X-Ray elastic spreading contains data on the electron distribution in the material, the method used to determine the crystalline structure. Determination of the size of crystallites was performed using the Debye-Scherer relationship for diameter:

$$\boldsymbol{D = \frac{0.9\lambda}{B cos\theta}}$$

where B represents the width of the half-maximum for different peaks in the diffractogram. The assessed values for crystallite size are shown in Table 3.

By measuring angles and intensities of X-ray diffraction, a 3D image of the electrons in the crystal will be obtained. From the density of the electrons measured, the position of the atoms in the crystal is obtained, as well as information about their order / disorder.

Powder X-ray diffraction measurements aim to study the influence of sintering temperature and axial pressure on the structure and composition of the phase of the samples. The sintering temperature was 840 °C, 845 °C and axial pressures of 196MPa and 392MPa (Figure 1).

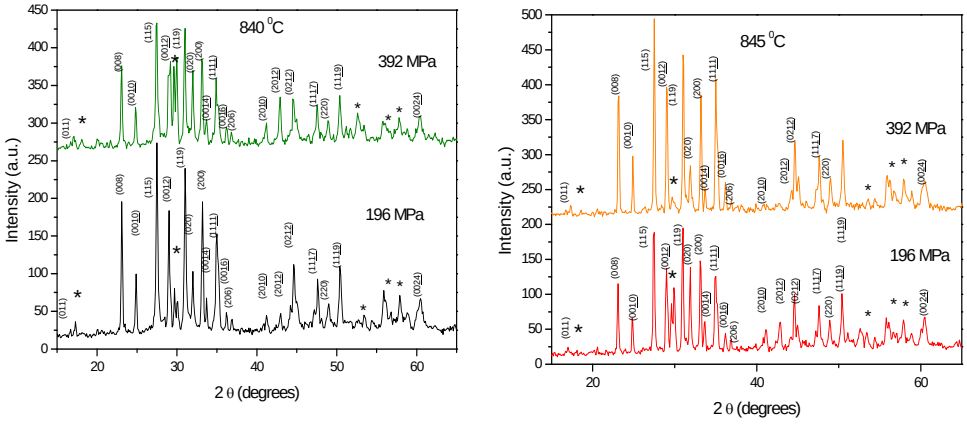

Figure 1. XRD diffractograms for sample sintered at la 840°C and 845°C

Also from the XRD analysis we calculate the presence of Bi: 2212 phase, with a relatively small percentage for both axial pressures, which can be seen from Table 2.

Table 2. Phase percentage calculated from XRD measurements.

		2223 %	2212 %
196MPa	840° C	80.8	19.2
	845° C	85.7	14.3
392 MPa	840° C	84.2	15.8
	845° C	90.4	9.6

Phase percentages were calculated using the formulas:

$$\mathrm{Bi}:2223(\%)=\frac{\sum I[\mathrm{Bi}:2223]}{q}\times 100$$

$$\mathrm{Bi}:2212(\%)=\frac{\sum I[\mathrm{Bi}:2212]}{q}\times 100$$

,

were q= $\Sigma I[Bi{:}\,2223]+\Sigma I[Bi{:}\,2212]$ and I is the intensity of the present phases.

The analysis of the crystalline structure of the $(Bi_{1.6}Pb_{0.4})$ $(Sr_{1.8}Ba_{0.2})$ Ca_2 $(Cu_{1-x}Gd_x)_3O_y$ compound was performed using a high resolution Brucker D8 diffractometer with a Bragg-Brentano configuration, copper anode with λ = 0.15406 nm; θ-20 range was 10 - 90, 0.1 step and time of 5s / step.

3.1 Variation of sintering temperature and uniaxial pressure

Starting from previous studies [19] showing that by increasing the sintering temperature samples with good intergranular coupling were obtained, we varied the sintering temperature in the range around 845 ^{0}C, for which the samples had high critical current densities. To study the effect of thermal treatments and uniaxial pressures on critical current density we varied in two different ways. When we varied the temperature between 840 ^{0}C and 845 ^{0}C, we kept the pressure of sample constant, and when we kept the constant sintering temperature we varied the pressure of sample between 196 and 392 MPa. The first temperature of the heat treatment applied to the samples - calcination was 840 ^{o}C for 9 days and the second to 845 ^{o}C, which is shown in Figure 2.

To have the desired effect the application of the uniaxial pressure is indicated is indicated to have high values. For this reason, we applied 196 and 392 MPa which leads to a good compaction of the sample and the atomic diffusion becomes approximately uniform.

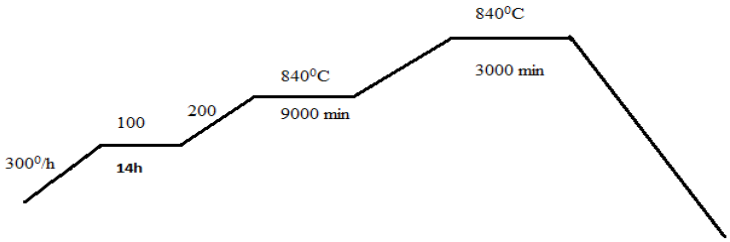

Figure 2. Schematic representation of heat treatment

The temperature dependence of the electrical resistivity was measured using the standard four-probe method. The sample was cooled in the absence of the magnetic field; an excitation current was applied to the sample in the plane, perpendicular to the direction of pressing (in plane (ab)). The voltage in the sample was measured as the temperature dropped to 60K.

Figure 3 shows the dependence of the temperature resistivity for the two Bi: 2223 samples at 196MPa or 392MPa respectively. Resistance behavior is a predictable transition from normal to superconducting conditions below 110K. The critical temperature of the samples was obtained from the temperature-dependent resistor I-derived derivative.

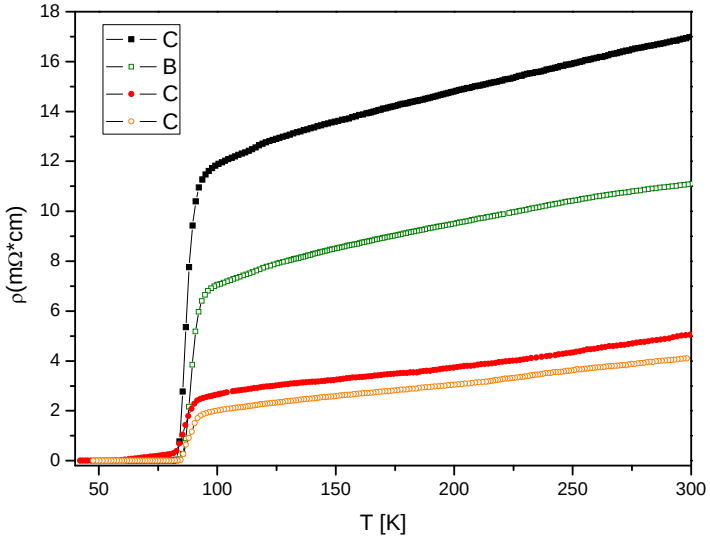

Figure 3. Resistivity dependence vs. temperature

The curves show a "metallic" behavior in the temperature region corresponding to the normal state indicating that the electric current flow occurs in the plane ab.

Table 3. Parameters obtained from data of x-ray diffraction and electrical measurements

Sample	Tc (K)	ρ at 300 k (mΩ* cm)	Epsilon * 10^{-3}	(D) (nm)
196 Mpa, 840 ^{0}C	95.2	16.91	9.06	22.9
392 Mpa, 840^{0}C	98.1	11.09	7.83	31.5
845 196 Mpa,^{0}C	96.7	5.05	4.94	38.6
845 392 Mpa,^{0}C	99.2	4.13	3.29	101.4

Study of electrical resistance depending on temperature shows that by increasing the pressure of the uniaxial tensile strength decreases (Table 3) due to betterment of electrical contacts between granules and their orientation perpendicular to the direction of applying the pressure and temperature of growth.

3.2 SEM measurements

Following the SEM analysis, it is observed that the superconductors have a uniform surface, but the size of the granules is changed, so that their size increases by decreasing the degree of crystallization. It can also be seen a change in the shape of the crystallites, as the distance decreases. Temperature has an important role because its growth leads to an increase in the size of the crystallites, which leads to an improvement of the superconducting conductivity, according to the results obtained in the literature, Figure 4.

840 ^{0}C, 192 MPa

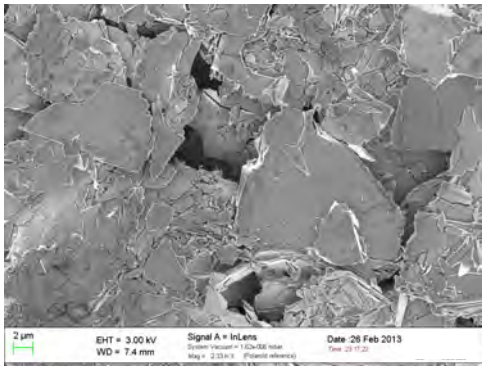

840 ^{0}C, 392 MPa

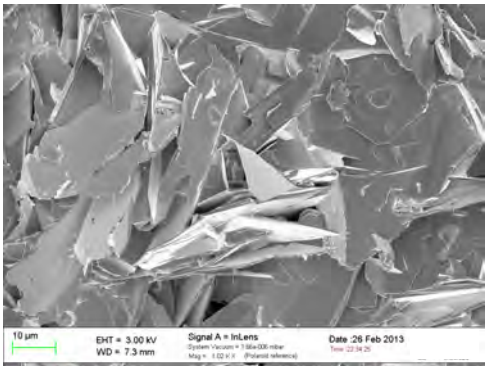

845 ^{0}C, 192 MPa

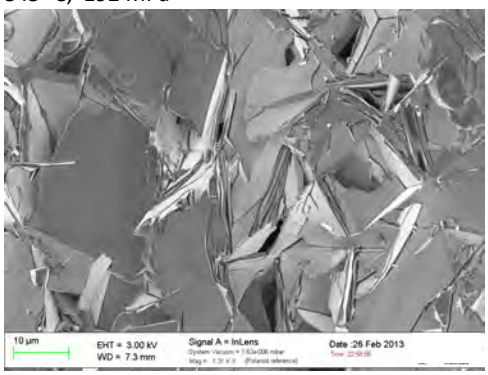

845 ^{0}C, 392 MPa

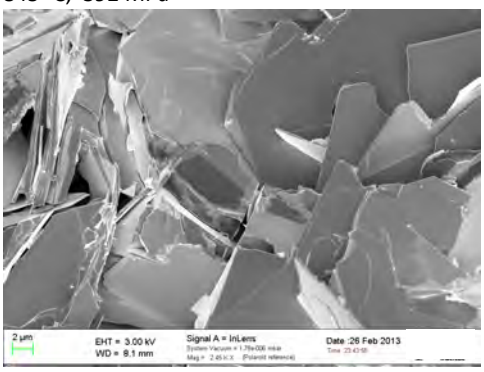

Figure 4. SEM images for the sample sintered at 840 ^{o}C and 845 ^{o}C using uniaxial pressure of 196 Mpa and 392 Mpa

The stoichiometry of the obtained samples (Figure 5) was assessed from the EDX measurements using the ZAF approximation.

Using this correction the atomic percentage of the elements was normalized by the percentage of Cu = 3 and the stoichiometry obtained for all samples was Bi: Pb: Sr: Ba: Ca: Cu: Gd = 1.65: 0.35: 1.85: 0.25: 1.57: 2.88: 0.12.

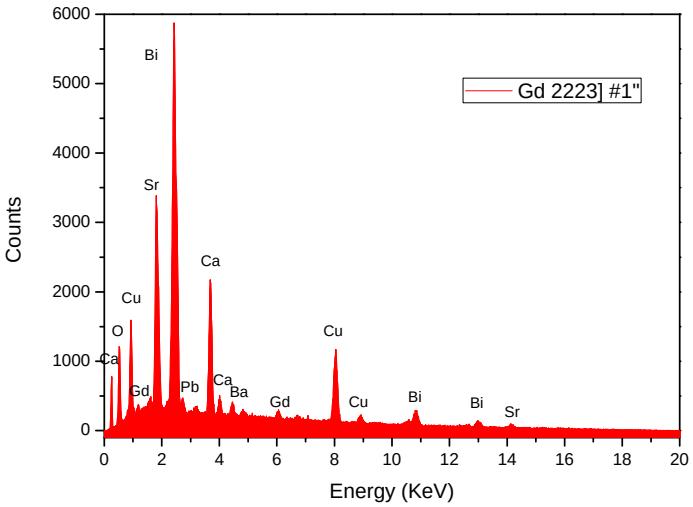

Figure 5. The stoichiometry obtained from EDX

4. CONCLUSION

Following experimental investigations to synthesize and characterize the structural and electrical properties of the compound **$(Bi_{1.6}Pb_{0.4})(Sr_{1.8}Ba_{0.2})Ca_2(Cu_{1-x}Gd_x)_3O_y$** when we modified the sintering temperature from 840 ^{0}C to 845 ^{0}C and we applied a uniaxial pressure of 196MPa and 392MPa respectively, we reached the following conclusions: the samples obtained at 840 °C contain two phases: Bi: 2223 - the major phase and Bi: 2212-minority phase. With the increase of the sintering temperature at 845 ^{0}C, a decrease in the diffraction peaks of the phase 2212 is observed, and with the increase of the pressure at 392MPa this phase falls below 10%. By increasing the uniaxial pressure the electrical resistance decreases due to the improvement of the contacts between the granules and their orientation perpendicular to the direction of application of the pressure. Following the SEM analysis, it is observed that the superconductors have a uniform surface, but the size of the granules changes so that the sample sintered at 845 °C and the uniaxial pressure of 392 MPa has the best crystallinity.

REFERENCES

[1] C. Terzioglu, M. Yilmazlar, O. Ozturk, E. Yanmaz, Physica C 423 (2005) 119.
[2] M. Yilmazlar, H.A. Cetinkara, M. Nursoy, O. Ozturk, C. Terzioglu, Physica C 442 (2006) 101.
[3] M. Yilmazlar, O. Ozturk, O. Gorur, I. Belenli, C. Terzioglu, Supercond. Sci. Technol. 20 (2007) 365.
[4] O. Gorur, T. Kucukomeroglu, C. Terzioglu, A. Varilci, M. Altunbas, Physica C 418 (2005) 355.
[5] S.M. Khalil, J. Phys. Chem. Solids 64 (2003) 855.
[6] C. Terzioglu, O. Ozturk, A. Kilic, A. Gencer, I. Belenli, Physica C 434 (2006) 153.
[7] D. Yegen, C. Terzioglu, O. Gorur, I. Belenli, A. Varilci, Chin. J. Phys. 44 (3) (2006) 233.
[8] O. Ozturk, D. Yegen, M. Yilmazlar, A. Varilci, C. Terzioglu, Physica C 451 (2007) 113.
[9] A. Biju, R.P. Aloysius, U. Syamaprasad, Supercond. Sci. Technol. 18 (2005) 1454.
[10] N. Udomkan, P. Vinotai, R. Suryanarayanan, N. Charoenthai, Supercond. Sci. Technol. 18 (2005) 1294.
[11] V.G. Prabitha, A. Biju, R.G. AbhilashKumar, P.M. Sarun, R.P. Aloysius, U. Syamaprasad, Physica C 433 (2005) 28.
[12] A. Biju, R.G. Abhilash Kumar, R.P. Aloysius, U. Syamaprasad, Physica C 449 (2006) 109.
[13] A. Ekicibil, A. Coskun, B. Ozcelik, K. Kiymac, J. Low Temp. Phys. 140 (2005) 105.
[14] K. Ozturk, S. Celik, U. Cevik, E. Yanmaz, J. Alloys Compds. 433 (2007) 46.
[15] N Sanada, T Nakadaira, M Shimomura, Y Suzuki, Y Fukuda, M Nagoshi, Y Syono and M Tachiki, Physica C263, (1996) 286
[16] A.V. Pop, D. Marconi, V. Pop, M. Pop, J. Optoelectron. Adv. Mater. 8 (2) (2006) 476–479.
[17] A.A. El-Abar, P.J. King, K.J. Maxwell, J.R. Owers-Bradley, W.B. Roys, Physica C 198 (1992) 81.
[18] A.V. Pop, G. Ilonca, M. Pop, D. Marconi, Int. J. Mod. Phys. B 18 (15) (2004) 2169.
[19] D Marconi, M Pop, AV Pop, Journal of Alloys and Compounds 513, (2012) 586-591

STUDIA UBB PHYSICA, Vol. 63 (LXIII), 1-2, 2018, pp. 143-151
(RECOMMENDED CITATION)
doi:10.24193/subbphys.2018.15

ENGINEERED PAPER PLATFORM LOADED WITH GOLD NANOSPHERES TO IMPROVE SERS PERFORMANCE FOR ANALYTE DETECTION

F. ORZAN[1], A. CAMPU[2], S. SUARASAN[2], S. ASTILEAN[1,2] AND M. FOCSAN[2,*]

ABSTRACT. In this paper, we report a flexible surface enhanced Raman scattering (SERS) nanoplatform based on a Whatman paper loaded with gold nanospheres *via* a direct immersion approach. After the fabrication and optical/morphological characterization, the SERS performance of our plasmonic nanoplatforms was tested using the non-resonant Raman p-aminothiophenol (p-ATP) analyte. Finally, the plasmonic nanoplatform developed here has demonstrated to have excellent reproducibility, the SERS efficiency being highly dependent on the AuNPs concentration loaded on the 3D flexible scaffold paper.

Keywords: *paper substrate; gold nanospheres; SERS detection, sensor nanoplatform*

INTRODUCTION

In the recent years, a growing interest is focused on the possibility to fabricate efficient, stable, reproductible and inexpensive bio(nano)sensors

[1] *Babeş-Bolyai University, Faculty of Physics, Biomolecular Physics Department, 1 M. Kogălniceanu str., 400084 Cluj-Napoca, Romania*
[2] *Babes-Bolyai University, Interdisciplinary Research Institute in Bio-Nano-Sciences, Nanobiophotonics and Laser Microscopy Center, 42 T. Laurian str., 400271, Cluj-Napoca, Romania*
** Corresponding author: monica.iosin@phys.ubbcluj.ro*

that can be effectively implemented in the clinical analyses in order to identify various diseases in their early stages, hence preventing their progression [1].

Paper has recently been claimed as an ideal flexible substrate for inexpensive analytical tests both in health and environment applications [2]. Although enzyme-linked immunosorbent assay (ELISA) -as a common solution-based tool- can be theoretically applied to paper, it requires multiple reactants as well as washing steps, making this technique complicated and hard to implement [3]. Therefore, a direct technique able to detect analytes of interest even at very low concentrations, through the direct interaction between the treated paper substrate and analytes, is highly desired. Surface-enhanced Raman scattering (SERS) can be such a technique, by combining the molecular specificity of the Raman spectroscopy with the high sensitivity of the gold nanoparticles based on their exceptional plasmonic properties (i.e. field enhancement) [4]. In this context, the SERS technique is continuously applied in food, water or clinical analysis, major research topics, which are associated with a healthy life style aiming to prevent diseases. Even so, for the direct implementation of the plasmonic platform in routine SERS applications, it is a critical requirement to engineer robust, reproductible, stable and sensitive substrate. Paper, with its excellent features such as easy-to-use, flexibility, robustness, three-dimensional (3D) porosity and so on, represents -therefore- a promising SERS nanoplatform for different relevant bioassays [5,6] .

In this paper, positively charged cetyltrimethylammonium chloride (CTAC) spherical nanoparticles (denoted further as CTAC@AuNPs) in solution were loaded via a simple immersion approach onto the Whatman no 1 paper, selected herein as common filter paper consisting of 98 % α-cellulose. We proved that after the CTAC@AuNPs loading on paper, their characteristic optical response in aqueous solution was well-transferred and maintained on the paper substrate. The CTAC@AuNPs size and morphology of the as-fabricated plasmonic paper substrate were rigorously characterized by transmission electron microscopy (TEM) and scanning electron microscopy (SEM), respectively. Then, a model Raman analyte, p-aminothiophenol (p-ATP), was adsorbed on the CTAC@AuNPs paper substrate and its generated SERS signal was evaluated.

Further on, the effect of the CTAC@AuNPs concentration loaded on the paper - induced and controlled by three successive dipping steps- was finally discussed in terms of SERS performance of our engineered paper nanoplatforms, in the context of the increased necessity to improve the paper-based SERS nanoplaforms efficiency for further specific biodetection.

EXPERIMENTAL DETAILS

Chemicals

Hydrogen tetrachloroaurate-(III) trihydrate ($HAuCl_4 \cdot 3H_2O$, 99.99 %), sodium borohydride ($NaBH_4$), Hexadecyltrimethylammonium bromide (CTAB, 96%), Cetyltrimethylammonium chloride solution (CTAC), ascorbic acid (AA), p-aminothiophenol (p-ATP) and Whatman® qualitative filter paper, Grade 1 (Whatman no. 1) were purchased from Sigma-Aldrich (Germany). All chemicals were of analytical grade, and all aqueous solutions were prepared using ultrapure water (resistivity ~ 18 MΩ).

Synthesis of CTAC-stabilized gold nanospheres

The CTAC-stabilized gold nanospheres (CTAC@AuNPs) were synthesized using an adapted version of the previously reported approach by Zheng *et al*. [7]. In summary, the CTAB-capped Au clusters were firstly prepared by adding a $NaBH_4$ solution to a 10 ml mixture of 0.25 mM $HAuCl_4$ and 100 mM CTAB. 10 µl of Au clusters were then mixed with a freshly prepared solution of 2 ml CTAC (200 mM) and 1.5 ml of AA, followed by the addition of a 2 ml of 0.5 mM $HAuCl_4$ solution in order to finally obtain Au seeds of 10 nm diameter. After 15 min reaction at 27 °C, the seeds were centrifuged once at 14500 rpm for 30 min and redispersed in 1 ml 20 mM CTAC solution.

Fabrication of the plasmonic strips

For the preparation of plasmonic nanoplatforms, paper strips were firstly cut from the Whatman sheet and thenafter immersed into a Petri dish that contained CTAC@AuNRs colloidal solution for 10 minutes and left to dry 10 minutes at 45 ^{o}C before further analysis. In order to increase the CTAC@AuNPs concentration loaded on paper, the immersion procedure was repeated 3 times.

Preparation of SERS active paper nanoplatforms

10 µL ethanolic solution of 10^{-5} M of p-ATP molecules were prepared and dropped onto the dried CTAC@AuNPs paper to create a p-ATP monolayer on the plasmonic nanoplatform.

Experimental measurements

The extinction spectra of the CTAC@AuNPs in aqueous solution and loaded onto the paper substrate were recorded using a Jasco V-670 UV-Vis-NIR spectrophotometer with 1 nm spectral resolution. The morphology of the CTAC@AuNPs was examined using a FEI Tecnai F20 field emission, high resolution TEM (TEM/HRTEM) operating at an accelerating voltage of 200 kV and equipped with Eagle 4k CCD camera. Dynamic light scattering (DLS) and Zeta Potential measurements were performed using a Zetasizer Nano ZS 90 from Malvern Instruments. The morphology and the uniformity of the engineered CTAC@AuNPs nanoplatforms were investigated by scanning electron microscopy (SEM) using a FEI Quanta 3D FEG scanning electron microscope. All SERS spectra were recorded in air using a portable spectrometer (Raman Systems R3000CN) equipped with a 785 nm diode laser coupled to a 100 µm optical fiber.

RESULTS AND DISCUSSION

First, the optical response of the as-prepared CTAC@AuNPs in aqueous solution was investigated and depicted in Fig. 1. As such, the as-synthesized colloidal CTAC@AuNPs exhibit a plasmonic resonance band

centered at 529 nm (Fig. 1), which is consistent with an average diameter of 45±3.5 nm, as provided by transmission electron microscopy (TEM) observation (inset in Fig. 1). The CTAC@AuNPs size investigation by DLS measurement also revealed a highly monodispersed plasmonic AuNPs with an average hydrodynamic diameter of 55 nm (data not shown here). The advantages of employing this seed-mediated growth method is represented by: i) the resulting positively charged CTAC@AuNPs having a zeta potential of + 51 mV, allowing their direct electrostatic interaction with the negatively charged cellulose, caused of its hydroxyl groups [8]; ii) the narrow full width at half maximum (FWHM) compared to the citrate-covered AuNPs synthesized using the well-known standard Turkevich method [9], allowing thus this type of AuNPs to be further implemented as robust LSPR biosensors.

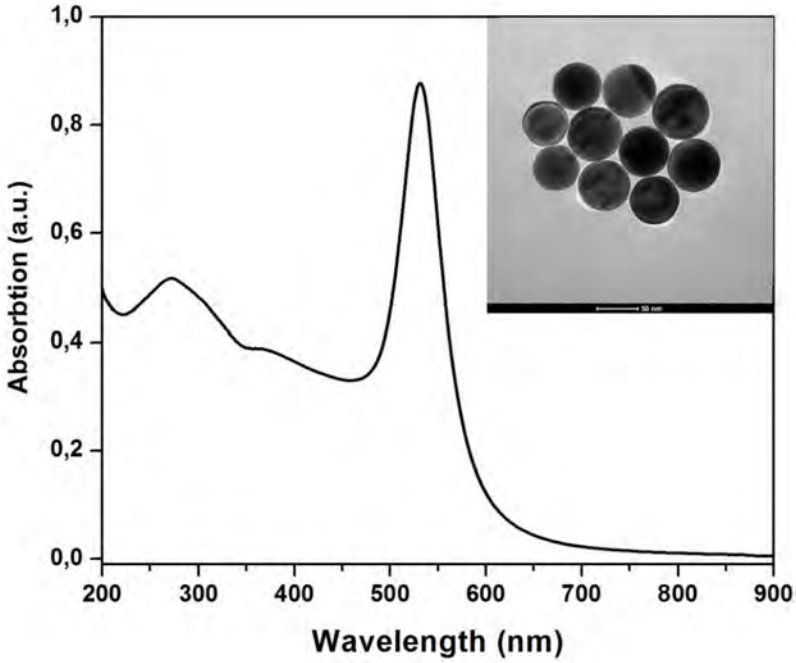

Fig. 1. The extinction spectrum of the CTAC@AuNPs obtained in aqueous solution. In inset is presented a representative TEM image of the synthesized CTAC@AuNPs.

After the immersion of the filter paper into the colloidal solution for 10 minutes, the color of the paper becomes red, in concordance with the color of the colloidal solution, denoting the first prove that the CTAC@AuNPs were successfully loaded onto the paper (Fig. 2(c)). To note that the color intensity of the dried CTAC@AuNPs paper nanoplatform became more intense as the number of the immersion steps was increased. SEM investigation was subsequently employed to confirm the presence of CTAC@AuNPs on the paper substrate in a dense and uniform distribution. As such, Fig. 2(b) depicts a typically SEM image, showing one bare paper microfiber, without CTAC@AuNPs. Contrarily, Fig. 2(b) shows a paper fiber with the loaded CTAC@AuNPs, the nanoparticles being well-adsorbed on paper after their diffusion from the colloidal solution into the 3D porous structure of the Whatman paper.

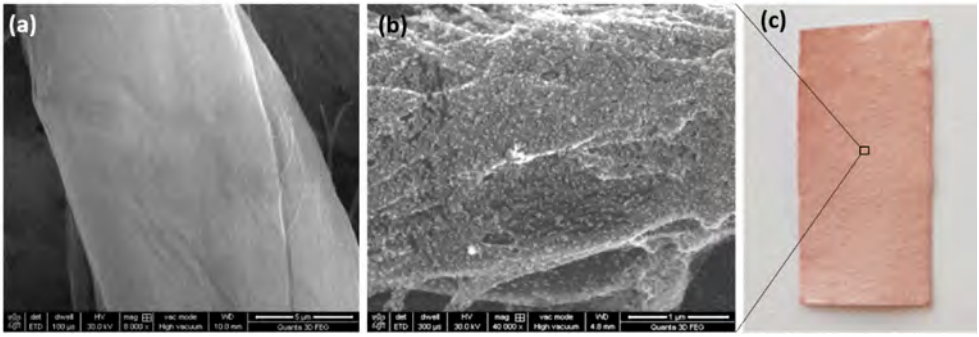

Fig. 2. (a) Representative SEM images before (bare Whatman paper) and (b) after loading with CTAC@AuNPs. (c) Digital photo of the fabricated plasmonic paper.

Further on, the UV-Vis analysis was performed on the fabricated plasmonic-paper nanoplatform. Specifically, the plasmonic response of the CTAC@AuNPs loaded on paper was well-preserved, and -more importantly- the amount of the CTAC@AuNPs adsorbed on the paper micro(nano)fibers increases with the number of immersion steps (Fig. 3(a)). This observation results from the ability of the 3D cellulose microfibers network of the Whatman paper to provide strong capillary forces for the diffusion of CTAC@AuNPs from

colloidal solution. The effect of the optical density of CTAC@AuNPs paper platforms was subsequently evaluated by SERS, by employing p-ATP molecule as active Raman probe, due to its strong affinity for Au surface via thiol linking, its ability to form a self-assembled monolayer as well as its distinct Raman vibrations [10]. After dropping 10 µL ethanolic solution of 10^{-5} M p-ATP onto the dried CTAC@AuNPs papers with different optical densities -obtained after three successive dipping steps- we observe that all paper platforms are Raman active. Moreover, all recorded spectra exhibit similar Raman peak positions, except their intensities which vary as function of the concentration of CTAB@AuNPs loaded onto the paper (Fig. 3(b)). To note that all spectra are dominated by three major Raman bands: i) at 387 cm $^{-1}$ assigned to δ(C-S), ii) at 1075 cm $^{-1}$ assigned to ν(C-S) and iii) 1585 cm $^{-1}$ assigned to ν(C-C).

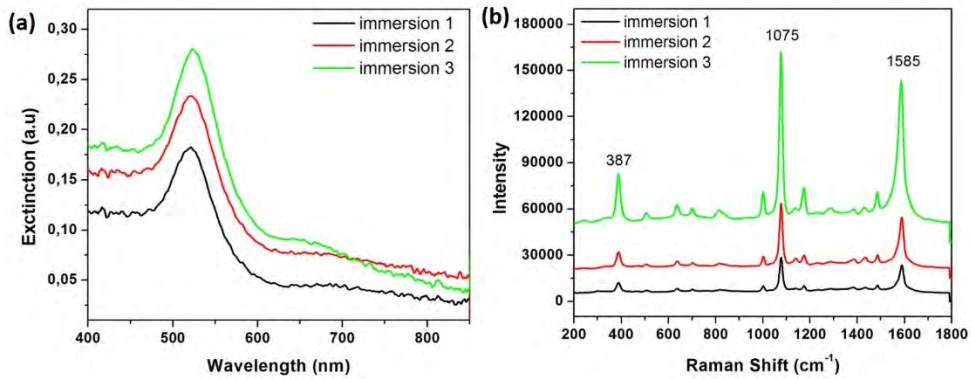

Fig. 3. (a) The optical response of the fabricated CTAC@AuNPs paper nanoplatforms with different nanoparticles concentration, (b) together with their SERS efficiency evaluated using the p-ATP analyte and excitation laser at 785 nm.

As a result, we found that the SERS intensity increases with the concentration of the CTAC@AuNPs loaded onto the paper platforms. However, we assume that the higher SERS efficiency obtained after three immersion steps (green spectrum in Fig. 3 (b)) are also due to plasmon coupling, which generates an enhanced electromagnetic field in the interparticle gaps, operating as effective SERS hot spots for p-ATP detection.

CONCLUSIONS

In conclusion, a simple and efficient plasmonic paper-based nanoplatform with enhanced SERS efficiency was designed. The positively charged CTAC@AuNPs bind electrostatically to the negatively charged cellulose fibers as a result of an easy immersion approach. Notably, the optical properties of the CTAC@AuNPs are well-preserved after the loading, moreover the concentration of the loaded nanoparticles can be increased by several consecutive immersions without harming their optical response. The CTAC@AuNPs paper-based nanoplatforms exhibit SERS performances when the p-ATP Raman reporter is employed. All samples present the vibrational spectrum of the p-ATP molecule, with increasing the optical density the SERS spectra are strongly amplified. Our plasmonic paper-based SERS nanoplatform relies on simple and cheap but highly sensitive and efficient fabrication and detection strategies becoming, therefore, interesting and reliable for analyte detection in complex samples.

ACKNOWLEDGMENTS

This work was supported by CNCS-UEFISCDI Romania, under the projects number PN-III-P1-1.1-TE-2016-2095.

REFERENCES

[1] C. Parolo, A. Merkoçi, *Chem. Soc. Rev.* 42, 450 (2012).
[2] K.A. Kirk, A. Othman, S. Andreescu, *Anal. Sci.* 34, 19 (2018).
[3] A. Ambrosi, F. Airò, A. Merkoçi, *Anal. Chem*. 82, 1151 (2010).
[4] M. Focsan, A. Campu, A.-M. Craciun, M. Potara, C. Leordean, D. Maniu, S. Astilean, *Biosens. Bioelectron*. 86, 728 (2016).
[5] L. Susu, A. Campu, A.M. Craciun, A. Vulpoi, S. Astilean, M. Focsan, *Sensors* 18, 3035 (2018).
[6] A. Campu, L. Susu, F. Orzan, D. Maniu, A.M. Craciun, A. Vulpoi, L. Roiban, M. Focsan, S. Astilean, *Front. Chem.* 7 (2019).

[7] Y. Zheng, X. Zhong, Z. Li, Y. Xia, *Part. Part. Syst. Charact.* 31, 266 (2014).
[8] R.J.B. Pinto, P.A.A.P. Marques, A.M. Barros-Timmons, T. Trindade, C.P. Neto, *Compos. Sci. Technol.* 68, 1088 (2008).
[9] J. Turkevich, P.C. Stevenson, J. Hillier, *Discuss. Faraday Soc.* 11, 55 (1951).
[10] A.C. Peacock, A. Amezcua-Correa, J. Yang, P.J.A. Sazio, S.M. Howdle, *Appl. Phys. Lett.* 92 141113 (2008).